Laser Spectroscopy of Caesium Dimers

A thesis submitted in partial fulfilment of the requirements
for the degree of Doctor of Philosophy by

Louise Sara Butcher

St John's College, Oxford
Michaelmas Term 1997

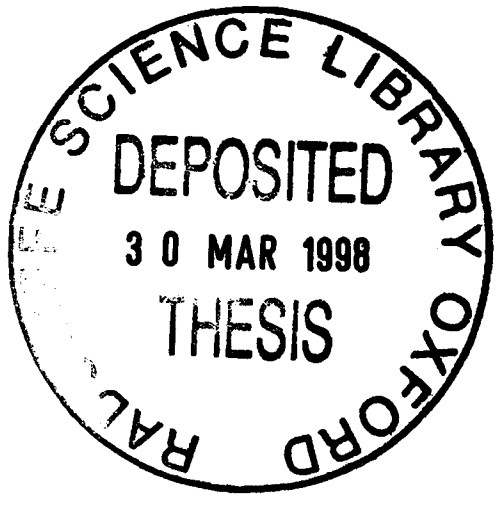

Abstract

We have obtained spectra of 10 vibrational bands of the Cs_2 $(2)^3\Pi_u \leftarrow x^3\Sigma_g^+$ system. The molecules were formed in a supersonic free jet expansion, and were excited by light from a single mode CW dye laser. The total laser induced fluorescence was measured at 90° to the incident light and molecular beam, using a photomultiplier. Using a slit system to image a selected part of the interaction region, we have reduced the Doppler width to about 350MHz.

We have been able to resolve the discrepancy between the different vibrational band positions given in two previous papers. Our vibrational bands show broad rotational contours, but we have not been able to resolve individual rotational lines.

We have also obtained rotationally resolved spectra of the bandhead region of 22 vibrational bands of the $B^1\Pi_g \leftarrow X^1\Sigma_u^+$ system. We found that the frequencies of the bandheads agreed with the bandhead positions deduced from the Dunham coefficients of a previous work. We have developed a theoretical model of the rotational structure and intensity distribution, taking into account optical pumping and the small solid angle subtended by the detector. By fitting this model to the experimental spectrum of the $v' = 3, v'' = 0$ band using least squares optimization, we were able to extract rotational constants and line positions. We found that these line positions were in good agreement with those from the previous work.

We have discussed how such spectroscopic data may be used in a determination of the s-wave scattering length of caesium, and we have reviewed the validity of the scattering length and other parameterisations of low energy Cs-Cs interactions.

Acknowledgements

First and foremost my thanks go to Keith Burnett, Derek Stacey and Carol Thompson for their constant support and encouragement over my time as a research student. Without their ideas, advice and reassurance, this thesis would not have been possible. I am also grateful to Stuart Lawrence for his help in the early stages of the experiment, and to Hans Müschenborn, both for help in the lab and for providing an excellent set of computer programs. A big thank you goes to Graham Quelch for his advice and technical support, and for the dried toad collection. Thanks also go to John Watson and Pete Ruprecht for keeping the computers running.

I would also like to thank all the others, both from the lab and from college, who have made my time in Oxford so enjoyable; in particular I must thank "Herodotos' friends" for the Union quiz nights.

Finally, a big thank you to Matt and my family for their love and support.

I gratefully acknowledge the financial support of the EPSRC.

Contents

List of Figures

List of Tables

Chapter 1

Introduction

This thesis describes high-resolution spectroscopy of the molecule formed of two caesium atoms, a *caesium dimer*. The interatomic potential of the caesium dimer gives a series of vibrational and rotational energy levels, as described in chapter 2. By looking for transitions between these levels using molecular spectroscopy, we can find the energies of these levels, and hence the form of the potentials, using the techniques given in chapter 3. But first we must ask why we wish to know the interatomic potentials of the caesium dimer.

1.1 Motivation for the current work - prospects for Bose-Einstein condensation in caesium.

In July 1995, Anderson et al. [1] observed Bose-Einstein condensation, or BEC, in a gas of rubidium-87 atoms cooled to just 170nK. In Bose-Einstein condensation, a phase transition occurs when the mean particle separation is comparable with the de Broglie wavelength of the particles. This leads to a sudden increase in the population of the ground state of the system. Although BEC has previously been studied in relation to superconductivity and superfluidity, this was the first observation of the phenomenon in a dilute atomic gas. Other observations of BEC in lithium-7 and sodium quickly followed [2, 3].

Bose-Einstein condensation has not yet (as of September 1997) been observed in caesium, the heaviest of the alkalis. Caesium is of particular interest as it is the element used in atomic clocks; the second is defined in terms of the frequency of a hyperfine transition in caesium. Many experiments on laser cooling and trapping of

caesium have taken place in Oxford, Paris and elsewhere [4]. What are the prospects for Bose-Einstein condensation of caesium?

In order to answer this question, we need to understand the collision processes which take place at the very low temperatures required for BEC. At these temperatures, quantum mechanical effects become significant, and it is not easy to predict what will happen when two atoms come together.

The behaviour of atoms in collisions at low temperatures can be represented in many cases by a single parameter, the *scattering length*, α. At low temperatures and when the atoms are well separated, they can be treated as though they are hard spheres with a radius $|\alpha|$. The elastic cross section is then given by $\sigma = 4\pi\alpha^2$. However, unlike the radius of a hard sphere, the scattering length can have either positive or negative sign. A positive scattering length corresponds to effectively repulsive interactions, and a negative scattering length to effectively attractive interactions. The sign of the scattering length determines the stability of a condensate. It was initially thought that a positive scattering length was essential to observe BEC [5]. However, BEC has been observed in lithium-7 [2], which is known to have a negative scattering length [6]. But although it has been shown that a condensate is possible for a negative scattering length, the attractive collisions lead to contraction of the cloud and hence heating and loss of atoms from the condensate; hence such a condensate is unstable for all but very small numbers of atoms [7]. So it is still highly desirable to have a positive scattering length.

Cold collisions also determine the rate of evaporate cooling, the technique used to reach the very low temperatures required for Bose-Einstein condensation to take place. In this technique, the depth of the magnetic trap holding the atom is decreased, so that faster atoms escape from the trap, leaving behind the cooler atoms [8]. For evaporative cooling to be effective, many elastic two-body collisions are required to maintain thermal equilibrium in the gas; however it is required that there are few spin flip two-body collisions that change the state, inelastic collisions which put atoms into untrapped states, or three-body collisions, which allow atoms to stick together and fall out of the trap. The rate of these three body collisions has been calculated to vary with α^4 [9].

The study of cold collisions is also important in other areas. In atomic fountains for use as frequency standards [10], collisions between atoms perturb the atomic energy levels, and lead to frequency shifts of a few mHz. Cold collisions have an effect in

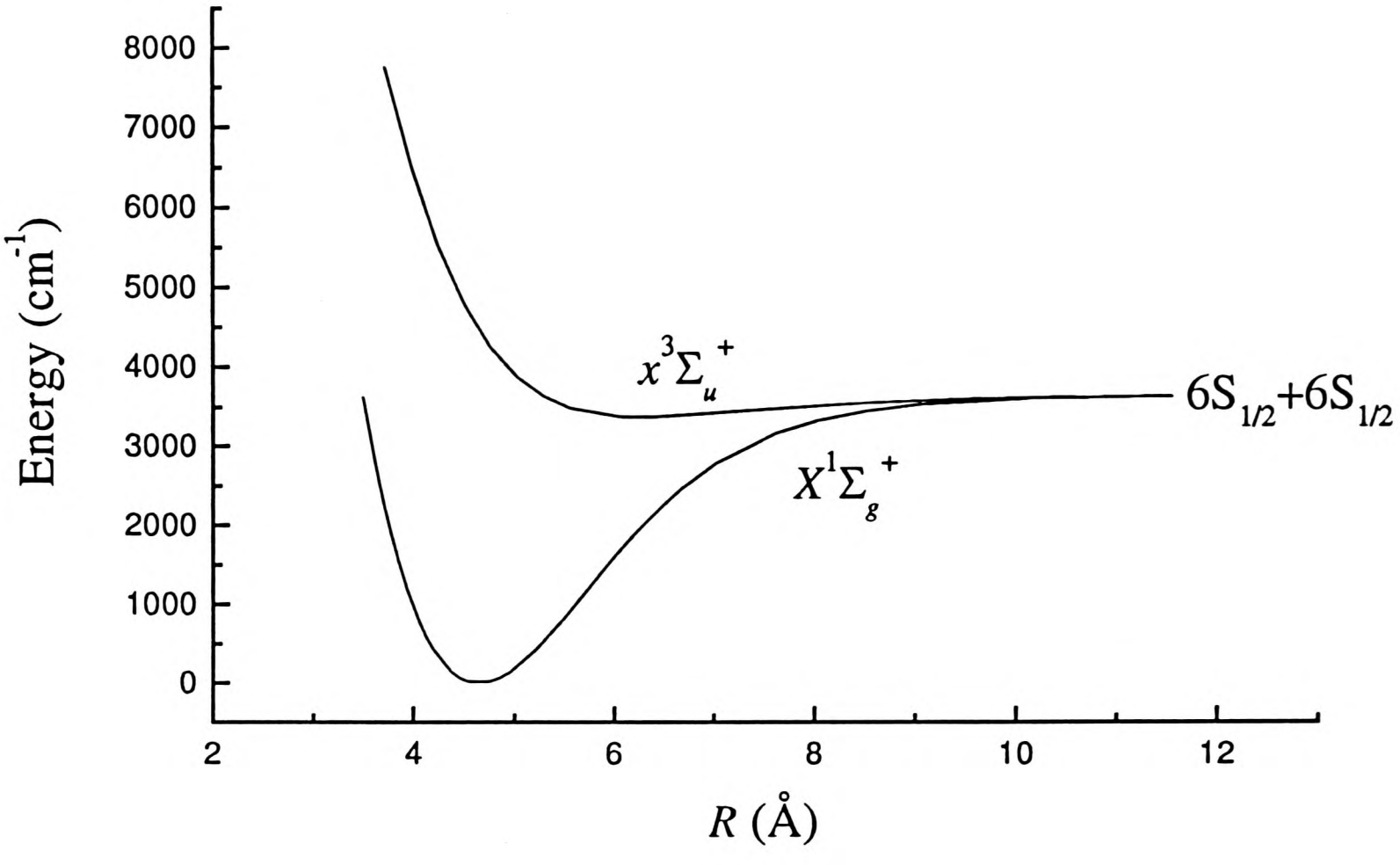

Figure 1.1: The ground state interatomic potentials of Cs_2.

atom interferometery, where interactions give an effective "refractive index" for the matter waves [11].

How can scattering lengths be deduced? One method is by looking at processes which depend on the scattering length: the relaxation time of atoms in a magnetic trap [12] or frequency shifts in an atomic fountain [13]. The intensities of transitions studied by photoassociation spectroscopy [14] can be used to deduce the phase shift in the wavefunction, and hence the scattering length (see also section 6.3.3). However, the method we shall be working towards in this thesis is to derive the scattering length from the *interatomic potential.* An interatomic potential is the energy of interaction between two atoms as a function of their separation. The ground state interatomic potentials of Cs_2 are shown in figure 1.1. At large separations the energy is just the energy of the free atoms (the *dissociation limit*). As the atoms come closer together, there are attractive forces between them. At very small separations, the forces between the atoms are repulsive, and the corresponding energy becomes large and positive. In the intermediate region, there is an attractive potential well, which may give rise to discrete bound states. In figure 1.1, we see that there are in fact two

different interatomic potentials which correspond to free atoms in the ground state. This arises because when the two ground state atoms come together they can do so in one of two ways. Each atom has a single outermost electron, leading to a spin of $\frac{1}{2}$. When the atoms come together, the spins can either align to be antiparallel, leading to a total spin of zero, or parallel, leading to a total spin of 1. Just as in atoms, the different spin states are labelled by the value $2S+1$, where S is the total spin. Hence the $S=0$ and $S=1$ states are known as the singlet and triplet states respectively.

As the singlet and triplet ground states have different interatomic potentials, they also give rise to different scattering lengths. These are known as the singlet and triplet scattering lengths, a_S and a_T. The scattering length which applies is determined by the states of the two atoms involved in the collision. Two atoms colliding with their spins parallel are governed by the triplet scattering length, while two atoms with their spins antiparallel are governed by the singlet scattering length. In fact, the situation is a little more complex due to the effects of hyperfine structure in the atoms, and the pure singlet case is never observed.

The hyperfine structure of the caesium atom as a function of applied magnetic field is shown in figure 1.2.

We are interested particularly in the states of the atoms which are amenable to trapping. Trapping requires a low-field seeking long-lived hyperfine state [15]. There are two such states for caesium as shown in figure 1.2: the $(F, m_F) = (4, +4)$ and $(F, m_F) = (3, -3)$ states. The scattering length of the $(4, +4)$ state is given purely by a_T, while the scattering length which applies to the $(3, -3)$ state is a mixture of a_T and a_S. As the combination of the two scattering lengths is dependent on the applied magnetic field strength, the scattering length for the $(3, -3)$ state may be tunable with magnetic field [15]. It may also be possible to tune the scattering length using nearly-resonant light [16]. This brief discussion shows that whichever hyperfine state is used, a knowledge of the triplet scattering length is necessary. However, the triplet scattering length in caesium is not well known, compared to the scattering lengths of the other alkalis. Table 1.1 shows the current values of scattering lengths for the alkali metals.

How can we deduce scattering lengths from interatomic potentials? If the potential does not support bound states, then finding the sign of the scattering length is straightforward; a purely repulsive potential leads to repulsive collisions, and a positive scattering length, while an attractive potential which supports no bound states

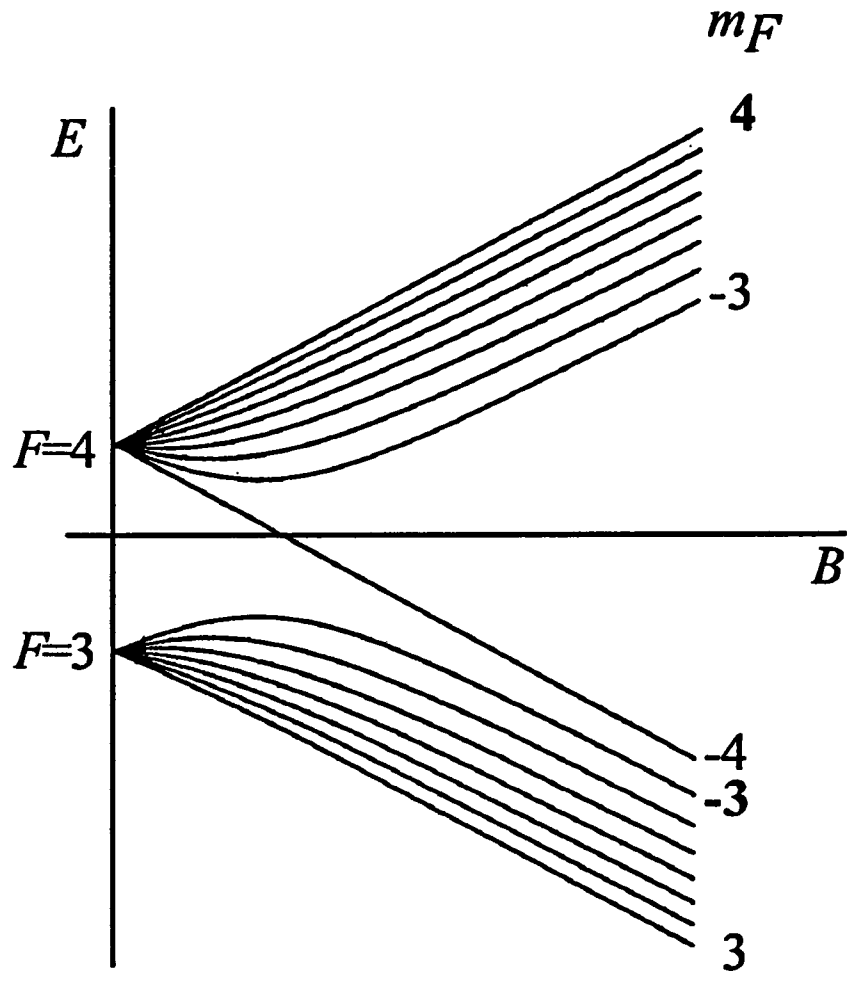

Figure 1.2: Caesium hyperfine states as a function of magnetic field.

	a_S (a_0)	a_T (a_0)	Techniques used	Ref.
^{6}Li	45.5±2.5	-2160 ± 250	Photoassociation spectroscopy	[17]
^{7}Li	33±2	-27.6±0.5	Photoassociation spectroscopy	[17]
^{23}Na	34.9	77.3	Molecular spectroscopy plus theoretical long and short range potential	[18]
^{87}Rb		+99→+119	Photoassociation spectroscopy	[19]
^{85}Rb		-1200→-80	Photoassociation spectroscopy	[20]
^{133}Cs		-200→-1100 -250	Frequency shifts in atomic fountain Theoretical potential	[13] [21]

Table 1.1: Scattering lengths of the alkalis

leads to attractive collisions, and a negative scattering length. Where the potential supports bound states, however, the situation is more complex. The magnitude and sign of the scattering length depends critically on the exact shape of the potential, and in particular on the position of the least bound state, as discussed in depth in chapter 3. Hence a very accurate knowledge of the interatomic potentials is required to calculate the scattering length.

How can we find the interatomic potentials sufficiently accurately? One method which has been tried is to use ab initio potentials [22, 23]. These are not generally sufficient to be used alone, but are useful to supplement experimental data. The long range parts of the potentials can be calculated using perturbation theory [24]. These long range parameters complement experimental work, as experiments can often find only the short-range part of the potential. In a recent estimate of the triplet scattering length, Pillet et al. [21] used a theoretical potential and long range parameters, finding a scattering length of -250a_0, which is within the range found by Verhaar et al.[13] using clock shifts. However, comparison of the parameters of the theoretical potential with experimental data is needed to judge its accuracy (see section 5.4.3).

The alternative method, and the one used in our work, is to find the the potentials experimentally using molecular spectroscopy. The two ground state interatomic potentials of caesium, from which α_S and α_T can be calculated are shown in figures 1.3 and 1.4, together with the other caesium interatomic potentials which have been studied previously. The important parameters of the potentials are tabulated in table 1.2: the dissociation energy D_e, the equilibrium separation of the atoms R_e and the vibrational constant ω_e. As can be seen from table 1.2, both theoretical and experimental methods have been used to find alkali potentials. Also shown are the singlet and triplet molecular transitions which we have studied.

The fact that despite its importance the triplet scattering length for caesium is known to such poor accuracy is some indication of the difficulties involved in its determination. The type of experiment described in this thesis, which is concerned only with the region near the minimum of the potential, cannot of itself give a value. However, it represents an important first step in providing much needed reliable data on the potential and resolving discrepancies in previously published work.

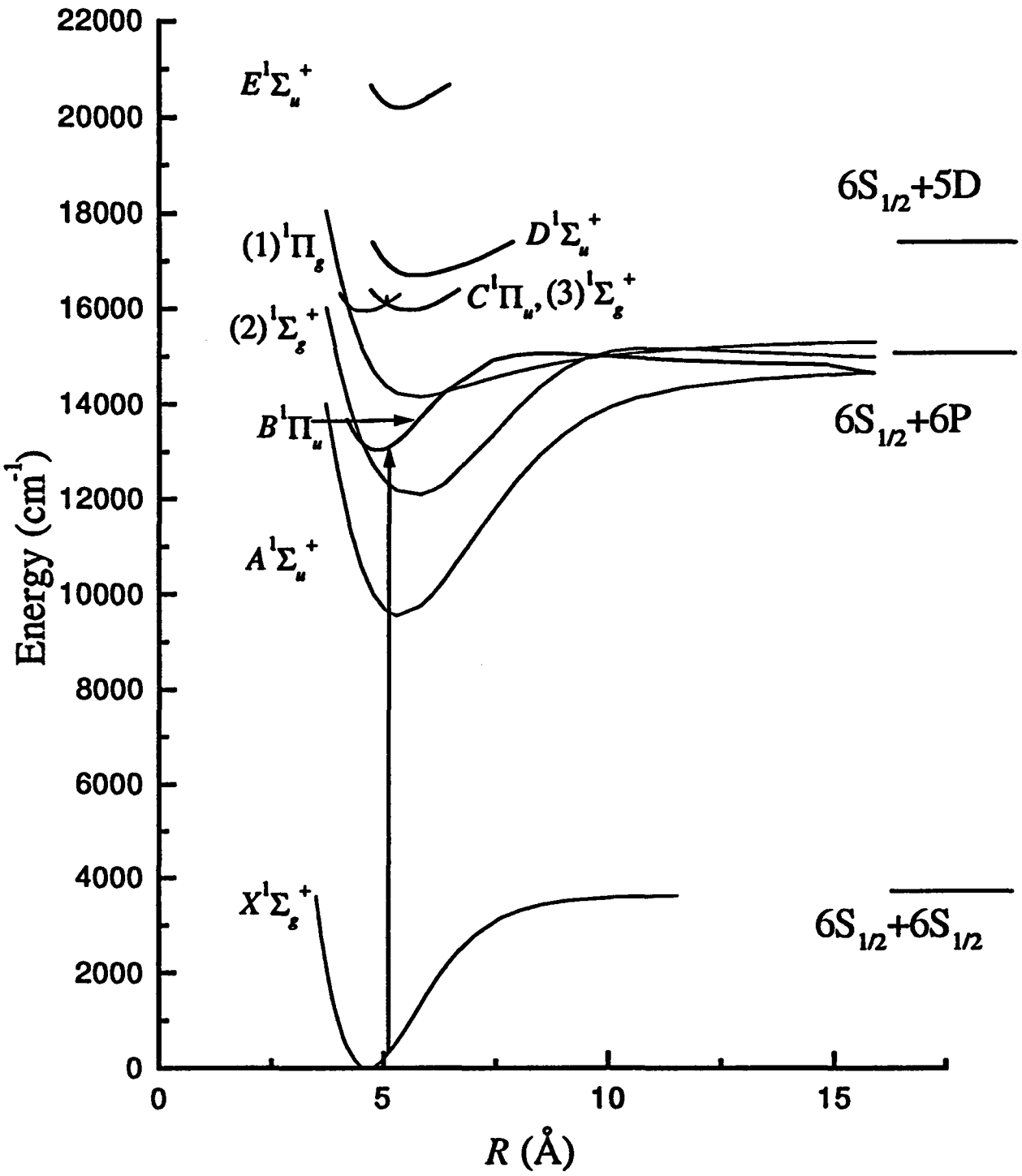

Figure 1.3: Singlet potentials of Cs_2

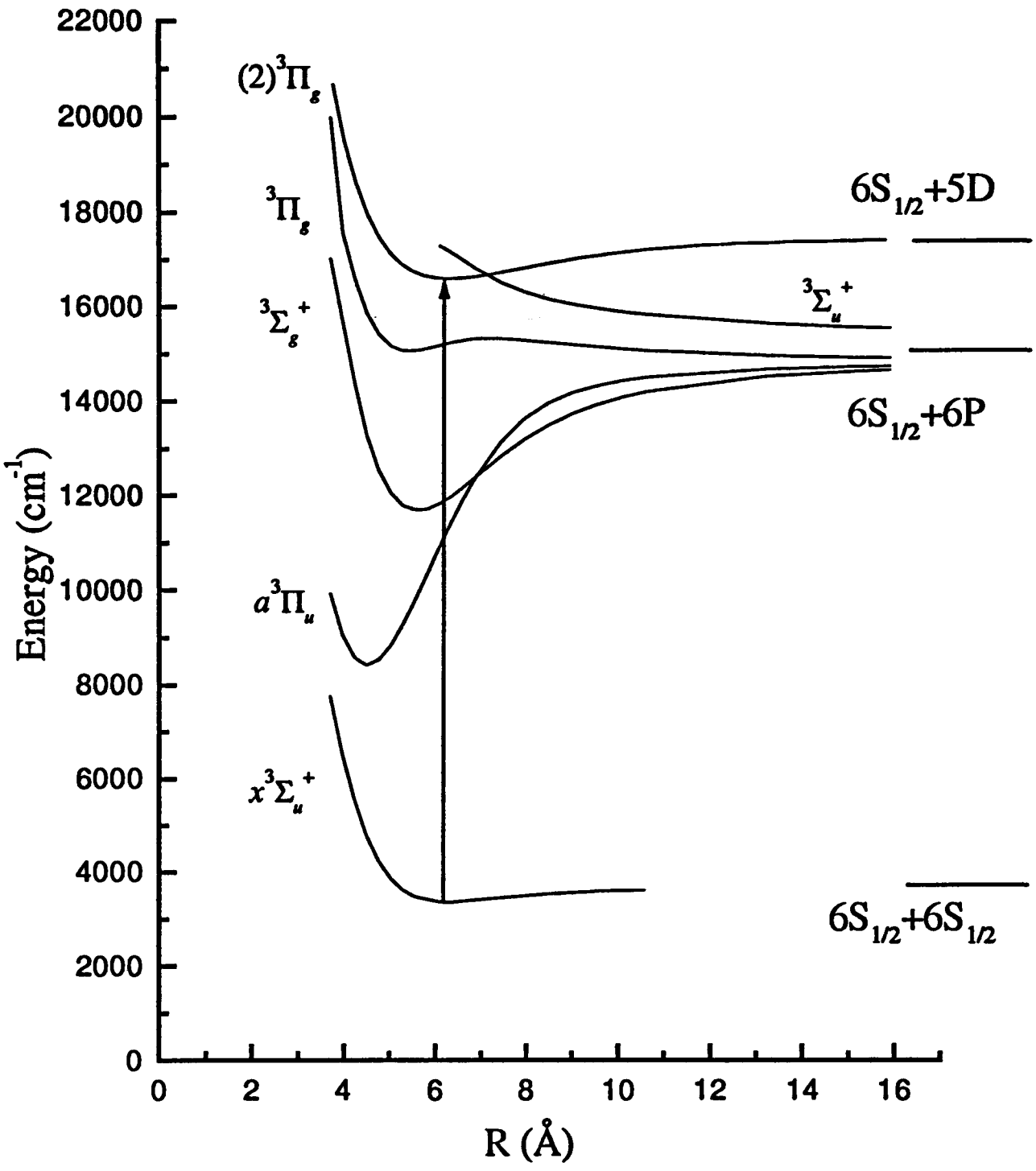

Figure 1.4: Triplet potentials of Cs_2

State	Dissociates to:	D_e (cm^{-1})	R_e ($\AA$)	ω_e (cm^{-1})	Ref.
$X^1\Sigma_g^+$	$6^2S_{\frac{1}{2}} + 6^2S_{\frac{1}{2}}$	3649.5	4.63	42.02	[25] (E)
		3573.0	4.63	40.99	[22] (T)
		3697	4.58	44.28	[23] (T)
$x^3\Sigma_u^+$	$6^2S_{\frac{1}{2}} + 6^2S_{\frac{1}{2}}$			11.05[1]	[26] (E)
		240	6.50[2]	11.2	[27](T)
				12.03	[28] (E)
		290	6.4	11	[25] (E+T)
		282.3	6.27	12.29	[22] (T)
		250	6.33	11.18	[23] (T)
$A^1\Sigma_u^+$	$6^2S_{\frac{1}{2}} + 6^2P$	5283.0	5.35	33.1	[22] (T)
		5561	5.24	33.74	[23]
$B^1\Pi_u$	$6^2S_{\frac{1}{2}} + 6^2P_{\frac{3}{2}}$	2338.1	4.85	34.3	[29] (E)
		1637.3	4.88	34.5	[22] (T)
		2193	4.78	36.69	[23] (T)
$(2)^1\Sigma_g^+$	$6^2S_{\frac{1}{2}} + 6^2P_{\frac{1}{2}}$	2713.7	5.83	23.35	[30] (E)
		2734.2	5.68	24.8	[22] (T)
		3060	5.68	23.01	[23] (T)
$(1)^1\Pi_g$	$6^2S_{\frac{1}{2}} + 6^2P_{\frac{3}{2}}$	1468.4	5.70	18.44	[30] (E)
		1226.0	5.70	18.8	[22] (T)
		1241	5.60	18.47	[23] (T)
$^3\Sigma_u^+$	$6^2S_{\frac{1}{2}} + 6^2P_{\frac{3}{2}}$?	Repulsive			[31, 22] (E,T)
$a^3\Pi_u$	$6^2S_{\frac{1}{2}} + 6^2P$?	6404.0	4.51	42.9	[22] (T)
		7099	4.43	47.66	[23] (T)
$^3\Sigma_g^+$	$6^2S_{\frac{1}{2}} + 6^2P$		5.54	28.64	[32] (E)
		3129.3	5.63	28.0	[22] (T)
		3247	5.46	27.98	[23] (T)
$^3\Pi_g$	$6^2S_{\frac{1}{2}} + 6^2P$	242.0	5.43	21.8	[22] (T)

Table 1.2: Parameters of the interatomic potentials of Cs_2

[1] Energy difference between $v'' = 0$ and $v'' = 1$

[2] Calculated from corresponding B_e value

State	Dissociates to:	D_e	R_e	ω_e	Ref.
$C^1\Pi_u$	$6^2S_{\frac{1}{2}} + 5^2D_{\frac{3}{2}}$	2297.7	4.5	29.66	[30] (E)
		2300	4.53	29.66	[31] (E)
		1964	4.40	30.89	[23] (T)
$(3)^1\Sigma_g^+$	$6^2S_{\frac{1}{2}} + 5^2D_?$	2173 or 2271	5.55	22.42	[30] (E)
		2090	5.58	22.65	[23] (T)
$D^1\Sigma_u^+$	$6^2S_{\frac{1}{2}} + 5^2D_{\frac{5}{2}?}$	1546	5.68	19.28	[30] (E)
		1535	5.64	19.83	[23] (T)
$(2)^3\Pi_g$	$6^2S_{\frac{1}{2}} + 5^2D_?$			17.4-18.0[3]	[26] (E)
		700-820[3]		19.6-17.2[3]	[28] (E)
			6.45[2]	17.9-18.9[3]	[27] (T)
$(3)(E)^1\Sigma_u^+$	$6^2S_{\frac{1}{2}} + 7^2S_{\frac{1}{2}}$	1989.7	5.34	28.99	[30] (E)
		1983	5.22	29.98	[23] (T)

Table 1.2: Parameters of the interatomic potentials of Cs_2 (continued)

1.2 Summary of experimental techniques and analysis

Since the dissociation energy of the caesium triplet state molecules is so small, they need to be formed at low temperatures in order to be stable. We form the caesium molecules in a supersonic free-jet expansion, which produces a cold beam of molecules with internal temperatures $\sim$ 10K. We then probe the molecules using a tunable dye laser beam, perpendicular to the molecular beam. When the frequency of the laser corresponds to a transition frequency of the caesium molecule, the molecules are excited into a higher state. Spontaneous emission then leads to the re-emission of photons (fluorescence) in all directions. We detect the fluorescence perpendicular to both the molecular beam and the laser beam using a photomultiplier as a photon counter. We detect the total fluorescence, i.e., not spectrally resolved. We tune the dye laser with time, scanning over approximately 30GHz in 3 minutes. We record the number of photon counts in each 0.5s interval using a PC. Hence our time scale is effectively a frequency axis. In order to normalise, linearise and calibrate our spectra, we simultaneously record an iodine bromide absorption spectrum and an iodine absorption spectrum, the fringes from an etalon, and the laser intensity using

[3]Depending on fine structure component

photodiodes.

We have studied two sets of spectra: the $B^1\Pi_u \leftarrow X^1\Sigma_g^+$ or "singlet" or B-X spectra around 765nm; and the $(2)^3\Pi_g \leftarrow x^3\Sigma_u^+$ or "triplet" spectra around 710nm.

Although we are interested in the vibrational and rotational levels of the ground states, we also include an electronic transition. Changes in vibrational and rotational energy level alone give spectra in the infra-red and microwave regions. By adding in an electronic transition, we can study a spectrum in the visible region, which is accessible using dye lasers.

We have been able to fit a theoretical model to the singlet spectra in order to extract the important molecular parameters. This involved a considerable extension to the conventional theory of intensities in molecular spectra, as described in chapter 5. Modelling the triplet spectra has proved more difficult as hyperfine structure must be taken into account.

1.3 Historical background

Many potentials of Cs_2 have been studied previously, as listed in table 1.2. We will now discuss the historical background of those potentials studied in this work, i.e., the $X^1\Sigma_g^+$ ground state singlet and the $B^1\Pi_u$ excited singlet states (B-X transitions) and the $x^3\Sigma_u^+$ ground state triplet and $(2)^3\Pi_g$ excited triplet states.

1.3.1 Singlet spectra

The B-X (singlet) absorption spectrum of Cs_2 was first reported in 1923 by McLennan and Ainslie [33]. Vibrational band positions were reported by Loomis and Kusch [34] in 1934. Although they were not able to obtain the high resolution available with modern laser techniques, their results agree remarkably well (to within $0.3cm^{-1}$) with the more recent study of the B-X bands. However, the first vibrational analysis was only given in 1969 by Kusch and Hessel [35].

An accurate ground state potential was determined in 1985 by Weickenmeier et al. [25], using data taken using a variety of laser spectroscopy techniques.

The B-X system was remeasured in 1989 by Diemer et al. [29], and the potential curve of the $B^1\Pi_u$ state was found, using polarization spectroscopy and optical-optical double resonance (OODR) spectroscopy. In polarization spectroscopy, caesium molecules are formed in a heatpipe at 610K, which is placed between crossed

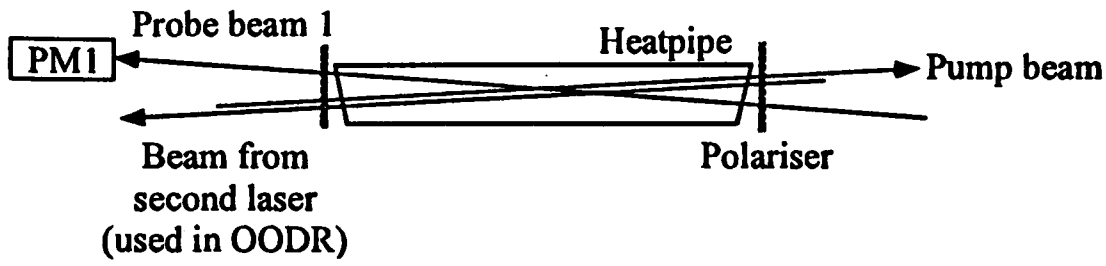

Figure 1.5: Experimental arrangement for polarization spectroscopy and OODR.

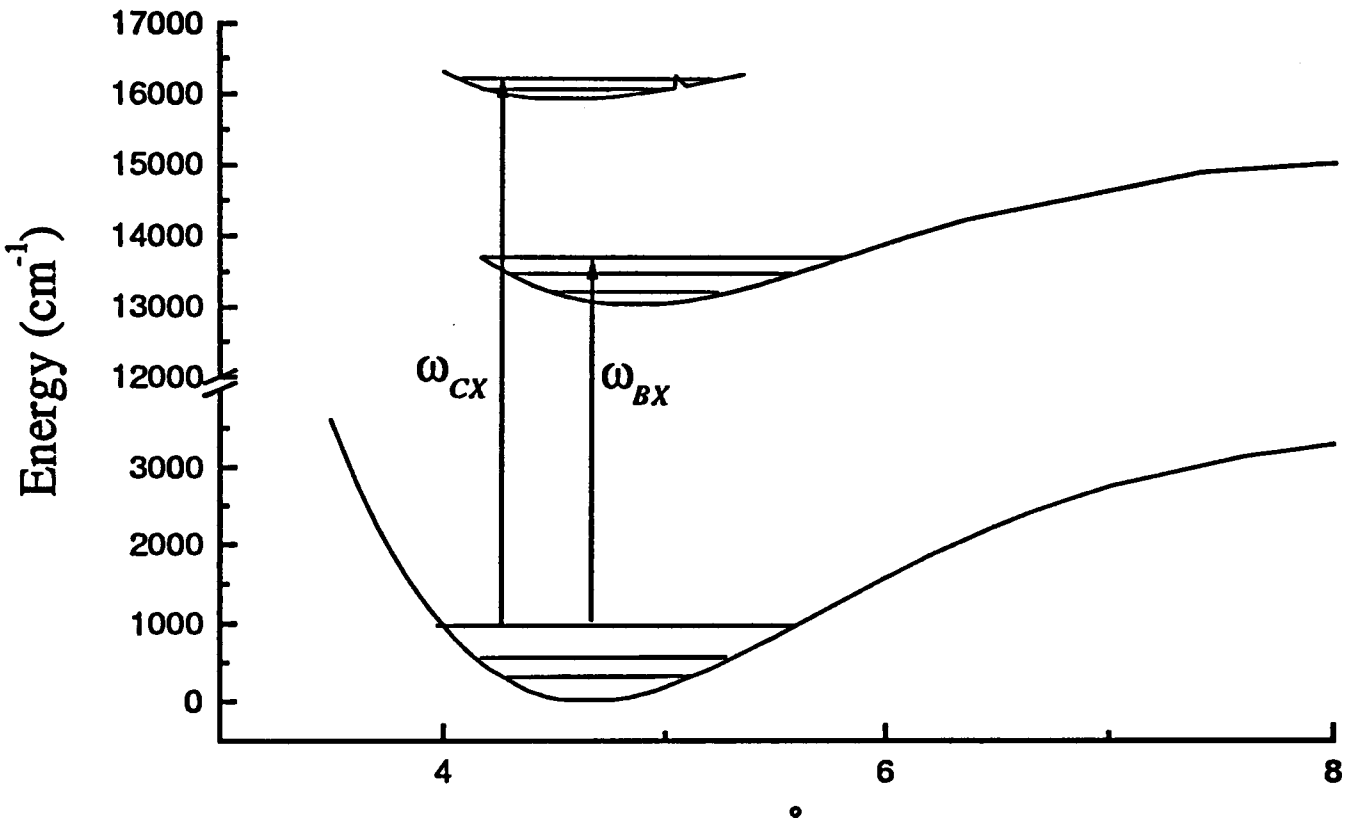

Figure 1.6: The CX pump and BX probe transitions from the same lower level in OODR spectroscopy.

polarisers. The output of a single mode dye laser is split into a strong pump beam, which is circularly or linearly polarized, and a weak, linearly polarized probe beam. The pump and probe beams pass in opposite directions through the heat pipe (see figure 1.5).

When the laser frequency is tuned to a molecular transition, molecules with a near zero velocity component parallel to the beams can interact with both the pump and the probe. The molecules are orientated by the polarized pump beam, and then modify the polarization of the probe beam so that part of the probe beam passes through the crossed polarisers, and is detected by a photomultiplier.

In OODR, the frequency of the laser is kept fixed on a known transition (in this

case, the C-X transition). A beam from a second laser passes through the heatpipe anticollinear to the pump beam. The second laser is scanned; when it is in resonance with a transition from the same lower level (in this case, a B-X transition), it depletes the population of this lower level, and the signal from the probe beam decreases (figure 1.6).

Although the singlet spectra have been well studied previously, we have studied them in order to optimise our experimental set-up and develop methods of analysis for the data. The conditions under which the spectra of [29] were taken are somewhat different to those we have used; Diemer et al. use a heatpipe at a temperature of 610K, while we use a cold molecular beam, giving a temperature of $\sim$ 10K.

1.3.2 Triplet spectra

The first observation of the triplet spectra was by Walter and Barratt in 1928 [36]. Although they were able to see different fine structure components, no vibrational structure is reported.

In recent times, with the benefit of laser spectroscopy techniques, the same triplet spectra have been studied by two groups, Diemer et al. [28] in 1991, and Kim and Yoshihara [26] in 1993. Diemer et al. used laser induced fluorescence (LIF) of a supersonic caesium/argon beam (the same technique used in this work), to record triplet spectra. However, they were unable to obtain LIF signals using a single mode laser, and so used a broadband dye laser of bandwidth $\Delta\nu \approx$ 2GHz. A rotational temperature for the singlets under these conditions was reported to be 10K.

Kim and Yoshihara used a resonance-enhanced two-photon ionization (RE2PI) method. They produced molecules in a pulsed supersonic beam, with a rotational temperature of about 1K. The molecules were excited using a dye laser, as in the LIF technique. But instead of detecting the fluorescence with a photomultiplier, the molecules in the excited state were photoionized with photons from a cw argon laser. The ions were detected using a mass spectrometer tuned to the mass of the caesium ions. The dye laser used in this case was a pulsed dye laser, with a line width of 0.2cm^{-1} (6GHz). The RE2PI technique has the advantage of a good signal to noise ratio, but the line width of the laser is once again large.

There is a significant disagreement between the two sets of results. Kim and Yoshihara find a discrepancy of up to 20cm^{-1} between their vibrational band positions and those found by Diemer et al. Kim and Yoshihara suggest that this could be

due to a misassignment of the vibrational quantum numbers, but this still leaves a discrepancy. In addition, neither group were able to resolve rotational structure. We have resolved the discrepancy between these results, and have observed structure which we believe to be rotational in origin, although not well resolved.

1.4 Layout of the thesis

The theory of molecular structure and spectra related to the study of caesium dimers is presented in chapter 2. In chapter 3, the methods of deducing interatomic potentials from molecular spectra are discussed. The calculation of scattering lengths from the potentials is reviewed, with a discussion of the validity of using the scattering length model of cold collisions.

The experimental methods are described in chapter 4. Our molecular spectra for the singlet and triplet cases are presented in chapter 5. We develop a model to reproduce the observed singlet spectra, and discuss the first spectra of the caesium dimer triplet ground state to be observed with single-mode laser resolution. Finally, in chapter 6 we present a summary of the results and suggestions for further work.

Chapter 2

Molecular structure and spectra

2.1 Molecular Structure

At first glance, even the smallest diatomic molecule appears extremely complex. Whereas in atoms we are concerned only with the motion of electrons around a nucleus, in a molecule we have to consider the motion of the two nuclei as well as that of the electrons. However, approximations can be made which simplify the problem greatly. The mass of the nuclei is much greater than that of the electrons. This means that the nuclear motion is very much slower than the electronic motion, and so as a first approximation, the two can be treated separately [37]. This is known as the Born-Oppenheimer approximation. We will first look at the nuclear motion in this approximation, and then move on to look at the effects of coupling between nuclear and electronic motion.

2.2 Born-Oppenheimer approximation

In the Born-Oppenheimer approximation, the wavefunction representing the molecule can be separated into an electronic and a nuclear component

$$\Psi = \psi_{elec}(\mathbf{r}, R)\psi_{nuc}(R, \theta, \phi) \tag{2.1}$$

where $\mathbf{r}$ represents the coordinates of the electrons, R the separation of the nuclei, and θ and ϕ the orientation of the internuclear axis (the line joining the two nuclei). Solving Schrödinger's equation for the electronic motion and nuclear repulsion for a particular separation R gives the total energy of the system excluding nuclear motion,

E_{elec}. Finding E_{elec} for each value of R gives an *interatomic potential curve.* This can then be used as the potential in Schrödinger's equation for the nuclear motion. A typical interatomic potential in a molecule has the form shown in figure 2.1. At very large distances, the forces between atoms are negligible, and the energy is just the sum of the atomic energies. As the atoms come together, the Van der Waals interaction leads to an attractive force between the atoms. At very small separations on the other hand, there is a strong repulsive force as the electron clouds of the two atoms overlap and the positive nuclear charges are no longer well screened by the electrons. At intermediate separations there is an attractive potential well, and corresponding to the bottom of this well an equilibrium separation for which there is no net force. Interatomic potentials will be discussed more fully in section 3.1.

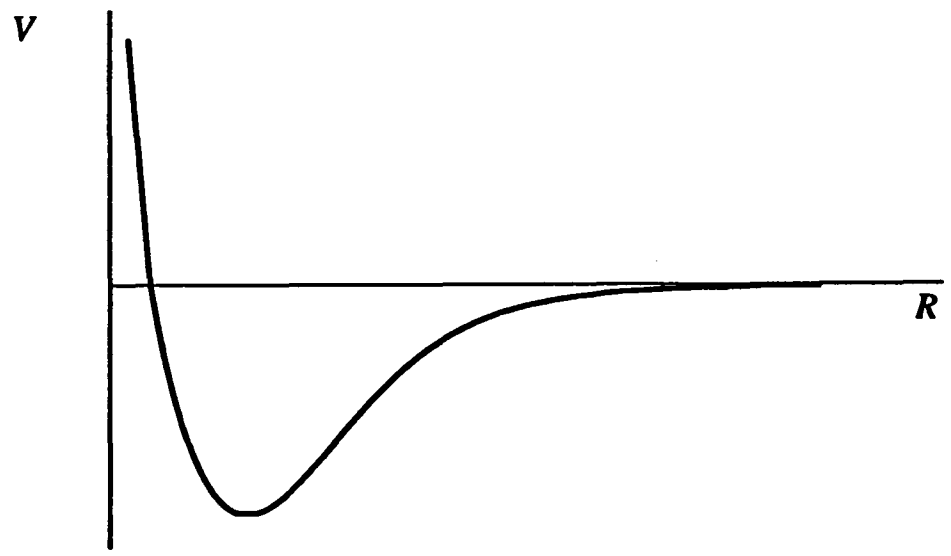

Figure 2.1: The typical form of an interatomic potential

The nuclear motion can be separated into two components as shown in figure 2.2 [37]. The atoms can vibrate relative to each other along the nuclear axis, and the molecule can rotate about an axis passing through the centre of gravity and perpendicular to the internuclear axis [38]. The energies of vibrational motion turn out to be of order 1000 times greater than the rotational energies, so it is a good approximation to treat the rotational and vibrational motion independently. This is often included in the statement of the Born-Oppenheimer approximation, giving the wavefunction as

$$\Psi = \psi_{elec}(\mathrm{r}, R)\psi_{vib}(R)\psi_{rot}(\theta, \phi) \tag{2.2}$$

and the total energy of the molecule is then a sum of the components

$$E_{tot} = E_{elec} + E_{vib} + E_{rot} \tag{2.3}$$

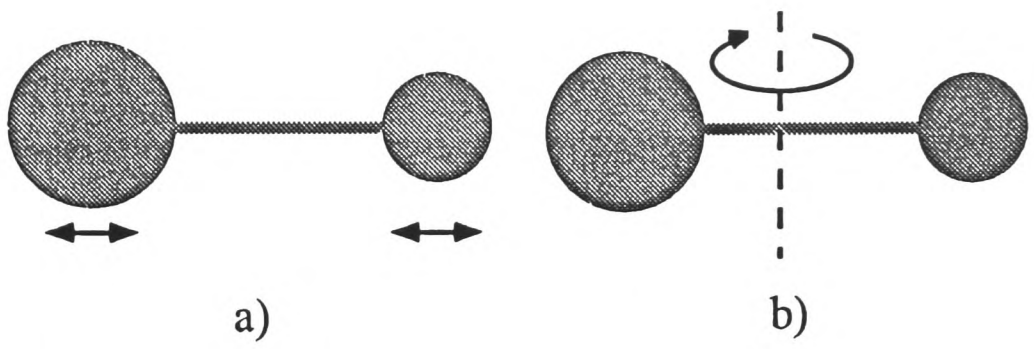

Figure 2.2: a) Vibrational motion of a molecule. b) Rotational motion of a molecule.

2.2.1 Nuclear motion - rotation and vibration

The rotational and vibrational motion can be found by solving the nuclear part of Schrödinger's equation in the presence of an interatomic potential. However, we can gain a better visualisation of the behaviour of the molecule if we treat it classically in the first instance.

Rotational energy levels

Classically, the energy of rotation of a rigid body is given by

$$E_{rot} = \frac{P^2}{2I} \tag{2.4}$$

where P is the angular momentum of the system, and I is the moment of inertia.

$$I = \mu R^2 \tag{2.5}$$

where μ is the reduced mass, and R is the separation of the nuclei. This is known as the *rigid rotator model.* To translate this into a quantum mechanical picture, we can use the result

$$P^2 = \hbar^2 J(J+1) \tag{2.6}$$

where J is the rotational quantum number. This gives the quantum mechanical expression for the rigid rotator,

$$E_{rot} = \frac{\hbar^2}{2\mu R^2} J(J+1) \tag{2.7}$$

We will follow the usual spectroscopic convention of expressing energies as wavenumbers, $\overline{\nu} = \frac{E}{hc}$ where $\overline{\nu}$ is given in cm^{-1}. We then have the *rotational term*

$$F(J) = \frac{E_{rot}}{hc} = B_e J(J+1) \tag{2.8}$$

where B_e is the equilibrium rotational constant.

Vibrational energy levels

In reality, the atoms are not joined rigidly. The molecule can also vibrate, as if its atoms were joined by a spring. The simplest model for vibration of two molecules is the simple harmonic oscillator. The interatomic potential can be approximated by an expansion about its minimum, the first term being the harmonic potential,

$$U(R) = \frac{1}{2}k(R - R_e)^2 \tag{2.9}$$

where R_e represents the equilibrium value of R. This gives us a series of energy levels [39]

$$E_{vib} = \frac{h}{2\pi}\sqrt{\frac{k}{\mu}}(v + \frac{1}{2}) \tag{2.10}$$

which, following the convention of using wavenumbers, can be written as

$$G(v) = \omega(v + \frac{1}{2}) \tag{2.11}$$

where $\omega = \frac{1}{2\pi c}\sqrt{\frac{k}{\mu}}$.

But real interatomic potentials are not harmonic, and so further terms of the expansion are required. In particular, we need to take into account that the potential is not symmetric; the midpoint of the potential well moves to higher R for higher energies. A better representation of the potential is a *Morse* potential. This analytical potential is given by

$$U(R) = \epsilon\left\{\left[1 - e^{-a(R-R_e)}\right]^2 - 1\right\} \tag{2.12}$$

Solving Schrödinger's equation for this potential gives the vibrational energy levels

$$G(v) = \omega_e(v + \frac{1}{2}) + \omega_e\chi_e(v + \frac{1}{2})^2 \tag{2.13}$$

where $\omega_e\chi_e$ is the *anharmonicity constant.* In the special case of the Morse potential, this is the exact solution of Schrödinger's equation. For a general potential, there will be higher order terms (section 2.2.2).

The spring-like forces between the atoms also affect the rotational motion. As the molecule rotates faster, the atoms tend to move further apart, as a greater force is required to maintain the circular motion. We can take this into account if as above we consider the atoms to be joined by a spring with force constant k. Then as well as the kinetic energy of rotation, there is also potential energy stored in the spring when stretched:

$$E_{rot} = \frac{\hbar^2}{2\mu R_e^2}J(J+1) - \frac{1}{2}k(R - R_e)^2 \tag{2.14}$$

Equating the necessary centripetal force to the tension in the spring gives

$$F = -\mu\omega^2 R = -\frac{P^2}{\mu R^3} = -k(R - R_e) \tag{2.15}$$

substituting in equation 2.14 gives

$$E_{rot} = \frac{P^2}{2\mu R_e^2} + \frac{P^4}{2\mu^2 R_e^6 k} \tag{2.16}$$

Using equation 2.6 gives

$$E_{rot} = \frac{\hbar^2}{2\mu R_e^2} J(J+1) - \frac{\hbar^4}{2\mu^2 R_e^6 k} J^2(J+1)^2 \tag{2.17}$$

which can be written as

$$F(J) = B_e J(J+1) - D_e J^2(J+1)^2 \tag{2.18}$$

where D_e is the centrifugal distortion constant, which is generally much smaller than B_e.

For an arbitrary potential, there will generally also be higher order correction terms. These will be discussed further in section 2.2.2.

2.2.2 Coupling of rotational and vibrational motion

So far we have treated the vibrational and rotational motion independently. In practice, the molecule will both rotate and vibrate. If we could neglect the interaction between the vibration and rotation, then the energy would be given by a sum of the terms from equation 2.18 and equation 2.13 i.e.

$$T(v, J) = B_e J(J+1) - D_e J^2(J+1)^2 + \omega_e(v + \frac{1}{2}) + \omega_e\chi_e(v + \frac{1}{2})^2 \tag{2.19}$$

However, a more accurate treatment requires that we take into account the fact that the internuclear distance changes as the molecule vibrates and so we would expect the rotational constant to change.

It can be shown [38] that we can use a mean value of the rotational constant B_v, where

$$B_v = \frac{\hbar}{2\mu c}\left[\frac{1}{R^2}\right] \tag{2.20}$$

and $\left[\frac{1}{R^2}\right]$ is the mean value of $\frac{1}{R^2}$ during the vibration. Since the mean value of R increases with increasing vibrational quantum number due to anharmonicity, B_v is smaller than the equilibrium value B_e, and to a first approximation is given by

$$B_v = B_e - \alpha_e(v + \frac{1}{2}) + \ldots \tag{2.21}$$

Similarly, the mean centrifugal distortion constant D_e is given by

$$D_v = D_e + \beta_e(v + \frac{1}{2}) + \ldots \tag{2.22}$$

Using these modified rotational constants, we obtain the energy levels of a vibrating rotator

$$T(v, J) = \omega_e(v + \frac{1}{2}) + \omega_e\chi_e(v + \frac{1}{2})^2 + B_vJ(J + 1) - D_vJ^2(J + 1)^2 \tag{2.23}$$

It is this expression which we have used to fit our singlet spectra in section 5.2.2. Although this is still an approximation, we have found that it is adequate to fit our spectra to within experimental error.

The Dunham Expansion

Although we have found the expression in equation 2.23 adequate for fitting our spectra, it is worth mentioning the extension to the Dunham expansion, which allows us to fit to vibrational and rotational levels of an arbitrary potential.

The Dunham expansion [40] represents the vibrating rotator as a sum of terms in v and J:

$$T(v, J) = \sum_{ik} Y_{ik}(v + \frac{1}{2})^i(J(J + 1))^k \tag{2.24}$$

The constants Y_{ik} are the *Dunham coefficients.* This is a generalisation of equation 2.23. If we take the Dunham expansion for the case where $0 \leq i \leq 2, 0 \leq k \leq 2$, we can see the correspondence between the Dunham coefficients and the constants of equation 2.23:

$$\begin{aligned} T(v, J) = Y_{00} + Y_{10}(v + \tfrac{1}{2}) + Y_{20}(v + \tfrac{1}{2})^2 + (Y_{01} + Y_{11}(v + \tfrac{1}{2}) + Y_{21}(v + \tfrac{1}{2})^2)J(J + 1) \\ +(Y_{02} + Y_{12}(v + \tfrac{1}{2}) + Y_{22}(v + \tfrac{1}{2})^2)J^2(J + 1)^2 \end{aligned} \tag{2.25}$$

In the approximation that we can neglect terms the terms containing $Y_{30}, Y_{40}, \ldots$ and terms containing $Y_{i3}, Y_{i4}, \ldots$, we obtain the relationships

$B_v \leftrightarrow \sum_i Y_{i1}(v + \frac{1}{2})^i$
$D_v \leftrightarrow -\sum_i Y_{i2}(v + \frac{1}{2})^i$
$\omega_e \leftrightarrow Y_{10}$
$\omega_e\chi_e \leftrightarrow Y_{20}$

Although our experimental data is not sufficiently accurate to require terms additional to those in equation 2.23, we have found it helpful to convert the Dunham coefficients for the singlet states given by Weickenmeier et al. [25] and by Diemer et al. [29] to the form of equation 2.23 to give our initial values for fitting a model to the singlet spectra (section 5.2.3). It has also been necessary to calculate line positions from the Dunham coefficients of [29] and [25] in order to compare the positions with our own results.

2.3 Electronic states of molecules

So far we have dealt with the vibrational and rotational motion of the molecule. We will now consider the possible electronic states of the molecule. As in the LS coupling scheme for atoms, the orbital angular momenta of the individual electrons couple to give **L**, the total orbital angular momentum, and the spins of the individual electrons couple to give **S**, the total spin angular momentum. These may then couple in different ways to each other and to the rotation of the molecule depending on the comparative strength of the interactions.

Five coupling cases may be distinguished, known as Hund's cases (a) to (e). However, we shall consider only the three of these((a) to (c)) which are relevant to the current work.

Hund's Case (a)

Unlike an atom, a diatomic molecule has an axis in space, defined by the line between the two nuclei (the Z axis). This reduces the symmetry of the molecule in an analogous way to applying a strong electric field to an atom. If the coupling between **L** and the field along the internuclear axis is stronger than between **L** and the molecular rotation, **L** precesses about the internuclear axis. Hence the projection onto the internuclear axis, M_L, is conserved and is a good quantum number. For an electric field, unlike a magnetic field, the states having projected orbital angular momentum quantum numbers M_L and $-M_L$ are degenerate. It is therefore conventional to consider

$$\Lambda = |M_L| \tag{2.26}$$

Value of Λ	0	1	2	3
Label	Σ	Π	Δ	Φ

Table 2.1: Symbols for values of Λ.

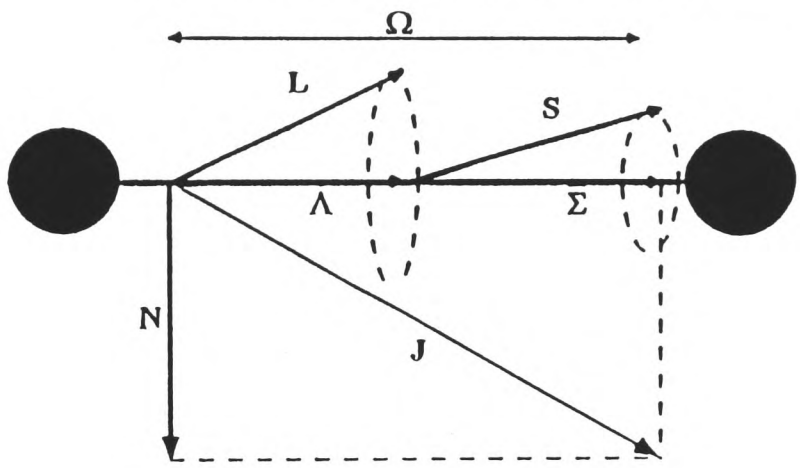

Figure 2.3: Vector diagram for Hund's case (a)

In analogy with atomic spectroscopy, capital Greek letters are associated with the different values of Λ, as shown in table 2.1. If $\Lambda \neq 0$, this orbital angular momentum produces an internal magnetic field along the internuclear axis. The spin S couples to this field, precessing about the internuclear axis with component $M_S\hbar$ (the quantum number is conventionally given the symbol Σ). Σ may take the $2S+1$ values

$$\Sigma = S, S-1, S-2, ..., -S \tag{2.27}$$

As in atoms, the molecules are labelled according to the value of $2S+1$ as a superscript e.g. $^1\Sigma, ^3\Pi$. States are also described as being singlet or triplet states, corresponding to $2S+1 = 1, 3$ respectively.

The magnitude of the total electronic angular momentum is given by

$$\Omega = |\Lambda + \Sigma| \tag{2.28}$$

For a state of a given Λ and S there are $2S+1$ different values of $\Lambda + \Sigma$. Due to the interaction of S with the magnetic field from the orbital motion of the electrons, states with different values of $\Lambda+\Sigma$ have different energies (analogously to the coupling between L and S in atoms). As for J in atoms, the value of Ω is given as a subscript e.g. $^3\Pi_{0,1,2}$.

In section 2.3, it was stated that states with $\Lambda \neq 0$ are twofold degenerate. In the $\Omega = 0$ case, the degeneracy is only approximate, and finer interactions lead to a

slight splitting into two states. Ω remains well defined in the rotating molecule. The rotational motion, with angular momentum N, and the electronic angular momentum Ω couple to give a resultant J, i.e.

$$\mathbf{J} = \Omega + \mathbf{N} \tag{2.29}$$

Since J cannot be smaller than its component Ω, then for a given quantum number Ω, J can take values

$$J = \Omega, \Omega + 1, \Omega + 2, ... \tag{2.30}$$

A vector diagram for Hund's case (a) is given in figure 2.3. The rotational energy is then given by (neglecting centrifugal stretching)

$$F(J) = B_v[J(J+1) - \Omega^2] \tag{2.31}$$

This is the same as the energy for a rigid rotor except for an additive constant. B_v has the same value for each fine structure (Ω) component as long as the fine structure splitting remains small. Hence the set of rotational levels for each fine structure component is identical except for an additive constant. The energy levels of the molecule obeying case (a) are well represented by equation 2.23.

Hund's Case (b)

When $\Lambda = 0$, and $S \neq 0$, as is the case for the triplet ground state of Cs_2, there is no internal magnetic field to couple S to the internuclear axis. This means that Σ and Ω are not defined. Hund's case (b) also arises in light molecules where $\Lambda \neq 0$, but the coupling of S to the internuclear axis is very weak. In this case, the rotation angular

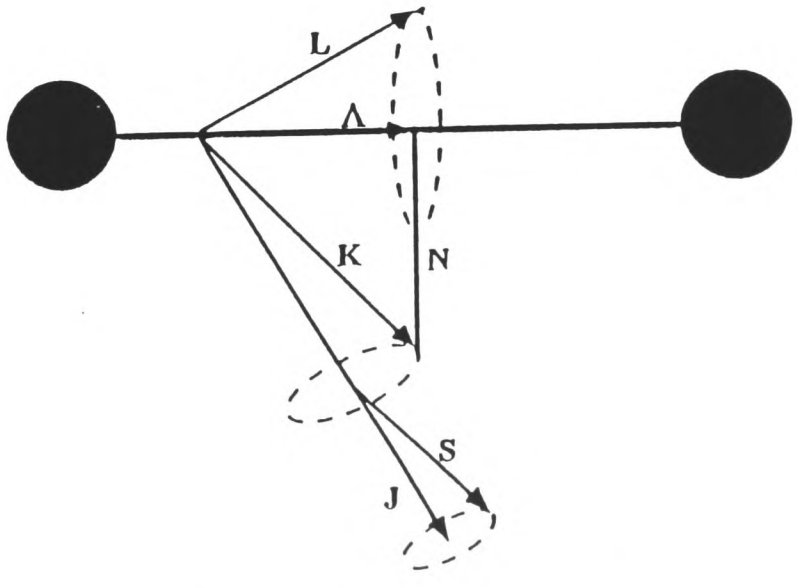

Figure 2.4: Vector diagram for Hund's case (b)

momentum **N** couples to **Λ** (if non-zero) to produce a resultant **K**, the total angular momentum apart from spin. The corresponding quantum number K takes values

$$K = \Lambda, \Lambda + 1, \Lambda + 2 ... \tag{2.32}$$

K and **S** then couple to give a total angular momentum **J**. A vector diagram for Hund's case (b) is given in figure 2.4.

The possible values of J are, from the normal rules of angular momentum addition,

$$J = |K - S|, |K - S| + 1, ...(K + S) \tag{2.33}$$

Each level of a given K therefore splits into $2S+1$ components (except where $K < S$). Thus the rotational levels are almost the same as those given by equation 2.23 except that they are very finely spaced multiplets.

Hund's case (c)

Especially in the case of heavier molecules, the interaction between **L** and **S** may be stronger than that between **L** and the internuclear axis. In this case **L** and **S** couple to give a resultant $\mathbf{J_a}$, which then couples to the internuclear axis with a projection **Ω**. The component **Ω** then couples to the rotational angular momentum **N** as in case (a), giving the same formula for the rotational energy levels. However, since **Λ** and **Σ** are no longer defined, a different notation to describe the electronic states is appropriate. The case (c) states are labelled using the notation $^{2S+1}\Omega$. A vector diagram for Hund's case (c) is given in figure 2.5.

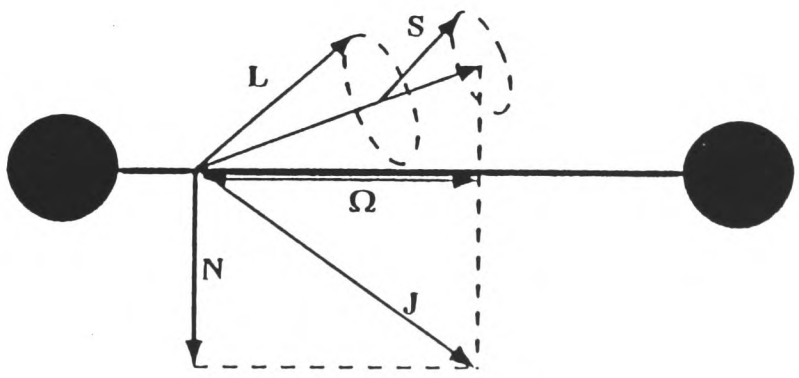

Figure 2.5: Vector diagram for Hund's case (c).

2.3.1 Other symmetry properties of the diatomic molecule

In a diatomic molecule, any plane through the internuclear axis is a plane of symmetry. For a non-degenerate state ($\Lambda = 0$, i.e., a Σ state, or $\Lambda \neq 0$, $\Omega = 0$), the electronic eigenfunction can differ by at most a change of sign when reflected in such a plane. States where the sign stays the same are labelled $^+$, and those where it changes, $^-$.

For a homonuclear molecule, there is also a centre of symmetry at the point midway between the two nuclei. On inverting electronic coordinates with respect to this point, the electronic wavefunction must have odd or even parity. For even parity, i.e., no change of sign, the state is labelled as gerade, or g, and if odd, it is labelled as ungerade, or u.

Ground states are denoted by X, and higher states by other letters or numbers. Hence the triplet ground state in which we are interested is denoted by $x^3\Sigma_u^+$ [38].

Hund's cases applied to the caesium dimer

We are interested in four molecular states, $^1\Sigma_g^+$,$^1\,\Pi_u$,$^3\,\Sigma_u^+$ and $^3\Pi_g$. How do Hund's cases apply to these states? The two singlet states, $^1\Sigma_g^+$ and $^1\Pi_u$ have $S = 0$. We cannot distinguish between the cases, but we will use the case (a) notation for convenience. For the triplet ground state, $^3\Sigma_u+$, $\Lambda = 0$ while $S \neq 0$, and so Hund's case (b) applies. However, it is unlikely that we will be able to resolve the multiplet splittings, in which case equation 2.23 applies.

For the triplet excited state, $^3\Pi_g$ (in the Hund's case (a) notation), both Λ and$S$ are non zero, and so it is not obvious whether the state is better described by case (a) or (c). Since Cs_2 is a reasonably heavy molecule, it is likely that there is at least some case (c) character, and the best description is probably a mixture of the two. However, it is convenient to keep the case (a) notation. The rotational energy levels are as found in equation 2.23 apart from an additive constant.

2.4 Spectra of diatomic molecules

In the previous section, expressions were found for the electronic, vibrational and rotational energy levels of diatomic molecules.

The frequencies of spectral lines are found from the differences in energy between levels. In order to gain a full understanding of the spectra, however, we also need to take into account the selection rules for transitions, and their relative intensities.

The energies of the transitions are given by differences between energy levels given by equation 2.23:

$$\begin{aligned}
\overline{\nu} &= (Te' - Te'') && (2.34)\\
&+ (\omega'_e(v' + \frac{1}{2}) - \omega''_e(v'' + \frac{1}{2}) + \omega'_e\chi'_e(v' + \frac{1}{2})^2 - \omega''_e\chi''_e(v'' + \frac{1}{2})^2) && (2.35)\\
&+ (B'_v J'(J'+1) - B''_v J''(J''+1) - D'_v J'^2(J'+1)^2 + D''_v J''^2(J''+1)^2) && (2.36)
\end{aligned}$$

where the first term corresponds to the electronic structure, the second to the vibrational structure, and the third to the rotational structure. A change in electronic level will usually involve a change in vibrational and rotational state as well. The electronic component is generally of order 10^3 times the vibrational component, which in turn is 10^3 times the rotational component. Hence the observed electronic spectrum has a coarse structure of vibrational bands, with a fine structure due to rotational transitions.

2.4.1 Electronic spectra

All our caesium spectra involve transitions in which there is a change in the electronic state of the molecule, i.e., they are electronic spectra. As in atoms, electronic transitions in molecules typically correspond to frequencies in the visible, ultra-violet or near infra-red region of the electromagnetic spectrum. In the case of the caesium dimer, we observe singlet transitions at 765nm, and triplet transitions at 710nm, both wavelengths being on the red/infra-red border.

Selection rules in electronic spectra

In section 2.3 the quantum numbers appropriate to different coupling schemes were introduced. Just as for atoms, there are selection rules for molecules which only allow transitions for certain values of these quantum numbers. Some are independent of the coupling scheme, and others hold only for a particular coupling case.

The selection rules for electric dipole transitions can be found by evaluating the matrix elements of the electric dipole operator, $< \psi_f | e\hat{\mathbf{r}} | \psi_i >$, where $\hat{\mathbf{r}}$ is the usual schematic representation of the coordinates of the electrons.

General selection rules The selection rule for the total angular momentum J is

$$\Delta J = 0, \pm 1, J = 0 \not\leftrightarrow J = 0 \qquad (2.37)$$

This rule always holds for electric dipole radiation.

There are also general selection rules relating to the symmetries of the diatomic molecule:

$$+ \leftrightarrow -, + \not\leftrightarrow +, - \not\leftrightarrow - \tag{2.38}$$

and in the case of identical nuclei,

$$g \leftrightarrow u, g \not\leftrightarrow g, u \not\leftrightarrow u \tag{2.39}$$

Selection rules holding for certain coupling cases In addition to the general selection rules, there are also selection rules which hold only for certain of Hund's cases (a) to (c).

For case (a) and (b), where Λ is defined,

$$\Delta\Lambda = 0, \pm 1 \tag{2.40}$$

Hence $\Sigma - \Sigma, \Sigma - \Pi, \Pi - \Pi, \Pi - \Delta$,... transitions are all allowed, but $\Sigma - \Delta, \Sigma - \Phi$ etc are forbidden.

For Hund's cases (a) and (b)

$$\Delta S = 0 \tag{2.41}$$

Hence singlet - singlet and triplet - triplet transitions are allowed, while singlet - triplet transitions are forbidden. Since this selection rule holds rigorously only for cases (a) and (b), any departure from these coupling schemes may result in a relaxation of the selection rule, and it may be possible to observe intercombination (singlet - triplet) transitions. As stated in section 2.3.1, the triplet excited state $^3\Pi_g$ could have some case (c) character, and so intercombination lines are theoretically possible. However, they would be expected to be very weak, and we have made no attempt to observe them experimentally.

2.4.2 Vibrational structure of electronic spectra

The selection rules given above tell us which transitions between electronic states are allowed. There are no forbidden transitions between vibrational states, but some transitions are very weak because the dipole matrix elements are reduced because the Franck-Condon factors (the overlap integrals between the vibrational states) are very small. This will be discussed in more depth in section 2.5.3 below.

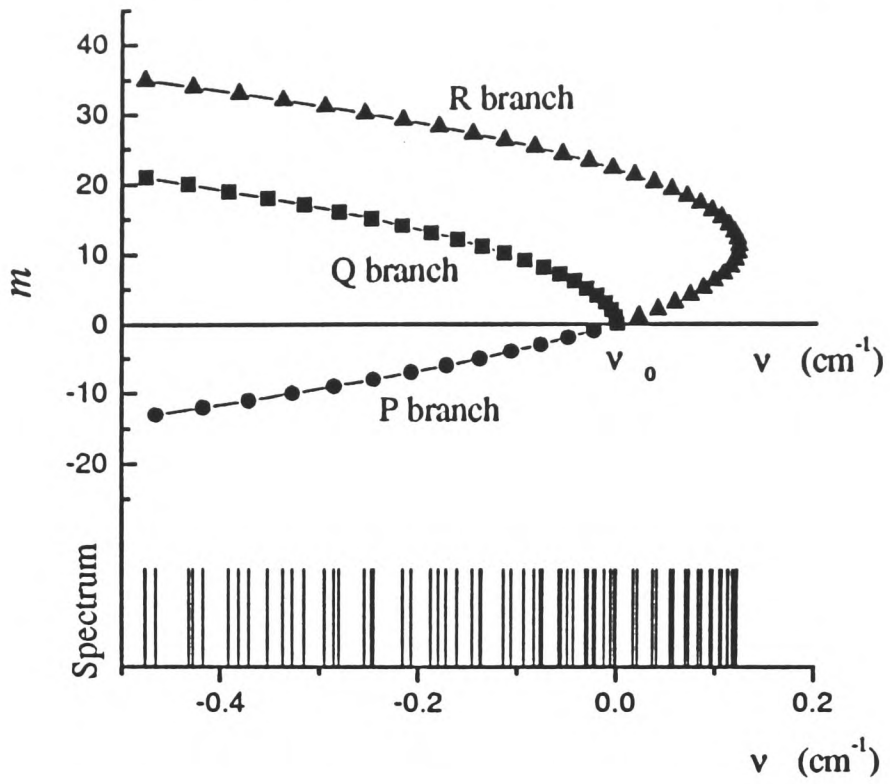

Figure 2.6: Fortrat diagram for 3-0 band of $B^1\Pi_u \leftarrow X^1\Sigma_g^+$ transition.

2.4.3 Rotational fine structure

As stated in section 2.4.1, the selection rule between angular momentum states is $\Delta J = 0, \pm 1$, unless $\Lambda = 0$ for both states, or $\Omega = 0$ for both states, in which case $\Delta J = \pm 1$. For the former case, the band consists of three rotational branches, the P, Q and R branch, corresponding to $\Delta J = -1, 0, 1$ respectively. In the latter case, the Q branch is missing.

Neglecting for the moment the terms in D_v in equation 2.36, the frequencies of the transitions in the three branches may be expressed as

$$\overline{\nu}_P = \overline{\nu}_0 - (B'_v + B''_v)J + (B'_v - B''_v)J^2 \quad (2.42)$$

$$\overline{\nu}_Q = \overline{\nu}_0 + (B'_v - B''_v)J + (B'_v - B''_v)J^2 \quad (2.43)$$

$$\overline{\nu}_R = \overline{\nu}_0 + 2B'_v + (3B'_v - B''_v)J + (B'_v - B''_v)J^2 \quad (2.44)$$

where J is the rotational quantum number of the lower state involved in the transition, and $\overline{\nu}_0$ is the electronic and vibrational contribution to the energy of the transition.

The P and R branches can be expressed by the single formula:

$$\overline{\nu} = \overline{\nu}_0 + (B'_v + B''_v)m + (B'_v - B''_v)m^2 \quad (2.45)$$

where $m = -J$ for the P branch, and $m = J+1$ for the R branch. Hence the rotational structure of the bands is parabolic in J. A plot of J against $\overline{\nu}$ is a *Fortrat parabola.* Figure 2.6 shows the Fortrat diagram for the $3-0$ singlet $B^1\Pi_u \leftarrow X^1\Sigma_g^+$ transition,

based on the rotational constants B_v derived from the Dunham coefficients of Diemer et. al. [28]. The equivalent plot for the Q branch, with $m = J$ is also included. The lines become closely spaced in frequency towards the high frequency, "blue" end of the band, forming a *band head.* The maximum rotational frequency, i.e., the band head, occurs when

$$m_{band\ head} = -\frac{B'_v + B''_v}{2(B'_v - B''_v)} \tag{2.46}$$

In this case, $B'_v < B''_v$, and the band head is in the R branch. If, on the other hand, $B'_v > B''_v$, then the band head occurs in the P branch, and the band head will be a low frequency limit.

2.5 Intensities in electronic spectra

In order to model our observed spectra theoretically, we need not only to know which lines are present and their frequencies, but also the relative intensities of the lines. This becomes most apparent when trying to fit a predicted spectrum to an observed rotational band, as discussed in section 5.2.2. Information on the relative intensities of the vibrational bands is also important, as it allows us to predict which bands we should be able to observe experimentally. An order of magnitude estimate of the absolute transition rate is sufficient.

There are two separate factors which normally determine the observed intensity of the transition. The first is the population of the initial level; the more molecules that are present in a given level, the more transitions there will be. The population depends on the temperature and the degeneracy of the level. The second factor is the transition probability for the transition, which is calculated from the dipole matrix element. Under certain assumptions, we find that the transition probabilities have a very simple form, which we will discuss below. However, as we will discuss in chapter 5, we have found it necessary to relax these assumptions and to take into account a third factor, the effect of optical pumping, to obtain a full agreement with experiment.

2.5.1 Population of states

Thermal distribution

In our treatment of intensities, we have used the Boltzmann distribution to give the distribution of molecules across both vibrational and rotational states.

The Boltzmann distribution gives the population of a level of energy E as

$$N \sim ge^{-\frac{E}{kT}} \tag{2.47}$$

where g is the degeneracy of the level. Taking the energy of the rotation energy level as $B_v J(J+1)$, the Boltzmann factor in the population is

$$N \sim ge^{-\frac{B_v J(J+1)}{kT_{rot}}} \tag{2.48}$$

where T_{rot} is the *rotational temperature.* This is found empirically when fitting the spectra. Similarly, for the vibrational levels, we have

$$N \sim e^{-\frac{\omega_e(v+\frac{1}{2})}{kT_{vib}}} \tag{2.49}$$

where T_{vib} is the vibrational temperature. The vibrational and rotational temperatures are generally different, due to the nature of the cooling process within the free-jet expansion.

The degeneracy g of the rotational level J is $(2J+1)$. However, this term is conventionally included in the Honl-London factors which are discussed in section 2.5.4.

Spin statistics

Another factor which must be taken into account in the discussion of intensities is the effect of nuclear spin. Although the coupling of nuclear spin with the electrons has negligible effect on the energy levels, the symmetry requirements will affect the intensities in a homonuclear molecule [37]. The result is that there is an additional factor in the intensities, with alternate lines having the ratio of intensities $\frac{(I+1)}{I}$, where I is the nuclear spin. For ^{133}Cs (the only naturally occurring isotope), the nuclear spin is $\frac{7}{2}$.

2.5.2 Transition probabilities

To find the transition probabilities for electric dipole radiation, we must calculate the matrix element for the transition. The transition probability can be written

$$W \propto |<\Psi_f|\mathbf{d}|\Psi_i>|^2 \tag{2.50}$$

where $\mathbf{d}$ is the electric dipole operator. We now make the Born-Oppenheimer separation

$$\Psi = \psi^e\psi^v\psi^r \tag{2.51}$$

The electronic wavefunction is expressed in a coordinate system which is fixed relative to the internuclear axis. We can then write the total wavefunction as

$$\Psi = \psi^e(\mathbf{r}, R)\psi^v(R)\psi^r(\theta, \phi) \tag{2.52}$$

where $\mathbf{r}$ represents the coordinates of all the electrons in the molecule fixed coordinate system. We first consider the factors in W arising from the first two terms, ignoring rotation. We obtain

$$| < \psi_f^e(\mathbf{r}, R)\psi^v(R)|\mathbf{d}|\psi_i^e(\mathbf{r}, R)\psi_i^v(R) > |^2 = | < \psi_f^e(\mathbf{r}, R)|\mathbf{d}|\psi_i^e(\mathbf{r}, R) > |^2 | < \psi_f^v(R)|\psi_i^v(R) > |^2 \tag{2.53}$$

The first term is the electronic dipole matrix element and the second is the vibration matrix element, or Franck-Condon factor. The rotational term which we have not included is a purely angular integral, which we will discuss in section 2.5.4.

Electronic transition probabilities

Although we are not generally concerned with the absolute transition probabilities, it is desirable to make an order of magnitude estimate.

If the two nuclei of the molecule were fixed, then the probability of a transition in the molecule should be of the same order as that for a similar electronic transition in an atom [38]. Introducing the nuclear motion does not change the total transition probability; the same total transition rate is just distributed over a number of lines.

For atoms, the spontaneous emission rate is given by [42]

$$A_{fi} = \frac{4}{3}\frac{1}{4\pi\epsilon_0}\frac{\omega_{fi}^3}{\hbar c^3}| < \psi_f|\mathbf{d}|\psi_i > |^2 \tag{2.54}$$

To give an order of magnitude estimate, we can put $| < \psi_f|d|\psi_i > |^2 \sim (ea_0)^2$ for an electric dipole transition, giving

$$A \sim \frac{1}{\hbar c^3}\frac{(ea_0)^2}{4\pi\epsilon_0}\omega^3 \tag{2.55}$$

and so $A \sim 10^8$ s^{-1}, and a lifetime $\tau \sim 10^{-8}$ s.

We would expect an absolute transition rate similar to this for molecules, but spread over the rotational and vibrational lines.

2.5.3 Franck-Condon Factors

Let us now consider the vibrational contribution to the transition probability, the Franck-Condon factor, $| < \psi_f^v|\psi_i^v > |^2$. This is the overlap integral between the

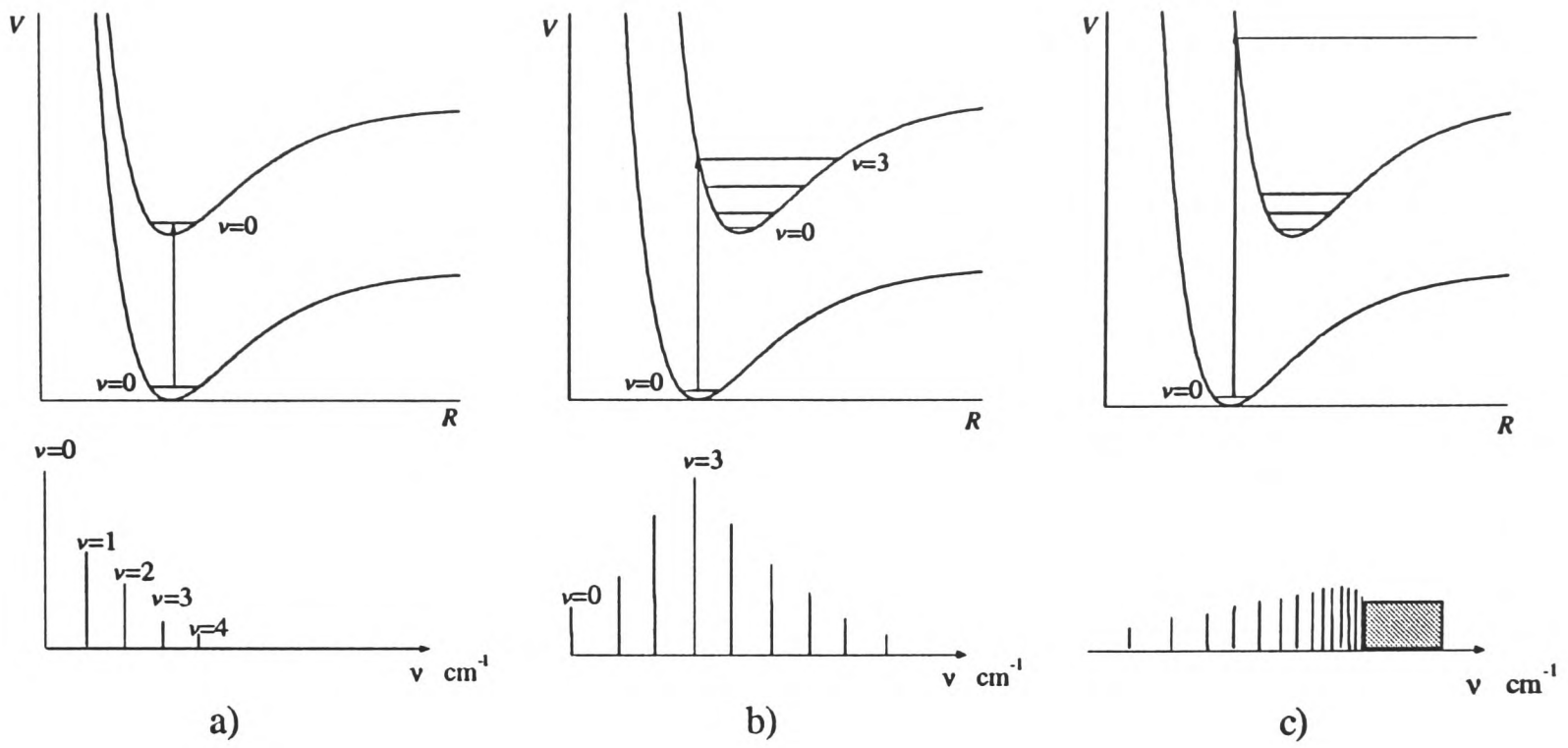

Figure 2.7: Potential curves and resulting intensity distributions illustrating three different possibilities under the Franck - Condon principle.

vibrational wavefunctions of the upper and lower states. This will be largest when the regions of maximum probability of the wavefunctions occur at similar R.

If the molecule is in its lowest vibrational state, then the maximum probability occurs at approximately the equilibrium separation. For excited vibrational states, the maximum probability occurs at the classical turning points. So from the ground state, the most likely transition is to an upper level with a classical turning point vertically above the equilibrium point for a transition from the ground state, or vertically above a classical turning point of the lower state if the transition is from an excited state.

If the potentials of the two electronic states have their minima at similar values of R, then the $v' = 0 \leftarrow v'' = 0$ transition will be strongest (figure 2.7 a). If the potentials have offset minima, then the transition to a higher value of v will be more probable e.g. the $v' = 3 \leftarrow v'' = 0$ transition in figure 2.7 b. If the potentials are offset by a large amount, then it is possible to have strong transitions to states above the dissociation limit, and a continuum is observed (figure 2.7 c). As well as transitions from $v'' = 0$, there will also be transitions from other vibrational levels of the lower state. However, these states will be less populated than the ground vibrational state (as discussed in section 2.5.1), especially at low temperatures, and so the bands will

usually be quite weak. Such bands from $v'' \neq 0$ are known as hot bands, since they generally only appear at high temperatures.

2.5.4 Relative transition probabilities for rotational states

The rotational term in the probability, as mentioned in section 2.5.2 gives the rotational transition probabilities and polarization dependence. It is the relative rotational intensities which are of most interest in this work, as we wish to fit a theoretical profile to a single vibrational band, for which we need an expression for both line positions and intensities for the rotational lines.

Honl-London Factors

Under certain approximations, the relative rotational transition rates are given by the *Honl-London* factors.

We consider a molecule in an initial rotational state (J, m). When the molecule absorbs a photon, a transition to an upper state $(J + \Delta J, m)$ will occur, where $\Delta J = -1, 0, 1$ corresponding to the P,Q or R branch respectively. The molecule will then emit a photon, falling back to a lower state which is not necessarily the initial state. The two simplifying assumptions to be made are:

- We only observe each molecule for one excitation cycle. This means we are only interested in the number of photons emitted, which corresponds to the number absorbed, so we only need to calculate the rate for upward transitions. Hence we are not concerned with the final state of the molecule. In reality, each molecule may go through many cycles, and so the final states become important as we have to consider optical pumping (section 5.3).

- We assume that we observe equal proportions of the photons emitted for each possible downwards transition, and that we are not concerned with their polarization. Since emitted photons are emitted preferentially in different directions, and with different polarisations depending on the transition, this would experimentally require us to detect photons over all solid angle. In reality, we only have a small area detector (again, we discuss this in section 5.3).

Making these simplifications, the rate at which we observe photons will be proportional to the absorption rate.

For a transition with $\Lambda'' = 0, \Lambda' = 1$, in a Hund's case a) approximation,the relative transition probabilities are given by [38]

$$\begin{aligned} \text{P branch} &: \frac{J''-1}{4} \\ \text{Q branch} &: \frac{2J''+1}{4} \\ \text{R branch} &: \frac{J''+2}{4} \end{aligned} \tag{2.56}$$

where J'' is the rotational quantum number of the lower state. These are the Honl-London factors.

As mentioned above, we will extend this analysis in chapter 5 by looking at the agreement of the model with experimental data.

Chapter 3

Interatomic potentials and scattering lengths

In chapter 2, the concept of an interatomic potential was introduced to explain how the discrete vibrational and rotational levels of a molecule arise from the electronic interactions between the two atoms. In this chapter, we will look more closely at the detailed shapes of these potentials, and how we can deduce the interatomic potentials and hence scattering lengths from spectral data. We apply our analysis to the case of the caesium ground state triplet potential.

3.1 Interatomic forces

As discussed briefly above, the key features of an interatomic potential are :

- At long range, the forces between atoms are attractive. At very large distances, the energy tends to the electronic energy of the isolated atoms.
- At short distances, there are strong repulsive forces between atoms. These are due partially to the electrostatic repulsion between the overlapping electron clouds, and partially due to the electrostatic repulsion between nuclei [43].
- In the intermediate region, there may be a potential well, at the bottom of which the atoms have an equilibrium separation.

Let us now look at the approximate functional forms which can be used for such a potential.

3.1.1 Long range potential - the Van der Waals interaction.

How does the force of attraction between two uncharged atoms at large distances arise? Neither atom is charged, and neither atom has a permanent dipole moment.

The answer lies in the *Van der Waals* attraction between atoms, which may be understood using the following picture. We can think of the electrons in each atom as being permanently in motion. As the electrons move, it is likely that they will not be distributed symmetrically. This will lead to a small instantaneous dipole moment D, constantly changing in direction and magnitude. Since there is no overall permanent dipole, its time averaged value must be zero. Hence for each atom the expectation value of the dipole moment $< \psi|D|\psi >$ must be zero.

The instantaneous interaction between two such atoms is given by the dipole-dipole interaction $\frac{D_a.D_b}{R^3}$, where D_a is the dipole moment of atom a, and D_b the dipole moment of atom b. To find the net contribution, averaged over time, to the potential between the atoms, we must treat the instantaneous interaction as a perturbation.

Using perturbation theory (the approach is not limited by the above picture), the first order perturbation energy is given by

$$\Delta E(1) = \frac{1}{R^3} < \psi_a\psi_b|D_a.D_b|\psi_a\psi_b > \tag{3.1}$$

$$= \frac{1}{R^3} < \psi_a|D_a|\psi_a >< \psi_b|D_b|\psi_b > \tag{3.2}$$

$$= 0 \tag{3.3}$$

since each expectation value is zero. The first non-vanishing perturbation energy is the second-order correction,

$$\Delta E(2) = \frac{1}{R^6}\sum_{j\neq 0}\frac{< \psi_0|D_a.D_b|\psi_j >< \psi_j|D_a.D_b|\psi_0 >}{E_0 - E_j} \tag{3.4}$$

where $\psi_0 = \psi_a\psi_b$ and ψ_j are the wavefunctions of the intermediate states.

Hence the long range potential from the Van der Waals interaction has the form:

$$U(R) \sim -\frac{1}{R^6} \tag{3.5}$$

As well as the induced dipole-dipole interaction, there will also be higher order interactions e.g. dipole-quadrupole, quadrupole-quadrupole. These will lead to higher order terms, giving

$$U(R) = -\frac{C_6}{R^6} - \frac{C_8}{R^8} - \frac{C_{10}}{R^{10}}\ldots \tag{3.6}$$

For the case of like atoms in different states, where there is an allowed transition between the states of the two atoms, a degeneracy is introduced. In this case, there is a first order interaction, and the first term in the energy is a $\frac{1}{R^3}$ term.

Values of the constants C_6...can be calculated theoretically [44], or found experimentally (e.g. [25])

It is less easy to deduce the form of the short range repulsive potential; normally a function is chosen which shows the required rapid increase as $R \rightarrow 0$, and which has a simple analytical form. One form which is used is in the *Lennard-Jones* potential, which is a sum of the short range and long range interactions:

$$U(R) = \epsilon \left\{ \frac{6}{n-6} \left(\frac{R_e}{R}\right)^n - \frac{n}{n-6} \left(\frac{R_e}{R}\right)^6 \right\} \tag{3.7}$$

Typically a value of $n = 12$ is used. This potential has the advantage that the long range part has the $1/R^6$ Van der Waals form.

Another widely used analytical potential is the Morse potential:

$$U(R) = \epsilon \left\{ 1 - e^{-\beta(R-R_e)} \right\} \tag{3.8}$$

The Morse potential has the advantage that it allows exact solutions of Schrödinger's equation, to give

$$G(v) = (v + \frac{1}{2})\omega_e - (v + \frac{1}{2})^2 \omega_e \chi_e \tag{3.9}$$

where $\omega_e = \beta\sqrt{\frac{\epsilon\hbar}{\pi c\mu}}$, and $\omega_e\chi_e = \frac{\hbar\beta^2}{4\pi c\mu}$, which is the same as the expression in equation 2.2.1. But since the long range part is exponential rather than the $1/R^6$ form, it is less satisfactory at long range.

3.2 The Rydberg-Klein-Rees Inversion method

While these analytical forms are a useful approximation, and may fit well to experimental data over a limited range, a more general method of deducing the potential from spectroscopic data is required. One such method is the Rydberg-Klein-Rees (RKR) inversion method. This is a semi-classical approach, which has been applied previously in the group, in the work on Hg-Ar [45].

The RKR method allows the classical turning points R_L and R_R to be found for an energy V' in a potential well $U(R)$, if the positions of the vibrational and rotational energy levels are known up to the energy V' [43]. Figure 3.1 shows part of the potential energy curve. The shaded area S in figure 3.1 is given by

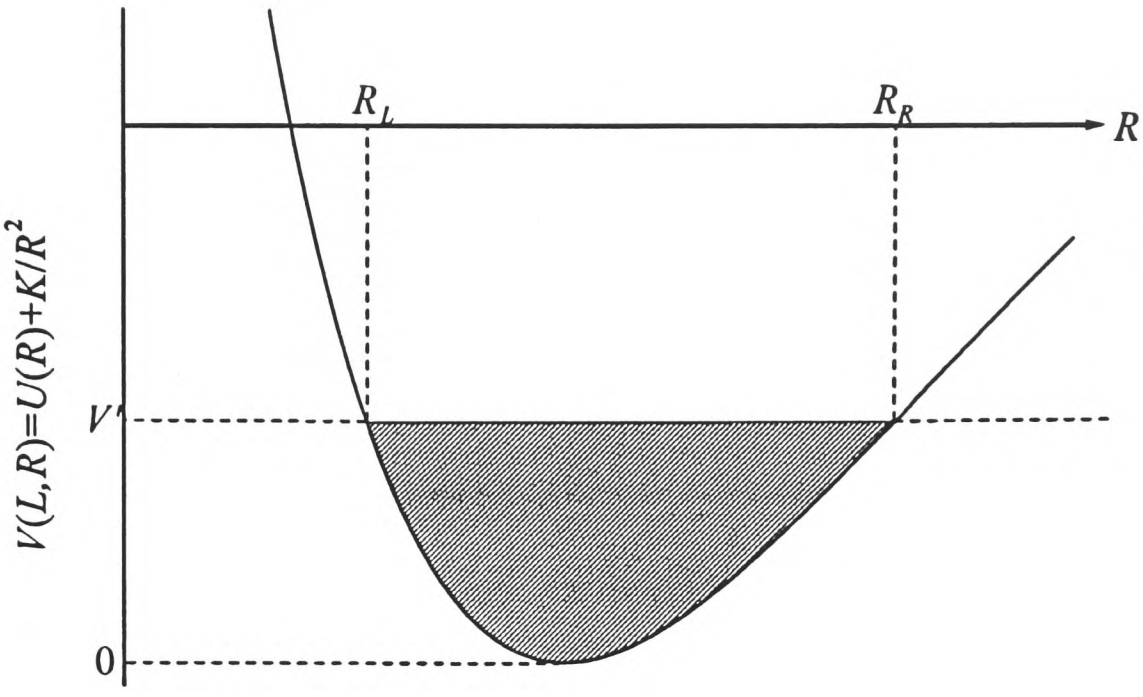

Figure 3.1: Potential energy curve and parameters used in RKR analysis

$$S = \int_{R_L}^{R_R} (V' - V) dR \tag{3.10}$$

V is the effective potential $U(R) + KR^{-2}$, where the second term is the centrifugal energy, dependent on l, the orbital angular momentum. Differentiating with respect to V' and then with respect to K gives

$$\left(\frac{\partial S}{\partial V'}\right)_K = \int_{R_L}^{R_R} dR = R_R - R_L \tag{3.11}$$

$$\left(\frac{\partial S}{\partial K}\right)_{V'} = -\int_{R_L}^{R_R} \frac{dR}{R^2} = \frac{1}{R_R} - \frac{1}{R_L} \tag{3.12}$$

Let the total energy of the system be $E(I, K)$, where I is the vibrational phase integral $\oint p dq$, and K is the angular momentum phase integral $\oint p_l d\theta$. According to the WKB approximation [43], these are quantised according to

$$\oint p dq = I = h(\nu + \frac{1}{2}) \tag{3.13}$$

$$\oint p_l d\theta = K = l(l+1)(\hbar^2/2\mu) \tag{3.14}$$

Differentiating I with respect to E, and then using a standard integral [43] gives another expression for S

$$S = \left(\frac{2}{\mu\pi^2}\right)^{\frac{1}{2}} \int_0^{I'} (V' - E(I, K))^{\frac{1}{2}} dI \tag{3.15}$$

Differentiating with respect to V', and comparing with equation 3.11 gives

$$R_R - R_L = \left(\frac{1}{2\pi^2\mu}\right)^{\frac{1}{2}} \int_0^{I'} \frac{dI}{\{V' - E(I,K)\}^{\frac{1}{2}}} \tag{3.16}$$

and with respect to K gives

$$\frac{1}{R_R} - \frac{1}{R_L} = \left(\frac{1}{2\pi^2\mu}\right)^{\frac{1}{2}} \int_0^{I'} \frac{(\partial E/\partial K)dI}{\{V' - E(I,K)\}^{\frac{1}{2}}} \tag{3.17}$$

Since we are interested in the case when $l = K = 0$, we can therefore use

$$E(I,K) = E(I,0) \tag{3.18}$$

$$\left(\frac{\partial E}{\partial K}\right)_{K=0} = B_v \frac{2\mu}{\hbar^2} = \frac{1}{\overline{R}_v^2} \tag{3.19}$$

where B_v is the rotational constant, and $\overline{R}_v$ is an effective mean separation. Expressing the integrals in terms of the vibrational constant instead of I then gives

$$R_R - R_L = \left(\frac{2\hbar^2}{\mu}\right)^{\frac{1}{2}} \int_{v_{min}}^{v'} \frac{dv}{[V' - E(v,0)]^{\frac{1}{2}}} \tag{3.20}$$

$$\frac{1}{R_L} - \frac{1}{R_R} = \left(\frac{8\mu}{\hbar^2}\right)^{\frac{1}{2}} \int_{v_{min}}^{v'} \frac{B_v dv}{[V' - E(v,0)]^{\frac{1}{2}}} \tag{3.21}$$

To calculate the integrals , we need to know B as a function of v, and the energy E as a function of v. Since both E and B are treated as continuous functions, but we can only find their values for integral v, we need to fit a continuous function to the experimental data. A suitable function is a polynomial expansion

$$E(v,0) = G(v) = \sum_{i=1}^{m} p_i (v + \frac{1}{2})^i \tag{3.22}$$

$$B(v) = \sum_{j=0}^{n} q_j (v + \frac{1}{2})^j \tag{3.23}$$

The integrals can then be found numerically using, for example, *Gaussian quadrature* [45]. We have used the program "RKR.PAS" to calculate potentials from spectral data. Although we have not obtained sufficient data on the caesium triplet ground state to derive a potential using this method, we have found it very useful to derive potentials from line positions in the singlet case and for iodine and iodine bromide, since we can find wavefunctions from the potentials, and so calculate the Franck-Condon factors to predict relative intensities of the spectral lines

If the rotational structure is unresolved, then equation 3.16 can be used to find the width of the potential well, but not the absolute values of R_R and R_L. The RKR method works up to the energy of the highest observed level. Various extrapolation methods must then be used to reach the dissociation limit [43].

The RKR method only provides the potential up to the highest measured vibrational level. However, the potential close to the dissociation limit is important for determining the scattering length. A theoretical long range potential, usually of the form given in equation 3.6 is fitted to the outermost part of the RKR potential to extrapolate to the dissociation limit [13].

3.3 Calculation of scattering lengths

In chapter 1, we introduced the concept of a scattering length. In this section we will look more closely at how the scattering length is used in the study of cold collisions, and how it can be calculated from interatomic potentials, including an assessment of the approximations used in calculating cold cross sections.

3.3.1 The scattering length in Bose-Einstein condensation

In chapter 1, the applications of cold collisions were discussed. Let us now look at how the scattering length affects the stability of a condensate.

To form a Bose-Einstein condensate, it is required that the interactions do not cause the condensate to collapse. If there are effectively attractive forces between the atoms, then the density of the caesium atoms will increase and the collision rates will increase. This leads to heating and loss of atoms from the trap before a condensate can form. This line of reasoning suggests that a positive scattering length (corresponding to effectively repulsive interactions) is required for a stable condensate; however, a condensate for a negative scattering length gas has been observed [2].

The scattering length α determines both the elastic scattering cross section σ, and the energy of the condensed atoms U_0.

$$\sigma = 4\pi\alpha^2 \tag{3.24}$$

$$U_0 = h^2\alpha/2\pi m \tag{3.25}$$

If the condensate is perturbed, then density variations will occur, which can be described by a single wavefunction over the condensate

$$n(\underline{r},t) = |\Psi(\underline{r},t)|^2 \tag{3.26}$$

The perturbations can be described by a non-linear Schrödinger equation

$$i\hbar\frac{\partial\Psi}{\partial t} = -\frac{\nabla^2\Psi}{2} + U_0|\Psi|^2\Psi \tag{3.27}$$

For small k excitations, and assuming a homogeneous condensate, this leads to the dispersion relation [46]

$$\omega = \sqrt{\frac{n_0U_0}{m}}k \tag{3.28}$$

where n_0 is the density of the unperturbed condensate. Since the sign of U_0 is the same as that of α (equation 3.25), this once again suggests that only a positive scattering length will lead to a stable condensate, as a negative scattering length will lead to complex roots. This confirms that a positive scattering length is desirable for BEC. In the negative scattering length case, the number of atoms which can condense before instability occurs is restricted.

3.3.2 How can scattering be studied using interatomic potentials?

In chapter 1, we briefly mentioned that the scattering length can be calculated from interatomic potentials. In this section we will show how scattering rates can be calculated from potentials, leading to our definition of the scattering length by comparison with hard sphere scattering.

Partial wave analysis

To treat scattering quantum mechanically, we need to look at a collision between two atoms in terms of a wavefunction for one atom in the region of some scattering potential due to the other. The incident and scattered particles are described by wavefunctions, determined from the Schrödinger equation in the presence of the scattering potential, which in this case is the interatomic potential [39]. We use the method of *partial wave* analysis, in which we first obtain the energy eigenfunctions of the interatomic potential which correspond to the energy of the incident particle. Since the incoming particles have a small positive energy, the eigenfunctions of the

potential required will be those for unbound states above the dissociation limit, where the energy may take any value.

Each eigenfunction is then expressed as the sum of a plane wave representing the incident beam, and a scattered wave. We assume that a measurement can distinguish between incident and scattered particles, and that we can ignore the internal structure of the atom (i.e. we have single channel and elastic scattering).

To obtain the energy eigenfunctions of a spherically symmetric potential $U(R)$, we solve Schrödinger's equation:

$$-\frac{\hbar^2}{2m}\nabla^2\Psi(\mathbf{r}) + U(r)\Psi(\mathbf{r}) = E\Psi(\mathbf{r}) \tag{3.29}$$

to give solutions of the form

$$\Psi_l = \psi(R)Y_{lm}(\theta,\phi) \tag{3.30}$$

where $Y_{lm}(\theta,\phi)$ are spherical harmonics.

For a fixed value of the energy E, the total wavefunction is a sum of such terms over all possible values of l, the total orbital angular momentum.

$$\Psi = \sum_0^\infty C_l\psi(R)Y_{lm}(\theta,\phi) \tag{3.31}$$

Substituting equation 3.30 into equation 3.29 gives a set of *partial wave* equations [43]

$$\frac{\mathrm{d}^2}{\mathrm{dR}^2}(U(R) + \frac{2m}{\hbar^2}l(l+1))\psi_l(R) = E\psi_l(R) \tag{3.32}$$

It can be shown that so long as $RU \to 0$ as $rR \to \infty$ an approximate solution of equation 3.32 for large R is

$$\psi_l(R) \simeq \frac{\sin(kR + \delta_l(k))}{R} \tag{3.33}$$

where δ_l is the phase shift between incoming and outgoing waves. By making the substitution $\chi(R) = R\psi(R)$, we can write the wavefunction in the simpler sinusoidal form

$$\chi_l(R) = \sin(kR + \delta_l(k)) \tag{3.34}$$

A typical example of such a partial wave is shown in figure 3.2.

The next step is to express this eigenfunction as a sum of incident and scattered waves. 3.33 can be rewritten in terms of incoming and outgoing exponentials:

$$\psi_l(R) = \frac{A}{R}[e^{-ikR} - e^{i(kR-l\pi+2\delta_l)}] \tag{3.35}$$

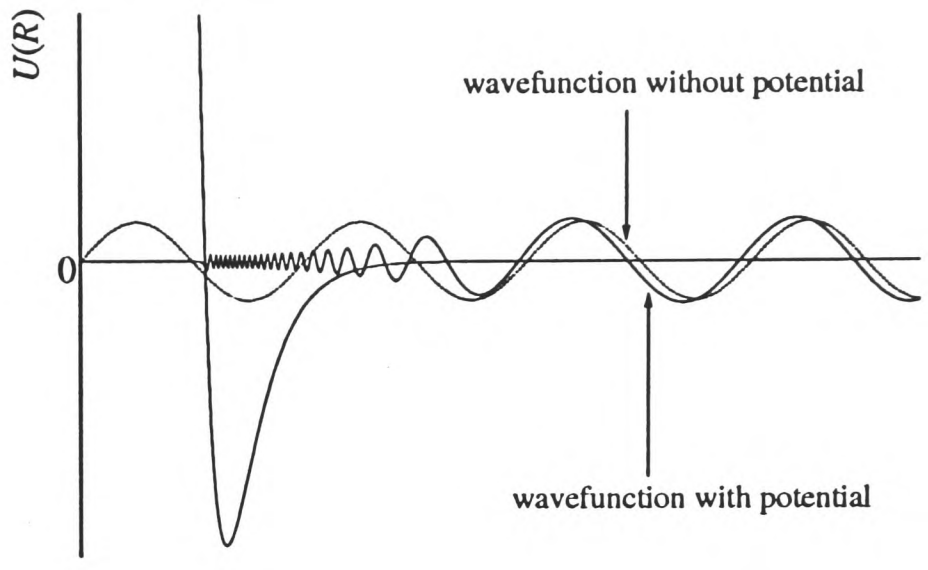

Figure 3.2: A typical partial wave, showing the phase shift introduced by the potential.

where the relationship between the phases has been chosen for convenience in the next step.

The wavefunction of the incident particle is that of a plane wave, which we can define to be along the z axis:

$$\Psi_i = Ce^{(ikR\cos\theta)} \tag{3.36}$$

In the limit of large R, this is given by

$$Ce^{(ikR\cos\theta)} = \frac{1}{2}C\sum_{l=0}^{\infty}(2l+1)i^{2l+1}\left[\frac{1}{kR}e^{-ikR} - \frac{1}{kR}e^{i(kR-l\pi)}\right]P_l(\cos\theta) \tag{3.37}$$

Compare this to the total wavefunction of the potential:

$$\Psi = \frac{A}{R}\sum_{l=0}^{\infty}[e^{-ikR} - e^{i(kR-l\pi+2\delta_l)}]\left(\frac{2l+1}{4\pi}\right)^{\frac{1}{2}}P_l(\cos\theta) \tag{3.38}$$

This wave function can be expressed as the sum of an incident wave (3.37), and a scattered wave which we wish to find. However, the scattered wave represents only particles moving *outwards* from the scatterer, and so cannot contain any terms in e^{-ikR}. Hence the coefficients of such terms must be equal for the incident wave (3.37) and the total wavefunction (3.38). Equating coefficients and subtracting the incident wavefunction from the total wavefunction then gives the scattered wavefunction

$$\Psi_s = \frac{C}{R}e^{ikR}f(\theta) \tag{3.39}$$

where

$$f(\theta) = \frac{1}{k}\sum_{l=0}^{\infty} e^{i\delta_l} \sin\delta_l P_l(\cos\theta) \tag{3.40}$$

All the information necessary to calculate the scattered wavefunction is therefore contained in the phase shifts $\delta_l(k)$.

The parameter of collisions which is generally measured experimentally is the cross section σ. The differential cross section is given by [39]

$$\sigma(\theta) = |f(\theta)|^2 \tag{3.41}$$

and the total cross section by integration over all solid angle is

$$\sigma = \frac{4\pi}{k^2}\sum_{l=0}^{\infty}(2l+1)\sin^2\delta_l \tag{3.42}$$

Although we have reduced the scattering problem to finding the phase shifts $\delta_l(k)$, we have infinitely many of them to calculate. In practice, however, the effect of each partial wave generally decreases as l increases, and so we can neglect partial waves with l higher than a certain value. We can make an estimate of how many partial waves we need to include by the following classical argument.

The partial waves correspond to atoms having an angular momentum $\sim \hbar l$. Considering a classical trajectory of an atom, in order to have an angular momentum $\hbar l$, the atom must pass the origin at a distance x such that $\hbar l = \hbar k x$, where $\hbar k$ is the linear momentum. But if x is larger than the range of the scattering potential, x_0, then there will be very little phase shift, and the effect of that partial wave will be negligibly small. So the only significant partial waves are those for which

$$kx_0 \geq l \tag{3.43}$$

S-wave scattering

If k is sufficiently small, as it is in the case of very low temperatures, then only the $l = 0$ term is important. In this approximation, we have *s-wave scattering.* For s-wave scattering, the total cross section is given by

$$\sigma = \frac{4\pi \sin^2\delta_0(k)}{k^2} \tag{3.44}$$

and the scattering is isotropic [39].

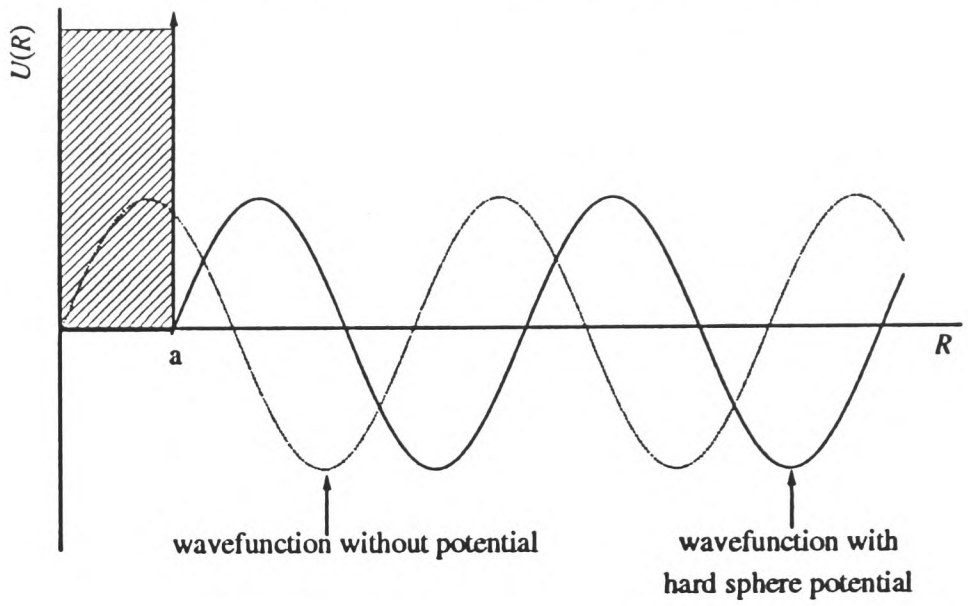

Figure 3.3: Wavefunction and phase shift for a hard sphere potential.

Hard sphere scattering

In the s-wave scattering approximation, we have reduced the problem of finding the scattering cross section to finding the phase shift $\delta_0(k)$, and hence finding the wavefunction for $l = 0$ for a given k in the presence of the scattering potential. For an arbitrary potential, the wavefunction must be calculated numerically, as described in appendix A. But first let us look at a simple case which can be solved analytically: the hard sphere potential.

In the absence of a potential, the wavefunction is given by

$$\chi(R) = \sin kR \tag{3.45}$$

If we then add in a hard sphere potential, given by

$$\begin{aligned} V &= 0, R > a \\ V &= \infty, R \leq a \end{aligned}$$

the wavefunction is excluded from the region where $V = \infty$, as shown in figure 3.3. The effect of the potential on the wavefunction is just to introduce a phase shift (figure 3.3), so that the new wavefunction is

$$\chi = \sin k(R - a) \tag{3.46}$$

The phase shift introduced by the potential is $-ka$, and so the cross section for the hard sphere potential is simply

$$\sigma = 4\pi a^2 \tag{3.47}$$

Note that for the hard sphere, the cross section is independent of the energy of the scattered particle.

Scattering from an interatomic potential

However, interatomic potentials are not those of hard spheres, but have the form discussed in section 3.1.1. A typical unbound wavefunction for such a potential is shown in figure 3.2. In contrast to the hard sphere case, the phase shift now depends on the energy, and hence wavevector, of the state. The phase shift also depends sensitively on the precise shape of the potential, as there are many fast oscillations of the wavefunction in the region of the potential well, rather than the complete exclusion of the wavefunction as in the case of the hard-sphere potential. If we wish to know the cross section for a particular energy, we now need to calculate the phase shift for that particular energy, which rather reduces the elegance of the method. However, as we are interested in the low temperature limit, we can consider only the phase shift as the energy tends to zero. If the phase shift remains small (we examine this approximation in section 3.3.3), then $\sin(\delta_0(k)) \sim \delta_0(k)$, and equation 3.44 becomes

$$\sigma = \frac{4\pi\delta_0(k)^2}{k^2} \tag{3.48}$$

We define the scattering length in terms of the phase shift as the energy tends to zero:

$$\alpha = -\lim_{k\to 0} \frac{\delta_0(k)}{k} \tag{3.49}$$

where k is the wavevector $\frac{2\pi}{\lambda}$ of the wavefunction, and δ_0 is the s-wave ($l = 0$) phase shift.

Using this definition in equation 3.48 then gives

$$\sigma = 4\pi\alpha^2 \tag{3.50}$$

Comparing this to the cross section for a hard sphere in equation 3.47, we see that the cross section for an arbitrary potential at zero energy is the same as that of a hard sphere with radius α.

In the case where the phase shifts are small, $\delta_0(k)/k$ is roughly constant for small k. Hence the cross section is given by equation 3.50 not only at $k = 0$, but also for small non-zero values of k.

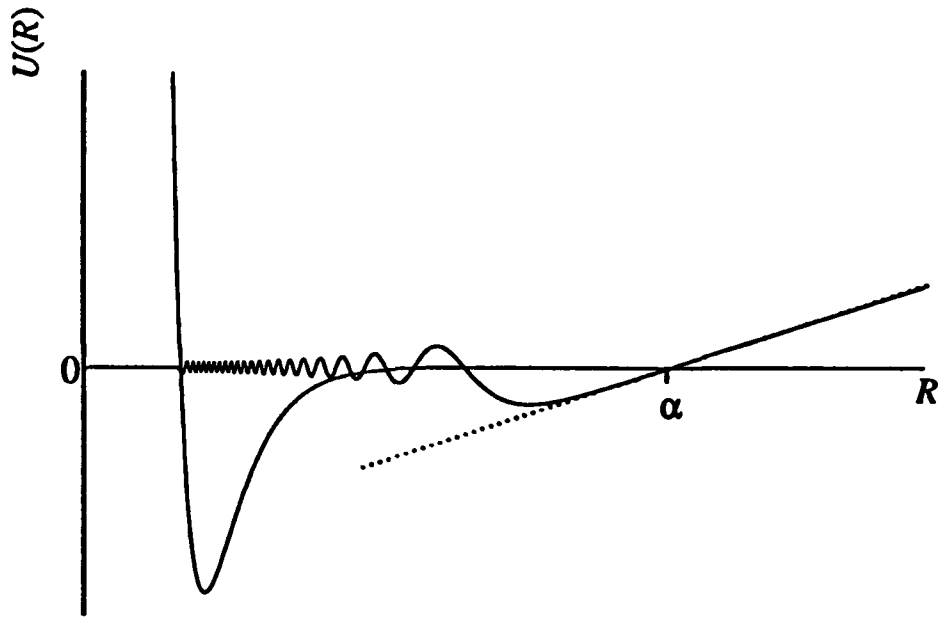

Figure 3.4: Wavefunction for low energy, showing the scattering length.

3.3.3 How does the scattering length depend on the bound states of the potential?

In the discussion of scattering lengths so far, we have considered the cross section only in terms of the phase shift at long range, and we have assumed that this phase shift is small. We must now look more closely at how the phase shift is determined by the inner part of the potential, and particularly at the significance of the bound states.

To determine the phase shift, we must find the wavefunction for a given energy by integrating Schrödinger's equation for the interatomic potential. This must in general be performed numerically, as discussed in appendix A. However, we can derive approximate results for certain cases. We have already considered the case where the phase shift is small, and found that we can use a scattering length approximation. But under certain circumstances, the phase shifts can become very large, and we must now consider the conditions for this to occur, and an alternative expression for the scattering.

There are a finite number of bound energy levels for a given interatomic potential [47], and so there is a "least bound" energy level. This least bound energy level has energy $-\epsilon$ ($\epsilon > 0$). The scattering depends critically on the position of this last bound state [48]. We can gain a qualitative idea of how the phase shift depends on the position of this least bound state by finding the wavefunctions for different positions of this least bound state, using the numerical method of appendix A. If ϵ is sufficiently large and so the last bound state is not very close to the top of the potential, then the phase shifts $\delta_0(k)$ will remain small, and we have the wavefunction shown in

figure 3.5a. If we now make a small change in the potential so that ϵ becomes larger, the least bound state moves away from the dissociation limit, and the scattering length decreases. A further change will result in a 'virtual level' approaching the dissociation limit from above. Just before this state becomes bound, the scattering length is very large and negative (figure 3.5b). As the state becomes bound, the wavefunction "turns over", as one extra bound state means one more node in the wavefunction, and the scattering length becomes large and positive (figure 3.5c).

Hence the scattering length depends very sensitively on the position of the least bound state, especially when this state is close to the dissociation limit. In the case where the least bound state is very close to the dissociation limit, or if there is a "virtual" nearly bound level (i.e., if ϵ is small), the energy of the scattered particle, E, is almost "in resonance" with the level $-\epsilon$, which leads to a significant increase in the phase shifts and cross section. In this *resonance scattering* case, equation 3.50 no longer applies [48]. The cross section in the case where there is a weakly bound level can be found by considering Schrödinger's equation for large and small R, and then considering the boundary condition that the two solutions match [48] to give

$$\sigma = \frac{2\pi\hbar}{\mu(E+\epsilon)} \tag{3.51}$$

where E is the energy of the scattered particle above the dissociation limit.

3.3.4 The effective range expansion: the best of both worlds

We now have two different expressions for the cross section, valid in opposite regimes. It is possible, however, to find an expression from equation 3.44 which is valid in both cases, by using the *effective range expansion.* The phase shift can be written as a power series expansion in k:

$$k\cot\delta_0(k) = -\frac{1}{\alpha} + \frac{1}{2}r_0k^2 + O(k^3) \tag{3.52}$$

where r_0 is the *effective range.* Substituting 3.52 into 3.44, and keeping terms up to k^2 gives [49]:

$$\sigma = \frac{4\pi\alpha^2}{k^2\alpha^2 + (1 - r_0k^2\alpha)} \tag{3.53}$$

In the limit of low energies or small $|\alpha|$ this reduces to the scattering length form of equation 3.50. This expression is also valid when there is a bound state near the

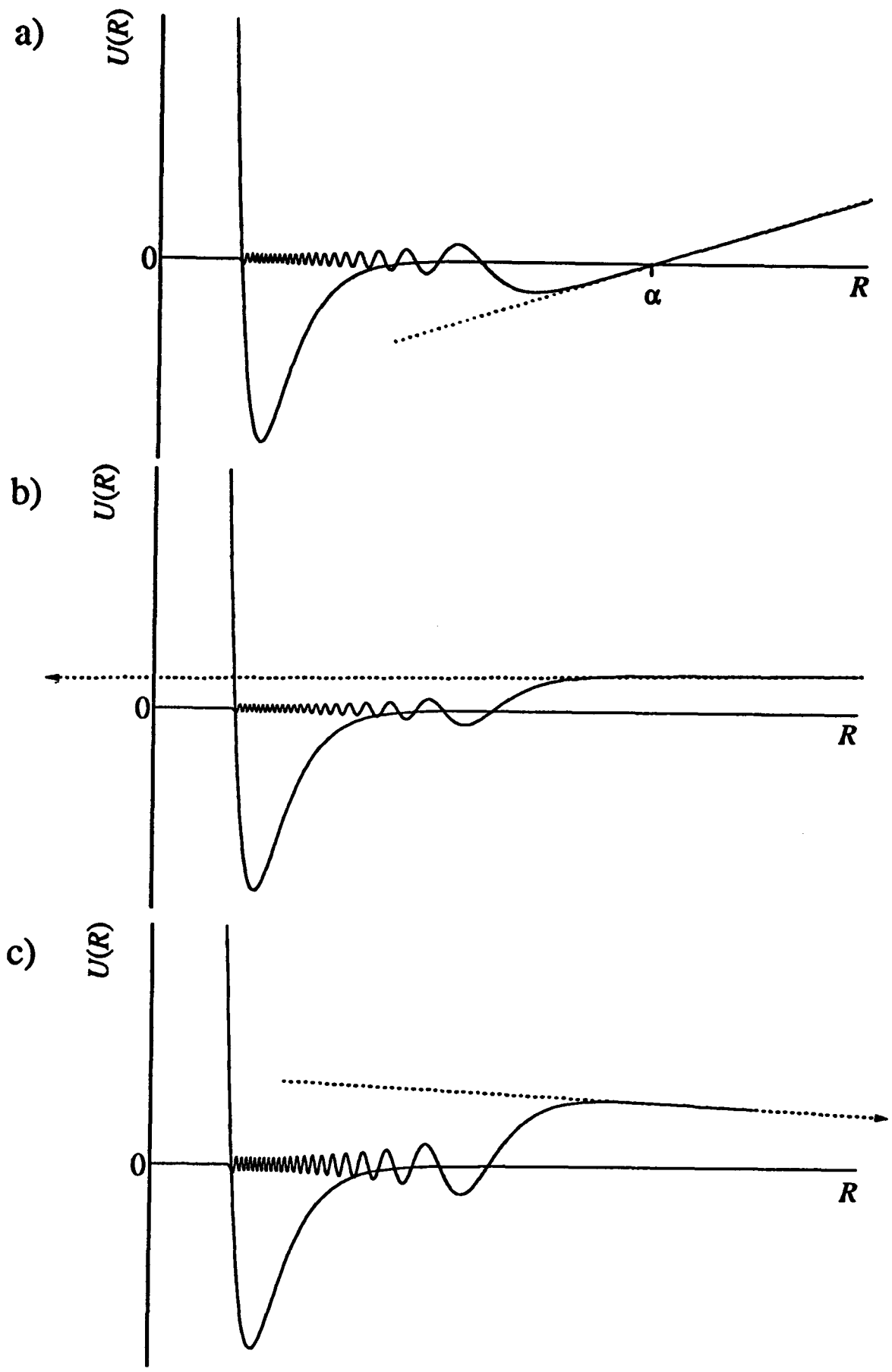

Figure 3.5: Wavefunction and scattering length for a)large positive ϵ, b)small negative ϵ, c)small positive ϵ

dissociation limit. For a bound state with energy $|E| = \frac{\hbar^2\kappa^2}{2\mu}$, α and r_0 are related by

$$-\frac{1}{\alpha} = -\kappa + \frac{1}{2}r_0\kappa^2 \tag{3.54}$$

This form for the cross section has the advantage that it is applicable across a wide range of scattering lengths.

3.4 Validity of approximate expressions for the cross section

We now have four formulae for the s-wave cross section, which are predicted to be valid in different circumstances:

a) $$\sigma = \frac{4\pi \sin^2 \delta_0(k)}{k^2} \qquad \text{(exact)} \quad (3.55)$$

which is valid for all δ_0.

b) $$\sigma = \frac{4\pi\alpha^2}{k^2\alpha^2 + (1 - r_0k^2\alpha)} \qquad \text{(effective range)} \quad (3.56)$$

which is valid for reasonably low k, all α

c) $$\sigma = 4\pi\alpha^2, \alpha = -\lim_{k\to 0}\frac{\delta_0}{k} \qquad \text{(scattering length)} \quad (3.57)$$

which is valid for small δ_0, which is the case when the least bound state ϵ is sufficiently far from the top of the potential.

d) $$\sigma = \frac{2\pi\hbar^2}{\mu(E+\epsilon)} \qquad \text{(resonance)} \quad (3.58)$$

which is valid when the least bound state is close to the top of the potential.

However, it is not immediately obvious for what values of ϵ b), c) and d) will be good approximations. The validity of each approximation may also depend on k; c) will always be true for $k = 0$ by definition, but will become an increasingly worse approximation for large k.

We have investigated the conditions under which the approximations hold by calculating the phase shifts numerically, using a potential similar to the expected form of the caesium ground state triplet potential. We calculated a Morse potential (see section 3.1.1), initially using the theoretical parameters of the caesium triplet potential found by Speiss [27]:

$$D_e = 240\text{cm}^{-1} \tag{3.59}$$

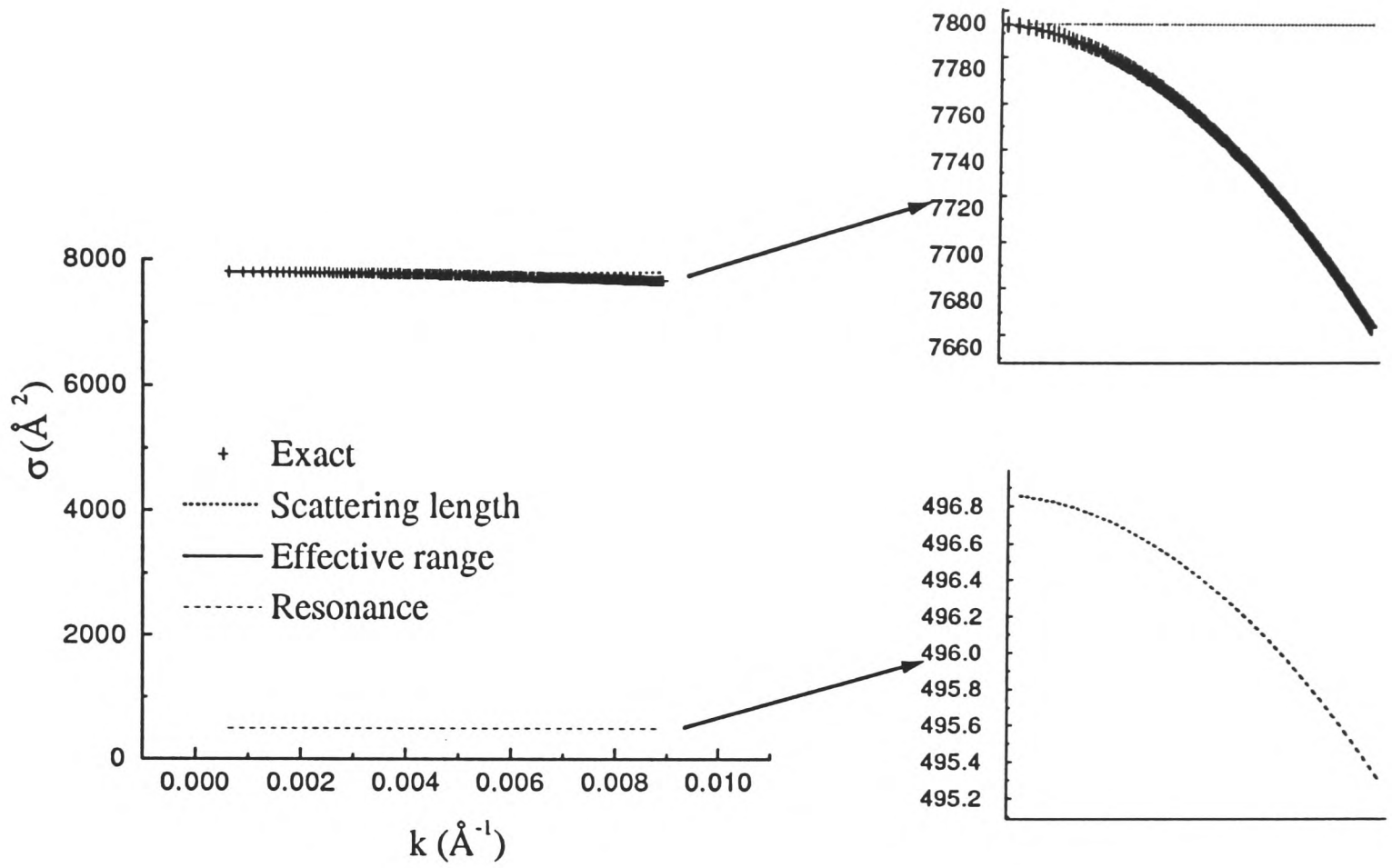

Figure 3.6: Cross section against k for different approximations.

$$\omega = 11.2\text{cm}^{-1} \tag{3.60}$$

$$B_e = 5.97 \times 10^{-3}\text{cm}^{-1} \tag{3.61}$$

which give the parameters for the Morse potential

$$\beta = 0.720\mathring{A}^{-1} \tag{3.62}$$

$$R_e = 6.496\mathring{A} \tag{3.63}$$

We calculated the potential from $R = 0.008$ to $80\mathring{A}$ at intervals of $0.008\mathring{A}$, and found values of δ_0 for particle energies from 10^{-7}cm^{-1} to $2 \times 10^{-5}\text{cm}^{-1}$ (1μK to 200μK) for this potential. On plotting δ_0 against k, for this potential, we found that the graph was a good approximation to a straight line. The scattering length is given by $\frac{-\delta_0}{k}$ as $k \to 0$. Since the gradient is almost constant, it suggests that the scattering length model is a good one in this case. To confirm this, we plotted values of σ against k as calculated from the general expression of a), and compared this with the three models b), c) and d) (figure 3.6). We found that the values of σ found in the scattering length approximation b) agree closely with the values found from a), while those calculated using the resonance approximation c) differ substantially. Hence in

this case, the scattering length model is the better. We calculated the position of the highest bound state for this potential, and found it to be at 0.0064cm^{-1} from the dissociation limit.

We then wished to look at the case when the last bound state is much closer to the top of the well. We varied the parameter β in the Morse potential, and for each value calculated the phase shift for an energy of 10^{-7}cm^{-1}. Figure 3.7 shows the phase shift, the cross section σ and $\ln\sigma$ against β. As β decreases, the last bound state moves closer to the dissociation limit, until the state is only just bound. This confirms the theory of section 3.3.3; when a state is just bound, the cross section becomes very large, and the scattering length passes from large and positive to large and negative as the potential changes so that the state is no longer bound. We then chose the value of β to be 0.70704Å^{-1}, which gives a just bound state, and again calculated the phase shifts over the same range of energies. We plotted the cross section calculated from a), and compared the result to models b), c) and d), as shown in figure 3.8. In this case, the scattering length model is much worse, and the cross sections approach those given by the resonance formula. However, the effective range formula still gives the best fit to the data.

From these calculations, we conclude that 3.50 is not a good approximation to the cross section at any but the very lowest energies when there is a state which is very weakly bound. Since recent observations by Arndt et al. [12] suggest that there is such a level for the caesium triplet ground state, we must look to a better approximation. The effective range expansion provides much better fits for the addition of only one extra parameter.

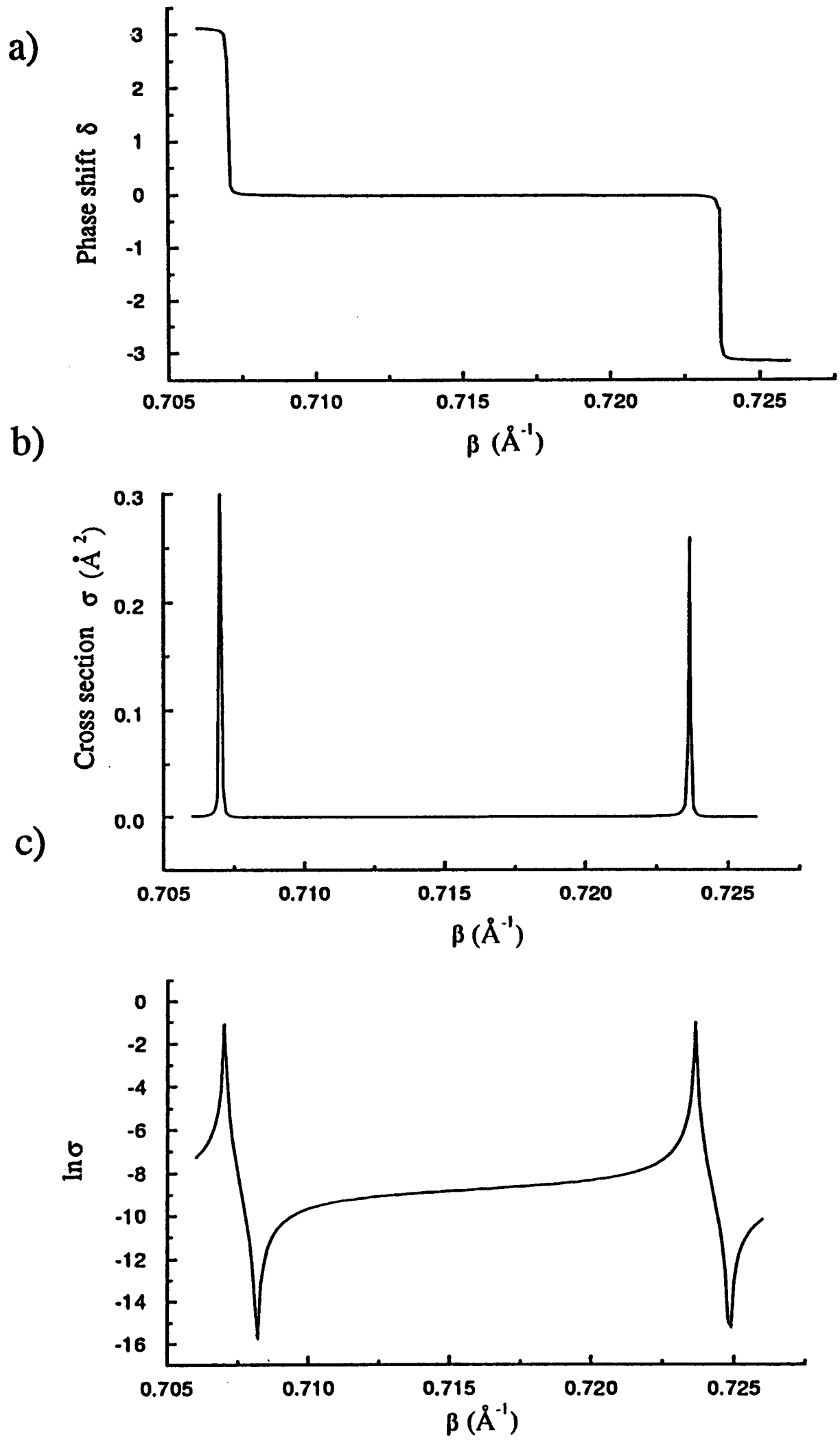

Figure 3.7: a) Phase shift, b) cross section σ, c) $\ln \sigma$ against k. Arbitrary factors of π in the phase are chosen to make the function continuous.

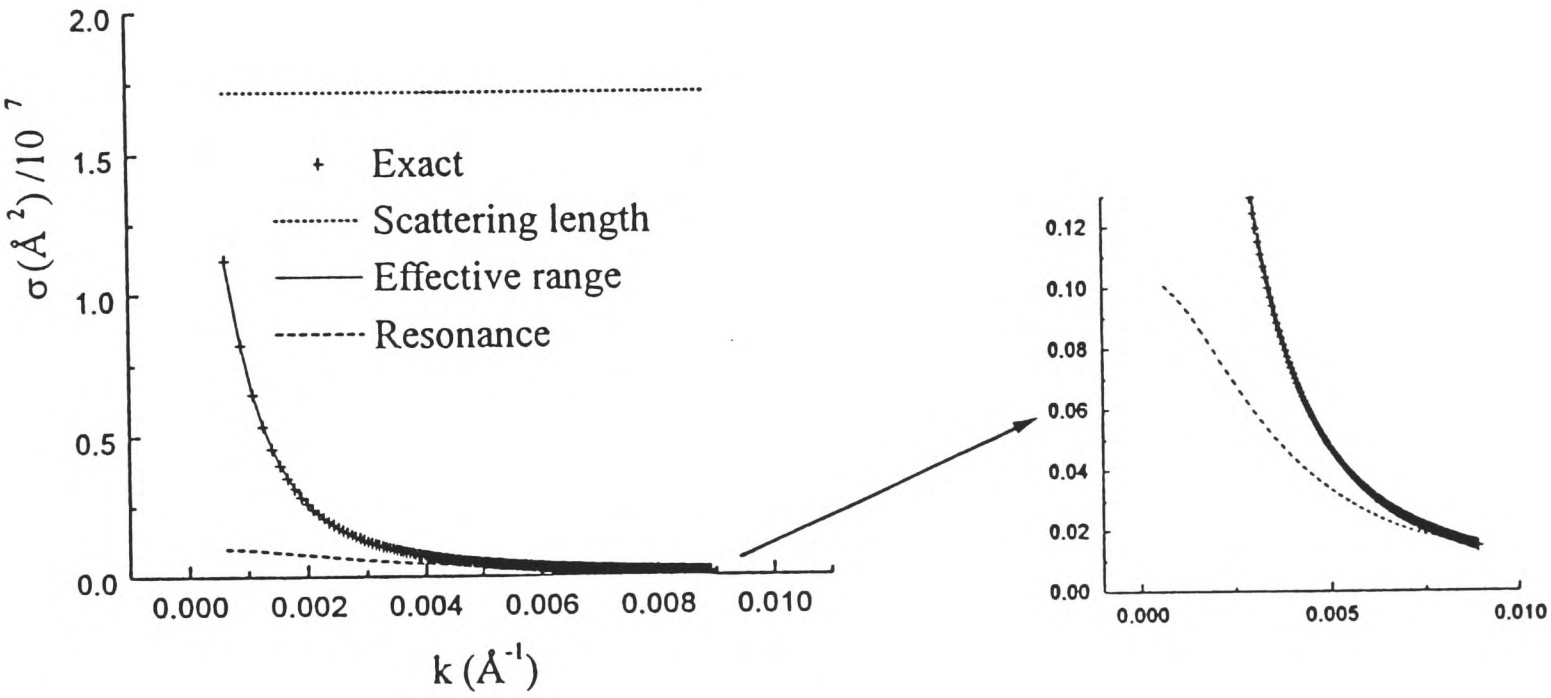

Figure 3.8: Cross section against k for different approximations, close to a bound state.

Chapter 4

Experimental details and procedure

4.1 Outline

The layout of the experiment is shown in figure 4.1. Caesium is heated to around 600K in a stainless steel oven. Argon buffer gas at a pressure of 1 to 4 atm is blown into the oven, picks up caesium vapour and the mixture is forced under pressure through a small nozzle ($\sim 250\mu$m diameter) at the base of the oven, into a vacuum of around 0.15 Torr. The mixture undergoes a supersonic free jet expansion, and the caesium is cooled. Under these conditions, caesium dimers are formed at a rotational temperature of $\sim$ 10K. The caesium dimers are probed with light from a tunable cw ring dye laser, intersecting the molecular beam at right-angles, at a distance of 5 to 10mm downstream of the nozzle. We tune the laser over the frequencies of interest, and detect the total fluorescence (i.e. not spectrally resolved) in a direction close to perpendicular to both the laser and the molecular beam. The fluorescence passes through a series of lenses and slits to narrow the Doppler width and increase the resolution, and is detected by a Peltier-cooled photomultiplier. A filter is sometimes used to prevent infra-red photons from the hot oven from reaching the photomultiplier.

We are interested in two wavelength regions: around 765nm for singlet spectra, and 710nm for triplet spectra. As the laser is scanned with time (typically 20GHz in 180s) we take measurements from the photomultiplier, and from the various calibration systems. Hence the time axis of a plot of the results is effectively a frequency axis, though slightly non-linear. Fringes from a temperature-stabilised etalon enable the

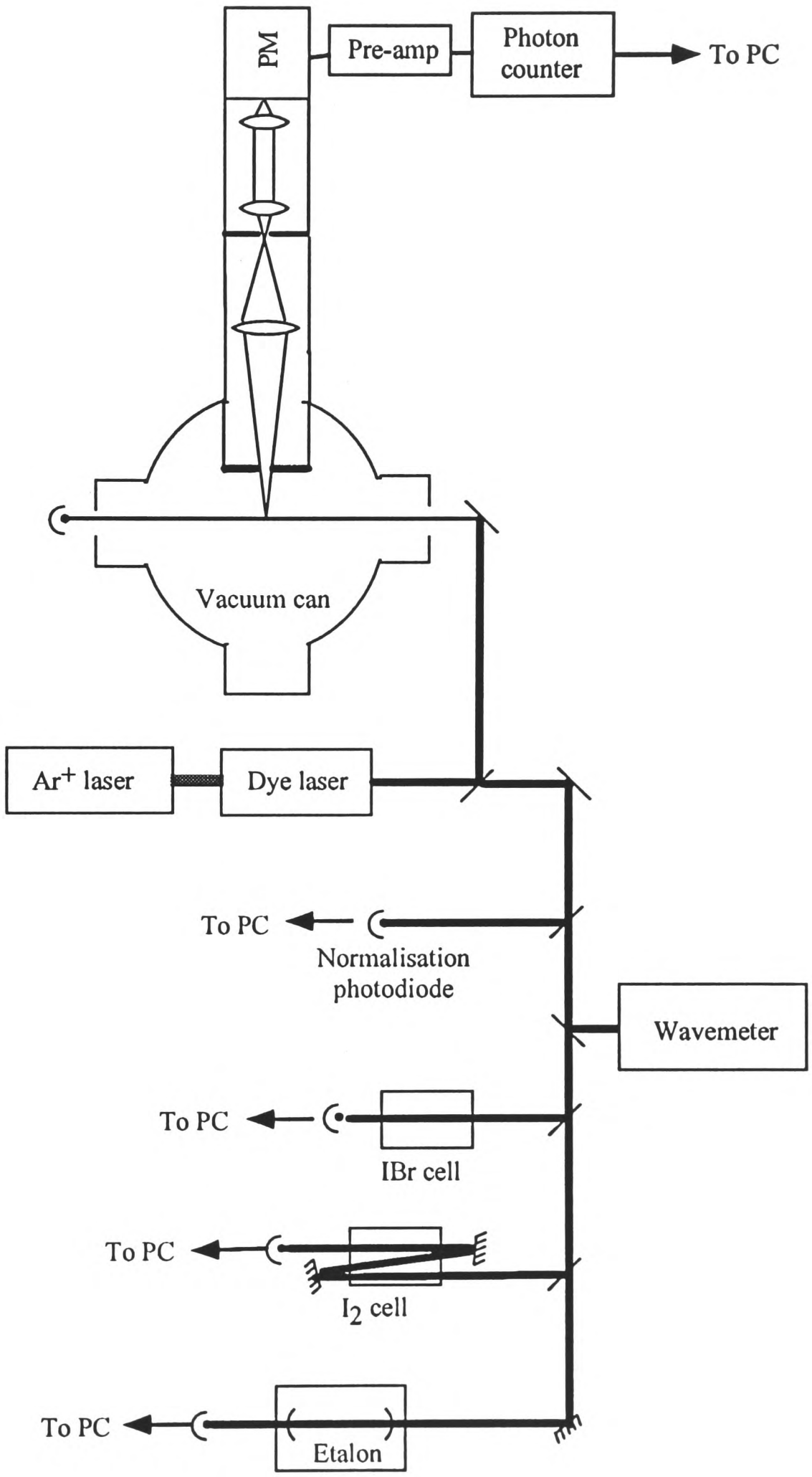

Figure 4.1: Schematic layout of experiment

scans to be linearized, and a relative frequency scale assigned. A Burleigh Wavemeter gives an absolute read-out, but is accurate only to around 0.1cm^{-1}. To give a more accurate calibration, we take an iodine absorption spectrum and an iodine bromide absorption spectrum simultaneously with our caesium dimer spectrum. The positions of the iodine lines are accurately known [50], and provide an absolute frequency reference. The iodine bromide spectrum provides additional features to enable consecutive scans to be overlapped.

The output from the photomultiplier is recorded by a photon counter after passing through a pre-amplifier. The output from the counter is recorded by a PC. At the same time, data from the photodiodes collecting light from the calibration is recorded by the PC using an analogue to digital converter.

4.2 Laser system

The laser used is a Coherent 699-21 tunable cw dye laser, with Pyridine-2 dye, pumped by the 514nm line of a Coherent Innova 100 argon-ion laser. The power of the pump laser is typically 8W, from which an output power from the dye laser of 250mW was achieved at 710nm, and 150mW at765 nm. The argon-ion laser was typically run with its internal aperture set at 12 to ensure a good mode quality.

The dye laser is run single mode, and is aligned and operated in the standard way [51]: the laser is locked to a reference cavity, and is scanned by maintaining this lock while the reference cavity is scanned by changing its path length with a galvo-driven Brewster plate. We found that the power and stability of the dye laser was improved when the dye was cooled to around 12°C using a modified beer cooler.

4.2.1 Ti:Sapphire laser

In our earlier experiments we tried using a Microlase E110 titanium-doped sapphire (Ti:Sapphire) laser. It is preferable to use a solid state lasing medium instead of a liquid dye as dye requires changing every few months (a messy procedure) and many laser dyes are toxic and/or carcinogenic. However, it proved difficult to lock and scan the Ti:Sapphire laser, especially at 710nm; this wavelength is at the extreme end of the Ti:Sapphire's tuning range.

4.2.2 Atmospheric oxygen absorption

We found that there were certain wavelengths around 765nm to which it was impossible to tune either the dye laser or the Ti:Sapphire laser. The problem appeared likely to be due to atmospheric O_2, which absorbs strongly around 765nm. We confirmed this by finding some of the frequencies at which the laser would not run, and comparing these with the frequencies of oxygen bands given by Babcock and Herzberg [52], as shown in table 4.1. The frequencies at which there was no lasing agree well with

Observed regions where no lasing (cm^{-1})	O_2 band (cm^{-1}) [52]
13067.92-13068.07	13068.068
13069.80-13069.96	13069.947
13076.16-13076.36	13076.312
13078.05-13078.22	13078.214
13084.02-13084.23	13084.193

Table 4.1: Comparison of observed laser jumps with known oxygen absorption bands.

the frequencies of the oxygen bands.

We attempted to solve the problem by sealing the case of the laser, and purging the laser cavity with oxygen-free nitrogen. We tried this with both the Ti:Sapphire and the dye laser, but we still found the oxygen absorption occurring. This was probably because it was very difficult to make the laser case at all gas-tight, and it only requires a very small absorption to force the laser to run on a different mode. As a result, there were some singlet vibrational bands which it was not possible to observe, as they corresponded to a region of oxygen absorption.

4.3 The molecular beam

In order for caesium dimers to be formed, a caesium vapour needs to be cooled so that the dimers are not dissociated by thermal energy. This is achieved in our experiment in a supersonic free jet expansion. As the caesium expands into a vacuum, it cools, and molecules are stabilized. This forms a cold molecular beam, which is probed by the laser beam a few millimetres from the nozzle, in the interaction region.

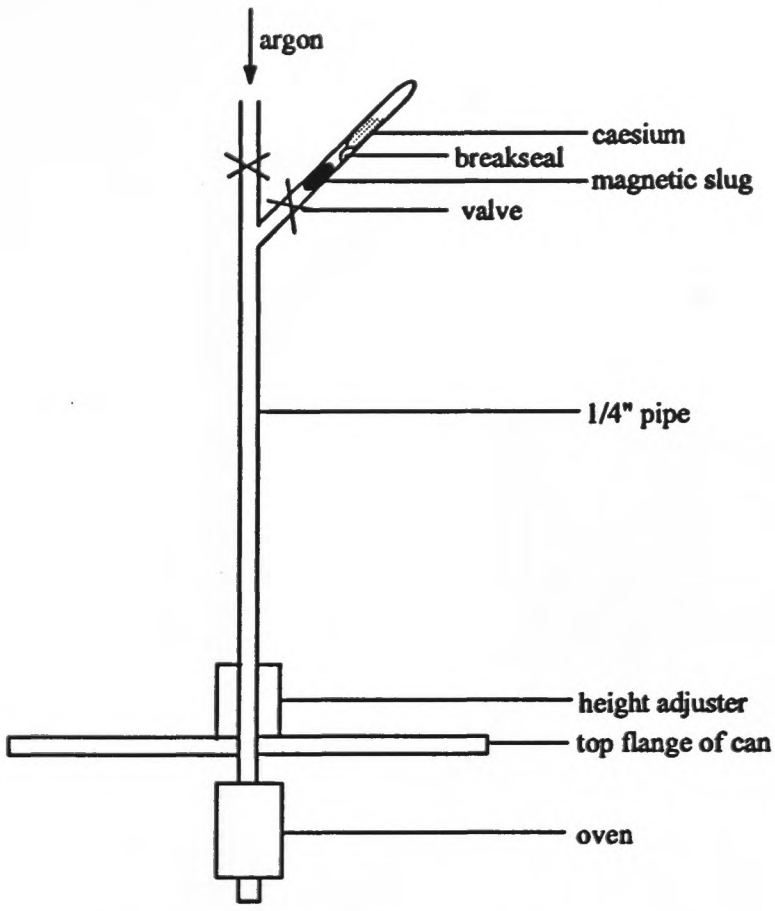

Figure 4.2: The sidearm method of loading the caesium

4.3.1 The oven and nozzle

One of the most difficult aspects of the experiment has been developing a suitable oven and loading technique. Caesium is highly reactive, reacting explosively with water, and oxidising rapidly and possibly violently in air. It is necessary to handle caesium only in a vacuum or an inert gas atmosphere.

Development of the oven and loading technique

The oven that was initially used was the same as that used in the previous work in the laboratory on mercury-argon bands [45]. The oven was constructed from a Nupro inline filter. This contains a stainless steel sintered pot, which we used as a reservoir for the caesium, held in place against the top of the filter by a spring. To load the system, a sidearm was attached to the argon line, with a valve so that the sidearm could be sealed (figure 4.2). The system was evacuated, and then a magnet was used to drive the slug against the breakseal in an attempt to break it. This is a standard technique for releasing materials under vacuum. However, we found that the breakseal did not break, so we modified the technique. We inserted a heavier slug, pumped out the sidearm, closed the valve, and removed the sidearm below the valve. The ampoule was then shaken, and we found that the slug did then break the

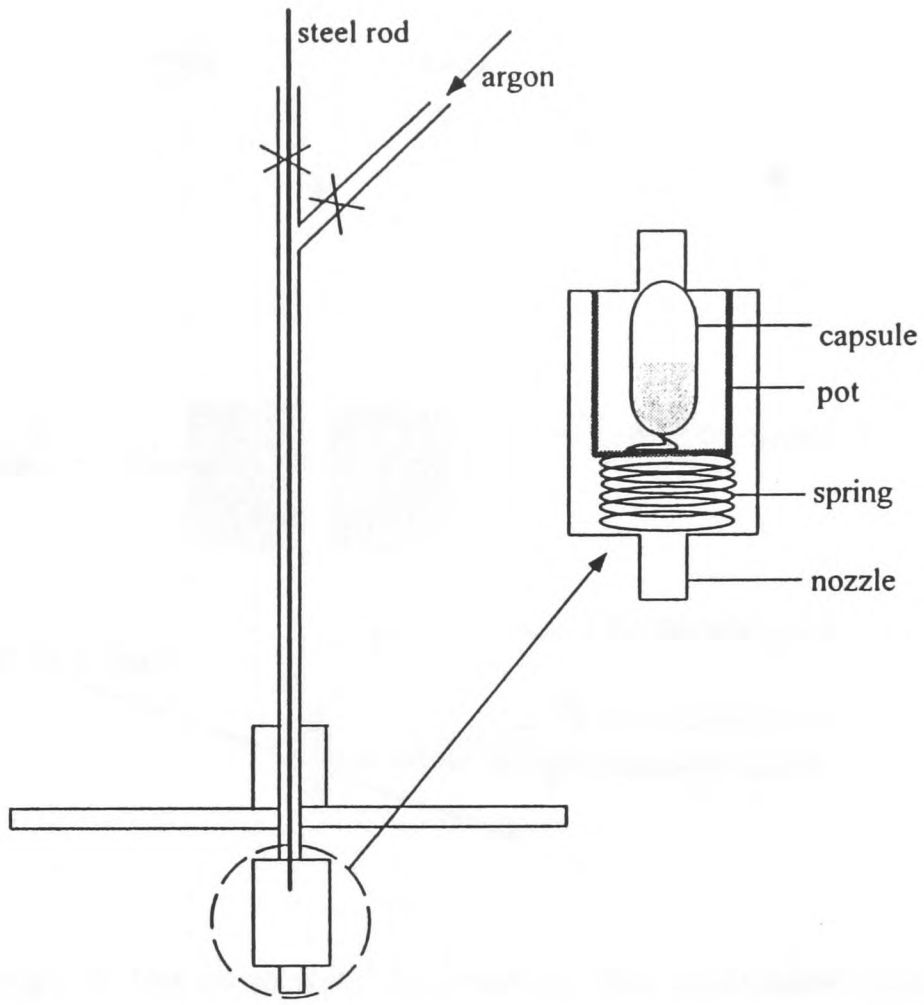

Figure 4.3: The capsule method of loading the caesium

seal. The sidearm was reattached, and the vacuum system pumped down.

The intention was to transfer the caesium into the oven by distilling it across. We heated both the caesium ampoule and the connecting pipes to at least 60°C with a hot air gun. We started the argon flow, and opened the valve to the sidearm. We found that only small quantities of caesium passed through the broken seal, and we could not get any caesium past the first valve.

In the next development, we distilled caesium into small glass capsules with break-seals, which were designed to fit inside the oven, as shown in figure 4.3. We moved the argon feed to the sidearm, leaving a straight metal tube running vertically upwards from the oven. We assembled the oven and sealed the vacuum can with the glass capsule in the oven, and then flushed the vacuum can with argon. We then opened the top valve, ensuring that there was an overpressure of argon. We lowered a steel rod down the pipe and into the oven, and used it to break open the caesium capsule. We withdrew the rod, closed the valve, started the vacuum pumps and switched on the oven heater.

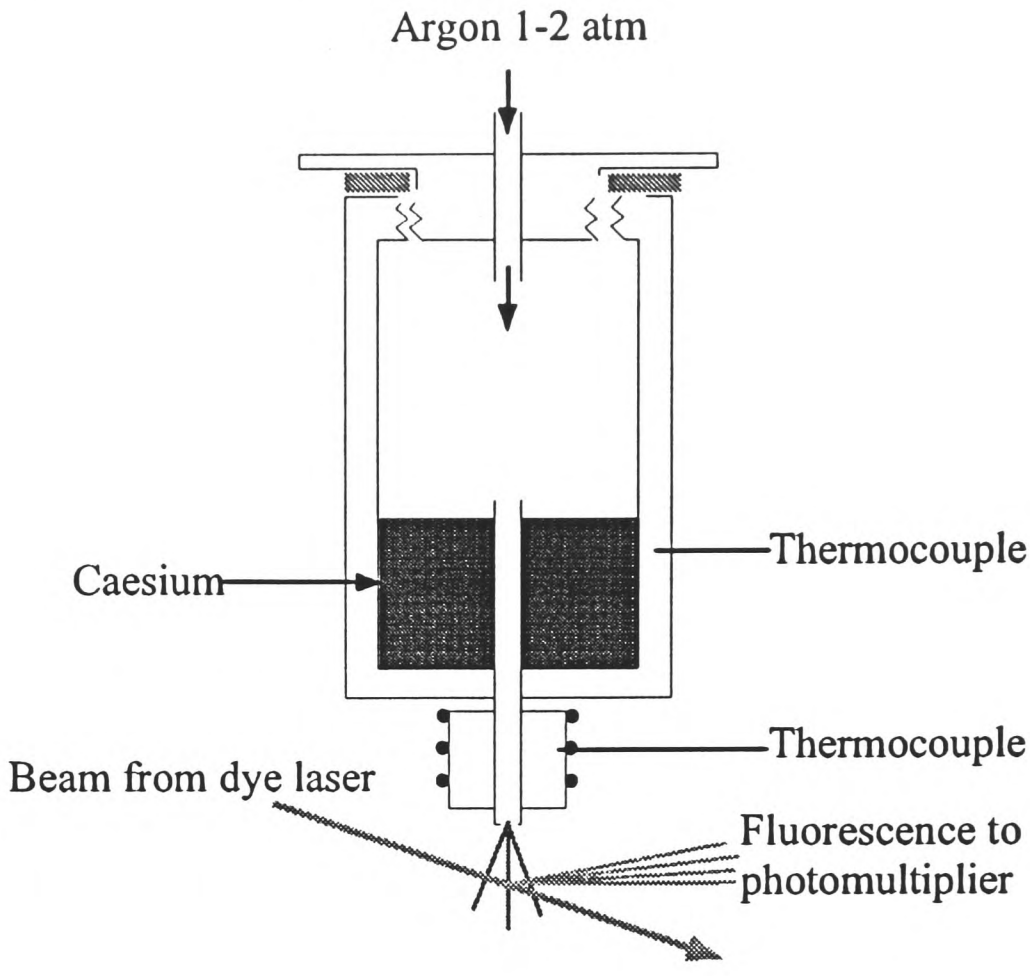

Figure 4.4: The final design of the oven used to produce the molecules in a free jet.

Using this technique, we were able to see some signals which may have been due to caesium molecules. However, very little caesium (< 0.2g) could be loaded in this way, and so it ran out very quickly. A fair proportion of the caesium became trapped in the sintered pot and in the fragments of glass. We also found that the nozzle blocked frequently because there was nothing to stop any impurities from falling into the nozzle. We realised that we needed a larger oven and more caesium, and so we constructed a new oven and a glovebox for the loading; this proved successful, and was our final design.

The final design and loading technique

A diagram of the oven used to produce the molecular beam is shown in figure 4.4. The oven is made from stainless steel, which does not react with caesium. The sections of the oven are screwed together with copper washers between sections to ensure a tight seal. The nozzle section is heated using a Thermocoax 25cm heater, coiled around the oven and soldered in place. The body of the oven is heated solely by conduction of heat from the nozzle section. This ensures that the nozzle is hotter than the rest

of the oven, so that caesium does not condense in the nozzle. The heater wires are connected via ceramic connector blocks to a connector sealed through the top flange. Thermocouple wires were placed in contact with the nozzle and the main oven body.

The nozzle protrudes ~3cm inside the oven so that only vapour, not liquid caesium, can reach the nozzle. This is to prevent the nozzle from blocking. Nevertheless, the nozzle does block occasionally during a run. When this happens, an attempt is made to clear the nozzle by increasing the temperature of the oven and/or the pressure of the buffer gas. This sometimes works, but often there is no remedy. The oven must be allowed to cool, and is then dismantled and thoroughly cleaned. After each experimental run, we cleaned the oven and nozzle in detergent, water and acetone (as a drying agent). Severe tarnishing was removed by cleaning in an acid bath.

Caesium is loaded into the oven in a home-made glove box. The oven and a sealed 1g caesium ampoule are placed inside the glove box, and the top flange of the vacuum can is placed on top of the glovebox to seal it, with the argon feed pipe passing through the flange into the glove box. The glove box is then filled with argon (BOC Pureshield). The ampoule is then opened and the caesium heated to around 60°C by placing the opened ampoule into a hot copper block. At this temperature the caesium becomes liquid and is then poured into the oven, care being taken to avoid placing caesium inside the nozzle. The oven is then attached to the argon feed pipe of the flange, and the nozzle sealed with plastic held in place by a rubber band.

The flange is then put in place on the top of the vacuum can, with an O-ring to seal it, and adjusted by eye to centre the oven relative to the laser beam and the collection optics. The nozzle cover is removed and the argon flow started at a pressure of about 1 atm. The vacuum can is then sealed, and is pumped down as described in section 4.4. We use BOC research grade argon which is specified to have very low impurity levels. Using the less pure "Pureshield" argon led to frequent nozzle blocking.

The pressure of the argon is controlled by a secondary regulator to reduce fluctuations in the flow rate which occur when using the primary regulator on the gas bottle.

A MKS Baratron 122A pressure gauge is attached to the vacuum can and a pressure gauge used in the argon line. We typically have an argon pressure of 1.4 atm, a pressure inside the vacuum can of 0.165 Torr, an oven temperature of 300°C and a nozzle temperature of 450°C. These values have been chosen on the basis of

previous experiments on Cs_2 [28, 26], and the previous experiment in our laboratory on mercury-argon [45]. A drop in can pressure to below 0.1 Torr indicates that the nozzle is blocking.

Nozzle diameter

We initially used nozzles with diameter ~100 and 150μm. These nozzles frequently blocked, probably due to caesium compounds such as caesium oxide and caesium hydroxide. We found that blocking was much less frequent with a $\sim$ 250μm diameter nozzle. Although this was not the sole reason for using a larger nozzle (see section 4.9.4), it was a major factor.

4.3.2 Supersonic expansion

The supersonic expansion we are using is known as a *free jet* expansion. A source can be described as a jet if the mean free path, λ, of the atoms is much smaller than the diameter, d of the aperture through which the atoms flow [53]. A previous calculation [54] gives that λ is 0.3μm for a pressure of 2 atm of argon. Since we use a nozzle diameter of 250μm diameter, the jet condition is satisfied.

The form of the emerging jet is as shown in figure 4.5 [53]. Total enthalpy is conserved in the expansion; the total enthalpy is made up of the random thermal enthalpy of the gas, and that due to directed flow i.e. its velocity. The expansion leads to an increase in the flow velocity of the gas, and hence to a decrease in translational temperature.

Just after the nozzle, large numbers of collisions take place, and molecules are formed. As the gas expands, collisions become less frequent. Three-body collisions, which are required for molecules to form, become rare, and molecular formation stops. However, two-body collisions continue further into the expansion. Since vibrational and rotational relaxation require only two-body collisions, the vibrational and rotational temperatures continue to decrease, until there are very few collisions, and the temperatures become "frozen-in". Rotational motion reaches equilibrium more quickly than vibrational motion, and so the rotational temperature is the lower. In previous studies, Kim and Yoshihara [26] estimate their vibrational and rotational temperatures to be 5K and 1K respectively, while Diemer et al.[28] find temperatures of 55K and 10K.

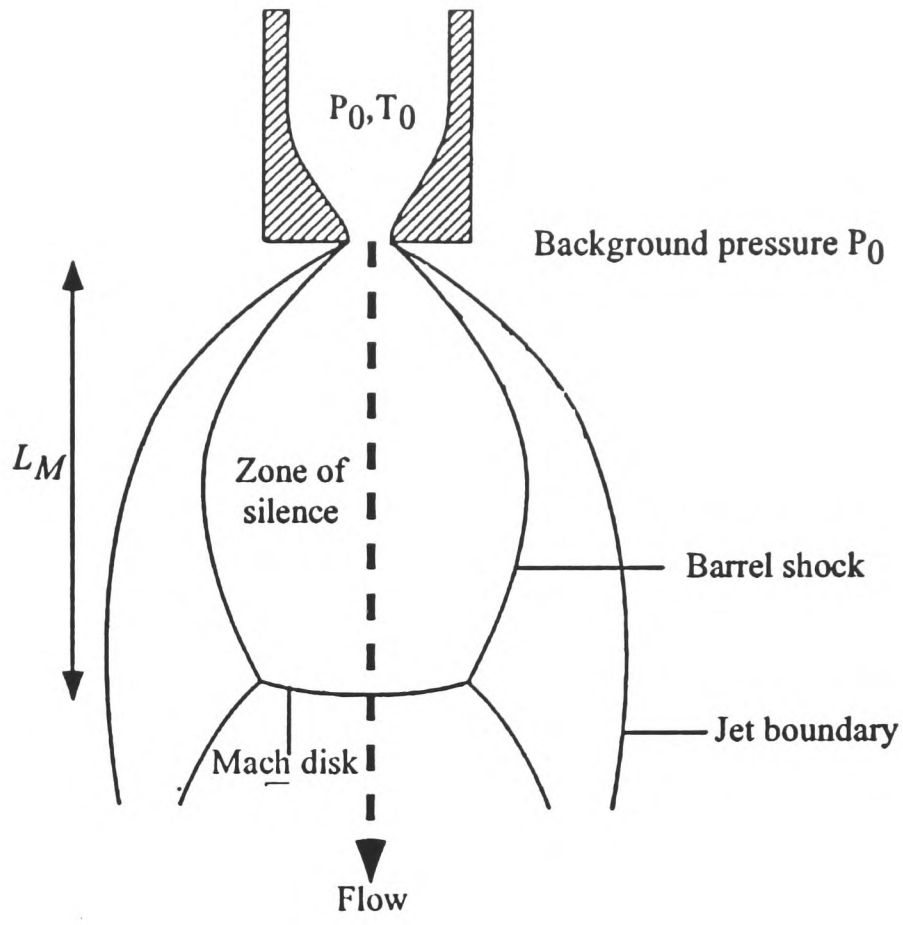

Figure 4.5: Free-jet expansion

The collision-free region is the *zone of silence* (see figure 4.5), and it is in this region that we would prefer to probe the molecules. Further downstream, the background gas becomes significant, and a shock wave, the *Mach disk* forms. The distance of the Mach disk from the nozzle is given by [53]

$$\frac{L_M}{d} = 0.67 \left(\frac{P_0}{P_b}\right)^{1/2} \tag{4.1}$$

where P_0 is the buffer gas pressure, P_b is the background pressure in the chamber and d is the diameter of the nozzle. For P_0=1.2 atm (900 Torr), P_b=0.15 Torr and $d = 0.25$mm, L_M ~13mm. We set the nozzle to be 5 to 12mm above the beam, and so we conclude that we were always probing the molecules within the zone of silence, as desired. The experimental observation that the signal to noise ratio decreased markedly when probing more than 12mm from the nozzle provides confirmation of this.

4.4 The expansion chamber and vacuum system

The oven is sealed inside a vacuum can, shown in figure 4.6. Flanges are mounted

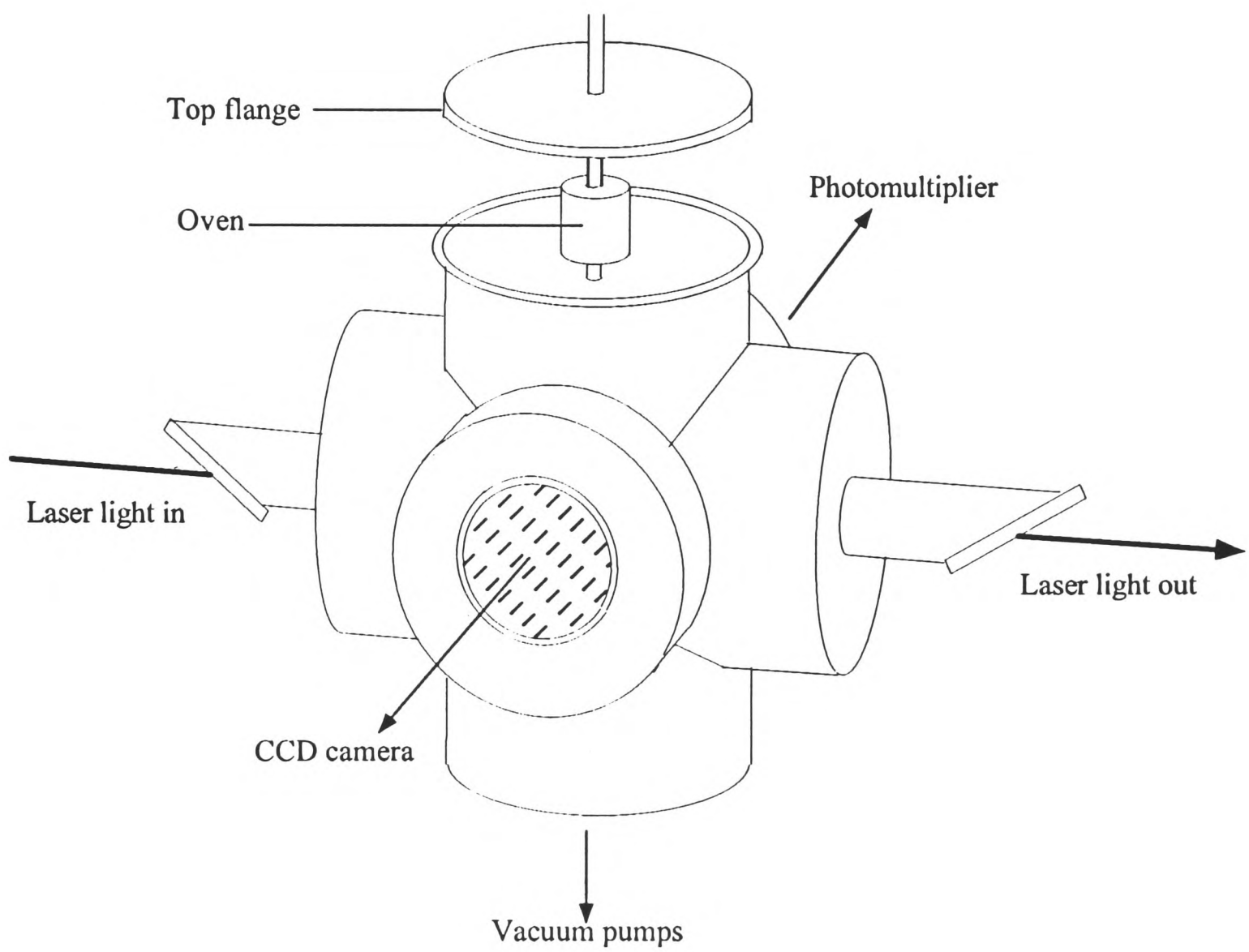

Figure 4.6: The vacuum can (many details omitted)

on five of the six sides, with the pumps below. The flanges to the left and right have Brewster windows mounted on them, and baffles inside to reduce the scattered light reaching the photomultiplier from the laser beam. The collection optics and photomultiplier are mounted at the rear of the can, while the front flange has an anti-reflection coated window, through which the interaction region can be imaged using a CCD camera. The top flange has the mounting and argon feed for the oven, as well as feed-throughs for the power to the oven heaters, and the mount for the pressure gauge. The vacuum can is supported on a table, while the pumps rest on the floor. The vacuum can is joined to the pumps by a flexible bellows coupling. Two pumps are used to evacuate the can. The first is a two-stage rotary pump (Edwards E2M80), which pumps from atmospheric pressure to around 0.2 Torr (with no argon flowing). However, this pump is not capable of handling large quantities of gas, and with argon flowing, only a pressure of around 1.5 Torr is achieved.

In addition to the rotary pump, a mechanical booster pump ('Roots' pump, Edwards EH1200) is used to reach lower pressures. This type of pump is good at pumping large quantities of gas, and so is ideal in this case, where we have a flow of argon into the system. The Roots pump is water cooled. It should not be used when the can is at atmospheric pressure, but is switched on when the rotary pump has reduced the pressure below around 2 Torr. We avoid using the heaters in air, as the combination of oxygen and heat could lead to corrosion, and reduce the life of the heaters.

We have taken steps to reduce the corrosion by caesium of the rotary pump. We use a nitrogen purge at a pressure of 3 psi on the pump, so that the gases from the vacuum system come into contact with nitrogen, rather than air. We have also fitted an external oil filter (Edwards EOF300) to the rotary pump, to filter corrosive caesium compounds from the pump oil. The exhaust from the pumps is piped outside the building.

4.4.1 Reduction of vibration

The vacuum pumps produce considerable amounts of noise and vibration. We found that the vibration was transferred to the vacuum can, and produced noise on the measured signals. Our initial approach to reducing the vibration was to attempt to isolate the can and pump assembly from the rest of the experiment, so that neither the table supporting the optics nor the photomultiplier were in physical contact with

vacuum can. We later found that a different approach was better. We put cross-braces on the table holding the vacuum can to provide extra rigidity, and bolted the bread-board on which the input optics were mounted rigidly to both the main steel table and the vacuum can table. We added steel rods to bolt the photomultiplier firmly to the vacuum can. We then used neoprene rubber and cork to isolate the vacuum can from its support. By making the system more rigid instead of isolating it, we greatly reduced the amount of vibration transmitted to the vacuum can; despite our initial fears, very little vibration was transmitted. The later technique also had the advantage that the vacuum can did not sink downwards when it was pumped out; with the initial approach, the can sunk by a few millimetres (and not by a reproducible distance), when the pumps were on, making the optical alignment difficult.

4.5 Diode Laser and CCD camera

One of the problems we encountered early in the experiment was that, in the absence of molecular signal, we had no way of telling how much, if any, caesium was present in the beam. To solve this problem, we have added a diode laser to the experiment, which can be tuned to 852nm, the wavelength of the $6^2P_{\frac{3}{2}} \rightarrow 6^2S_{\frac{1}{2}}$ Cs atomic resonance line. This laser is directed into the can along the same path as the beam from the dye laser by a sliding mirror.

The diode laser is grating stabilized, with a maximum output power of 100mW at 852nm. Tuning is achieved by controlling the temperature and current of the diode, and the angle of the grating. We use a temperature control unit which cools the diode using a Peltier cooler, and measures the temperature using a thermocouple. A stable current control box is used to avoid current spikes which could damage the laser. A constant dc voltage of between 0 and 80V is applied to the grating to tune it, with a small modulation of 1V p-p superimposed. In this way the laser can be tuned to the caesium atomic line, and scanned continuously over it.

A small fraction of the beam from the diode laser is picked off with a beamsplitter, and directed through a room temperature caesium cell, onto a photodiode connected to an oscilloscope. This is used to tune the laser to the correct frequency.

When the diode laser is tuned to the atomic line, we can view the fluorescence from the caesium beam directly using a CCD camera. A typical view of the caesium beam is shown in figure 4.7. The CCD camera can also be used to observe the caesium beam

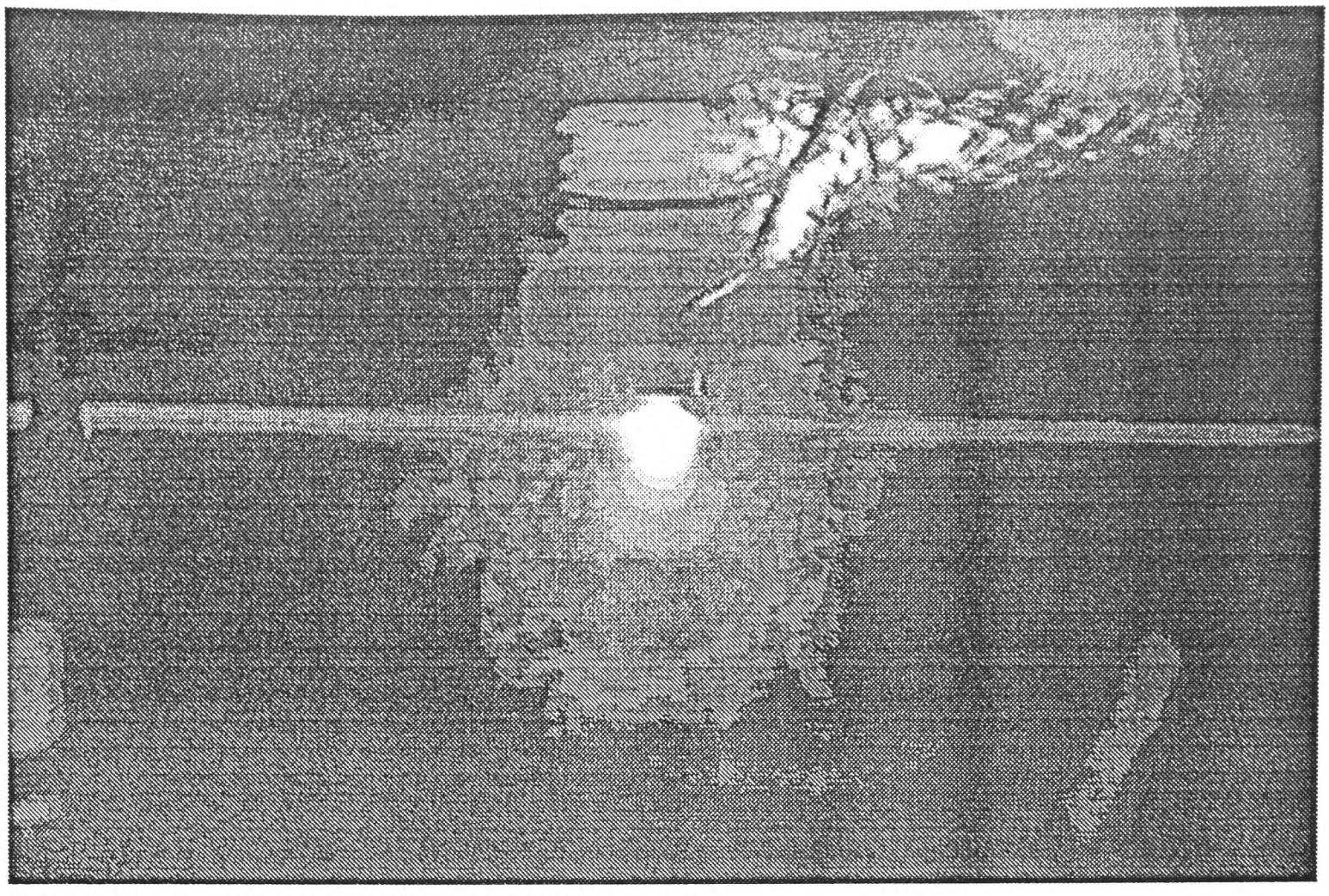

Figure 4.7: CCD camera image of caesium beam illuminated by diode laser light.

when the dye laser is tuned to a molecular transition. As the laser is tuned, different velocity classes of molecules are Doppler-shifted into resonance, and a bright line is seen to sweep across the beam. This provides a useful check that a peak observed by the photomultiplier is due to molecular absorption, and also provides a good method of locating molecular features, as the flash on the monitor is easy to see by eye even when the laser is scanned over an absorption very quickly.

4.6 Optics and imaging

We expect the signals from triplet molecules to be very small, and so it is important to optimise the signal-to-noise ratio. An important aspect of reducing noise is a good optical system, to cut out scattered and background light. We use input optics, to give a clean incoming beam, and output optics to ensure that the outgoing beam can leave the can without scattering back towards the PM. We have carefully designed collection optics, to reduce the scattering observed from surfaces in the can. We also use a filter in front of the PM window, to block out infra-red photons from the hot oven when studying the weak triplet signals.

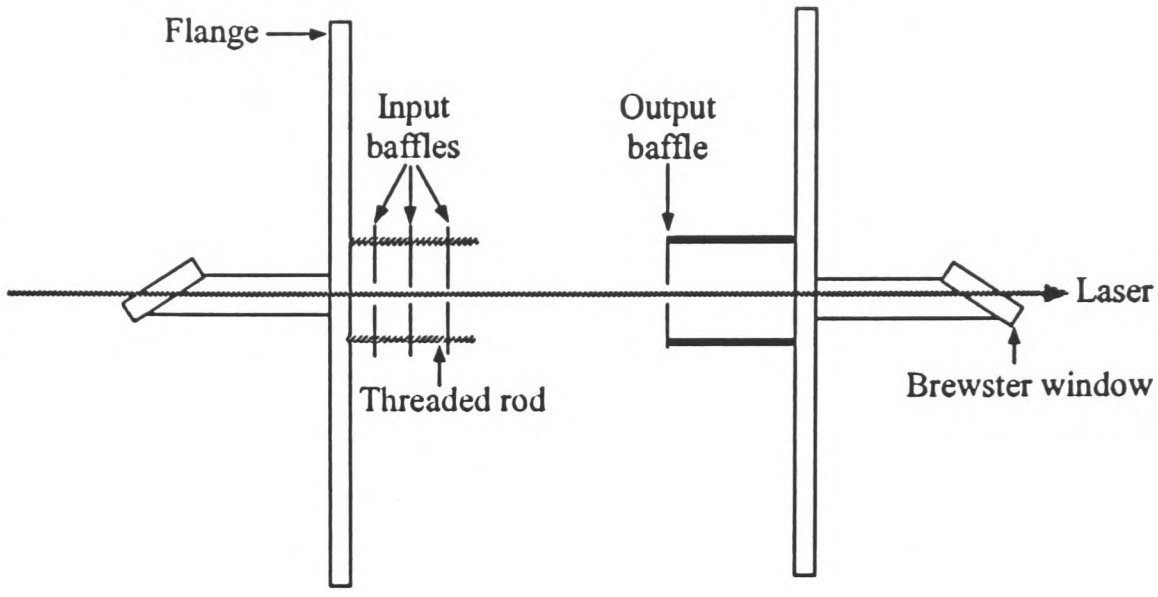

Figure 4.8: Path of laser beam through can; oven not shown.

Input optics

The path of the laser beam through the vacuum can is shown in figure 4.8. A lens (f ~150mm) is used to focus the laser so that the waist (~ 1.5mm) occurs at the interaction region, below the nozzle. The beam passes through Brewster angled windows with a 60' wedge. We initially used parallel-faced windows, but found that the windows gave multiple reflections with interference effects as the laser was scanned, leading to fluctuations in intensity. The use of Brewster angles maximizes the laser power entering the can, and minimizes reflection back into the can on exit.

The inside of the can is painted black with aquadag, a water-based paint, consisting of a suspension of graphite particles. This gives a very matt surface, which absorbs most light falling onto it. It is suitable for use in vacuum systems as the water quickly evaporates, leaving no solvent residue.

To reduce scattering further, a series of baffles are used inside the can, on the input side. These are a set of thin discs with holes in their centres, mounted on rods so that the holes are accurately aligned. The idea is that any scattered light around the beam is blocked by the first baffle. However, this leads to some scattering from the edges of the baffle, so the second baffle, with a slightly larger hole, blocks scattering from the first baffle. Similarly, the third baffle blocks any residual scattering from the second. The beam is focused to a waist at the interaction region, with a diameter of around 1.5mm. As the sizes of the holes are 2, 3, and 4mm, the main beam can pass through the baffles if correctly aligned.

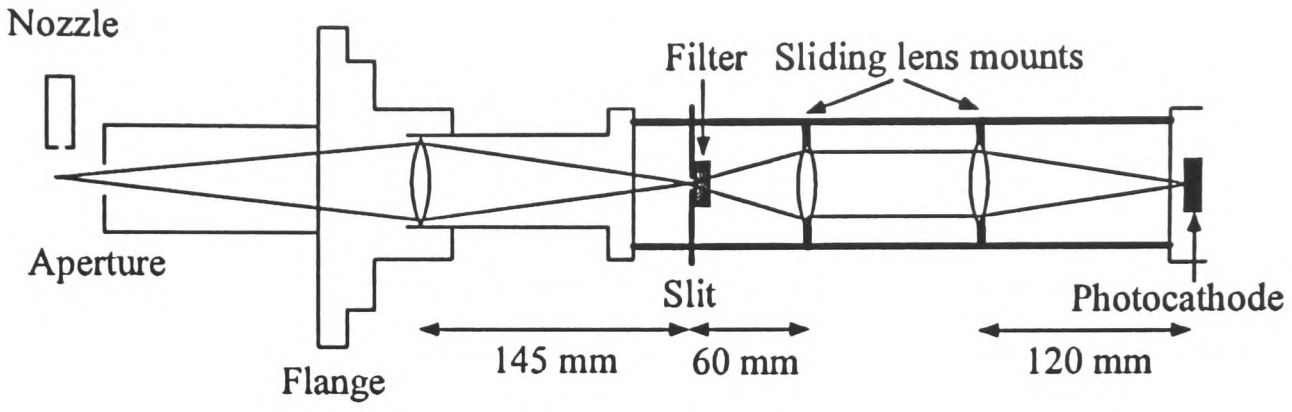

Figure 4.9: Collection optics used to image interaction region onto photomultiplier

On the exit side, the beam passes through a single baffle, and out through the Brewster window, where it is blocked by a Wood's horn. This is a piece of glass tubing, closed at one end, and drawn into a curve. The outside is painted black to absorb the light. When we used a photodiode on the output, especially if a neutral density filter was used in front of it, the background was much worse due to reflections back into the can. We also experimented with using more than one baffle on the exit side, but since any scatter from the laser beam as it encounters the exit baffles is back towards the interaction region, the scatter was actually worse. We also tried using additional irises to clean up the laser beam before it entered the vacuum can. They did not reduce scattered light significantly, although we found them helpful for aligning the laser beam through the vacuum can.

4.6.1 Collection optics

The collection optics used to collect the fluorescence from the interaction region are shown in figure 4.9. They are designed so that the maximum light from the interaction region is imaged onto the photocathode (which is only 10mm by 4mm in size) of the photomultiplier, while the minimum amount of scattered light reaches the photomultiplier. This can be achieved by using large aperture lenses to collect as much light as possible, while using suitable slits to block out the scatter.

Lens system

Our initial collection optics consisted of only the single fixed lens closest to the interaction region. This was a very inflexible arrangement, as focusing could only be

achieved by moving the whole photomultiplier assembly. We added in the two sliding lenses shown in the diagram, enabling us to fix the distance between the flange and the photomultiplier. They are mounted on rails which act as an optical bench. The sliding slit is moved along the rails to the image of the interaction region formed by the first lens. The sliding lenses are moved along the rails to focus the light from the sliding slit onto the photocathode. To aid with adjustment of the lenses and slits, a scattering metal edge is attached to the oven in place of the nozzle to give scattered laser light from the interaction region.

We found that the first fixed lens we used produced significant aberration; when we illuminated the sliding slit, and looked at its image in the interaction region, we found that the image moved as we looked through different parts of the lens. The movement was of the order of 1mm, the width of the slit, so the aberration was clearly limiting the resolution (see below). We substituted a higher quality lens, and the aberration was visibly reduced. This made it feasible to reduce the slit width to increase the resolution.

Slit widths and resolution

An aperture and a slit are used to block scattered light and to reduce the effective Doppler width. The aperture, of width 9.5mm and height 5mm, is mounted on a baffle inside the can and is positioned 25mm behind the interaction region. These dimensions were chosen so that scattering from the nozzle, at a height of 5mm above the laser beam, would not reach the PM. The slit, located in the image plane of the first lens, has a height of 3.2mm, chosen so that scatter from the edges of the first slit will be blocked. The width of this slit is much less - we have used slits from 0.5mm to 2mm wide. This is so that only light from a chosen part of the interaction region reaches the photomultiplier. This means that fluorescence is only detected from molecules which are moving almost in a single direction, and so the Doppler width is reduced and the resolution increased.

In the case of the singlet spectra, the signals were sufficiently strong that we were able to use for our final results a slit as narrow as 0.5mm, giving a considerable reduction in Doppler width. As the triplet spectra give much weaker signals, we added a horizontal micrometer adjustment to the position of the slit. The slit can be adjusted without room light reaching the PM. There is a red LED in front of the narrow slit, which can be used to illuminate the slit so that an image of its edges

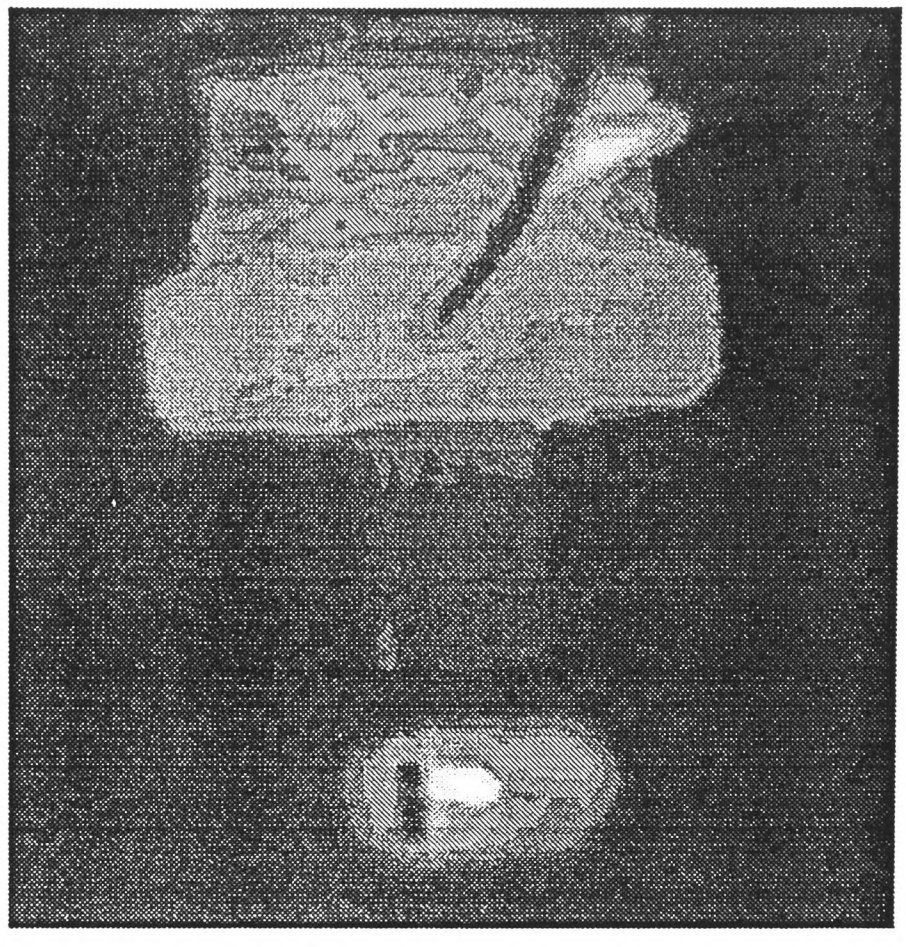

Figure 4.10: CCD camera image showing the illuminated slit

can be seen with the CCD camera. This enables us to determine where the slit is in relation to the interaction region (figure 4.10). We expected that the best signals would be obtained when the slit was in line with the centre of the interaction region. But although this gives us maximum background counts, we do not see good signals from molecules. We found that it was better to place the image of the slit away from the centre of the interaction region. In this case far fewer counts were detected but a much better signal to background ratio was obtained (section 4.9.1).

Because the oven is heated, it gives off infra-red photons, which are picked up by the photomultiplier. When looking for triplet spectra at 710nm, we use a filter (mounted immediately behind the second slit) to cut off photons with a wavelength longer than 750nm. The filter is not used when observing singlet spectra at 765nm. The imaging geometry is such that very little oven light reaches the photomultiplier.

Once the alignment was completed, we covered over the gap between the flange and the PM with a length of plastic drainpipe, split so that the upper half could be lifted off. The edges were sealed with black tape, to make the system light-tight. In addition, we wrapped thick black cloth around the pipe to further block light.

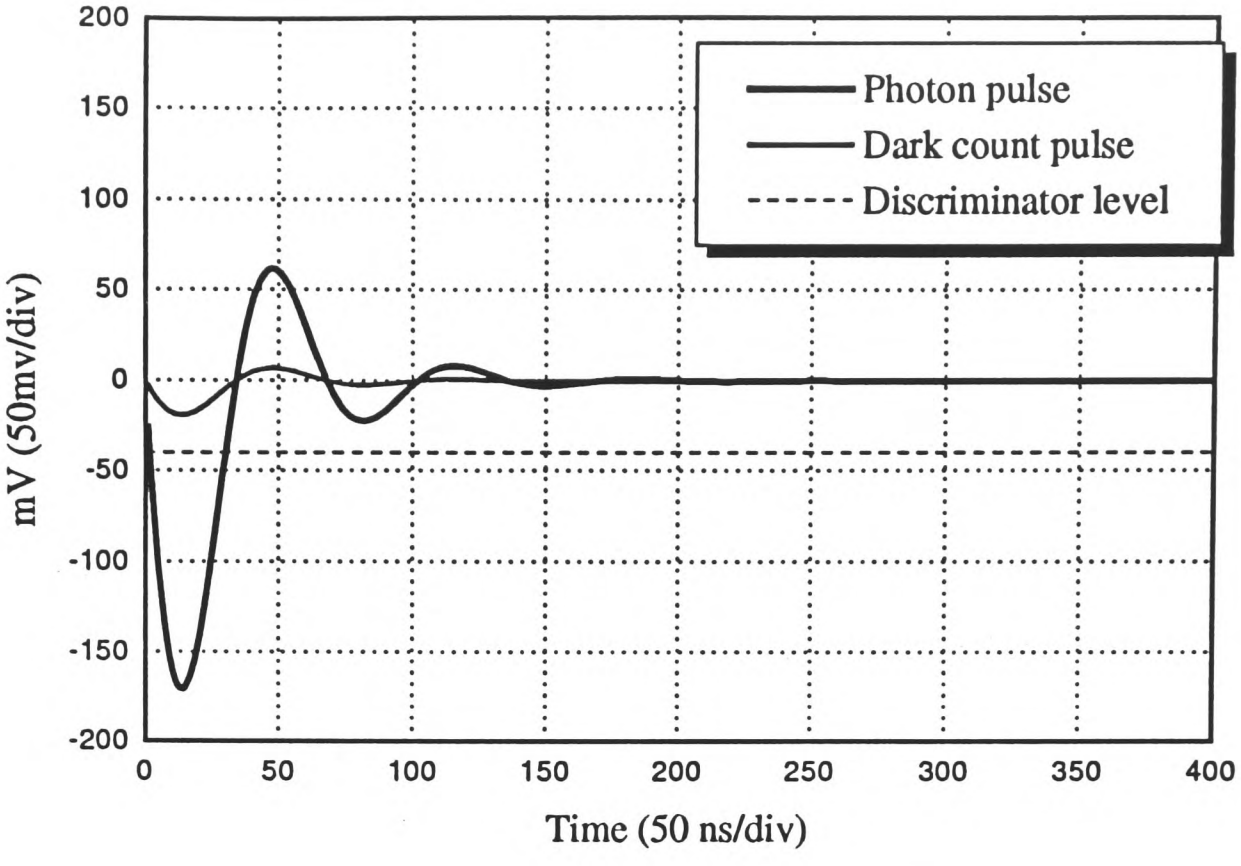

Figure 4.11: Pulse from photomultiplier

4.6.2 Photomultiplier

The photomultiplier is an 11 stage Burle C31034 with a spectral response range of 185 to 930nm, run at a voltage of 2kV. In this experiment, we use the photomultiplier in photon counting mode. Each photon detected by the photomultiplier produces a current pulse. The pulses are amplified by a preamplifier, and pass to the photon counter (figure 4.11).

The photon counter is a Stanford Research Systems model SR400. This counts the number of pulses, by counting when the input voltage passes through a certain discriminator level. The shape of the pulses as they reach the photon counter is shown in figure 4.11. The discriminator level is set to be above the level of the ringing, but below the height of the photon pulses. The ringing can be reduced by the use of a snubber. This is a short piece (~25cm) of 50Ω coax cable, terminated with a 50Ω variable resistor. The snubber is attached to the anode of the PMT along with the output lead. The resistance of the snubber potentiometer is adjusted to give the best output pulse shape. We also reduced ringing by terminating the lead from the preamplifier where it is attached to the photon counter with a 50Ω resistance attached using a T-piece. The discriminator level also needs to be set to minimize the number of dark counts recorded. Dark counts occur when electrons are

thermally emitted inside the photomultiplier, without the passage of a photon. The pulses due to dark counts are generally smaller than those due to photons, so the number counted can be reduced by setting the discriminator level below the pulses due to dark counts. By looking at the pulses on the 'scope, a discriminator level of -40mV was chosen. The level of thermal emission, and hence number of dark counts, is reduced by cooling the photomultiplier using a Peltier cooler, which reduces the temperature of the photomultiplier tube to around -10°C.

The dark count from the photomultiplier is typically 200 counts per half second.

Although the various levels of the photon counter can be set using menus and buttons on the front panel, we control it from the computer, through the serial port, using the commands given in the photon counter manual. This is described in further detail in section 4.8.

4.7 Calibration

In order to measure the frequencies of the molecular spectra accurately, we use several different calibration techniques. Our absolute frequency standard is the iodine spectrum, using the line positions tabulated in [50]. In addition, we have a computer program, based on the same data, which fits profiles of the iodine lines to our experimental lines. Since the iodine lines are widely spaced (on average one per 20GHz scan), we also use an absorption spectrum of IBr, and an etalon, which give more information over a 20GHz scan.

4.7.1 Etalon

To provide suitable reference fringes to assign a frequency scale on individual scans, we use a confocal etalon. The etalon has plates separated by ~7.5cm, with the mirrors coated for the red. The etalon is mounted in a temperature stabilized housing, which can be pumped out to give extra stability. The free spectral range of the etalon was previously measured to be 1.9782(4) GHz in vacuo [55]. As we used the etalon without a vacuum pumping system, there will be a small difference in the free spectral range due to the refractive index of air, which is 1.000275 at the wavelengths used. However, this will only introduce a relative error of 17MHz over a $2cm^{-1}$ band, which is negligible compared with other errors.

If the confocal etalon is aligned so that the light does not pass through the very

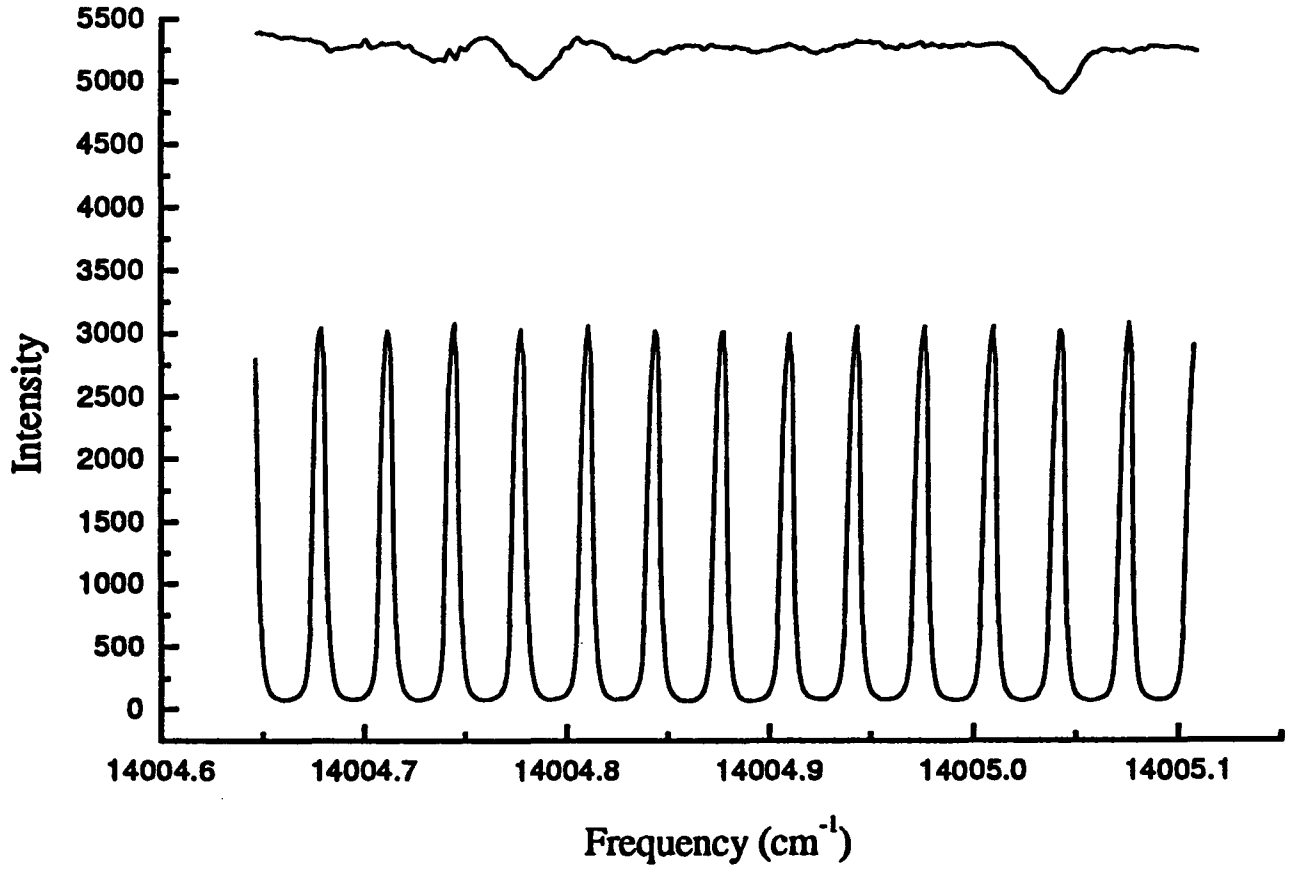

Figure 4.12: Iodine bromide spectrum and etalon fringes.

centre of the plates, twice as many fringes are observed, and the apparent free spectral range is halved. In this arrangement, the absolute frequency positions of the fringes will not be consistent, and the system is more prone to drifting with beam displacement. We sometimes operated the etalon in this way, although the alignment was always close to the ideal confocal alignment.

The etalon fringes allow the scan to be linearized and the frequency scale to be calibrated by means of a spline fitting program on the PC.

4.7.2 IBr

Although the spacing of the etalon fringes is known very well, each etalon fringe is identical. Another method is required to be able to patch consecutive scans together, with more distinctive features. For this, we use an iodine bromide absorption spectrum.

The iodine bromide is contained in a glass cell of 25mm diameter and 30cm in length. Part of the laser beam is picked off with a beam splitter. After passing through the cell, the beam falls on a photodiode. Figure 4.12 shows a typical IBr spectrum.

We compared our iodine bromide line positions with those of Selin [56] and those

of Appadoo et al.[57], but we were not able to identify corresponding lines.

Using these spectra, it is straightforward to identify equivalent etalon fringes on consecutive scans, enabling them to be joined and ensuring that the whole of frequency space is covered.

4.7.3 Wavemeter

To provide a fast and convenient measure of the laser frequency while tuning the laser, we use a Burleigh WA-10 wavemeter. This is very simple to use, and requires no internal alignment or electronic adjustment. Part of the laser beam is picked off with a beam splitter, and directed into the entrance aperture of the wavemeter. A He-Ne tracer beam is emitted from the aperture, and the input beam is correctly aligned when it travels the same path as the He-Ne (but in the opposite direction).

The Burleigh wavemeter gives a direct digital readout, in either wavenumbers or nanometers, which is updated every 1.6s. The wavemeter reads to 0.01cm^{-1}, but comparison with the iodine spectrum suggests that systematic calibration errors make it only reliable to $\sim 0.1\text{cm}^{-1}$. The wavemeter is very convenient for tuning the laser, but is not sufficiently accurate to rely on as a sole method of calibration.

4.7.4 Optogalvanic spectroscopy of neon

Before we were able to achieve a successful calibration with iodine, we tried using lines of neon as our absolute calibration, at 14215.97cm^{-1} and 13935.49cm^{-1}. To observe these lines, we used the technique of optogalvanic spectroscopy. When a discharge lamp is irradiated with photons with a frequency corresponding to a transition in the atoms of the discharge, there may be a change in the voltage across the discharge tube [58]. This method is especially useful in neon and the other noble gases, where it is simple to make a discharge lamp in such a way that external light can be directed onto the discharge. Figure 4.13 shows how the Phillips neon spectral lamp is connected to the high voltage supply. The supply is a Farnell Instruments DC supply, and we used a voltage of 235V. The laser light is directed through a chopper wheel, and onto the central part of the discharge. We found that the strongest signals were obtained when the beam was not focused.

We scanned the laser over the region of the atomic line. When the frequency corresponded to that of the line, an oscillation at the frequency of the chopper was

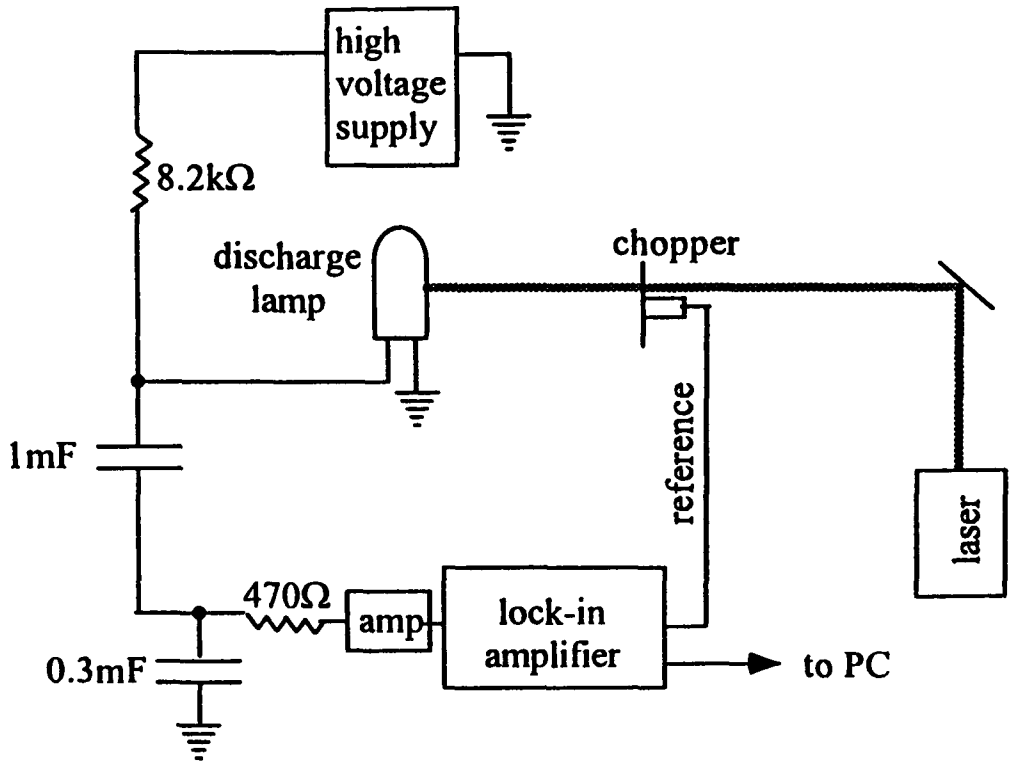

Figure 4.13: Apparatus used for opto-galvanic spectroscopy

observed using a 'scope. We then passed the signal from the amplifier through a lock-in detector, using a signal from the chopper wheel control box as the reference signal. We generally used a time constant of 0.1s for the lock-in detector. The output of the lock-in detector was connected to the analogue/digital converter, and was recorded by the PC. A typical line profile is shown in figure 4.14.

The two lines were measured as being at 13935.5nm and 14215.9nm using the Burleigh wavemeter. Unfortunately, we found it necessary to use the wavemeter in its low resolution mode because we were using the Ti:Sapphire laser for these readings, which gave an output with large intensity fluctuations; the wavemeter can only read to 1 decimal place when there are such fluctuations.

We had initially hoped to construct the spectrum over the whole region between these two neon lines, using the iodine bromide spectrum and etalon fringes to join scans and provide a relative frequency scale. We then intended to use the neon calibration to assign an absolute frequency scale. However, it soon became apparent that this would take a very long time, and that it would be better to study only a range of a few wavenumbers over each vibrational band. Once we had been able to observe iodine spectra and match the line positions with those of [50], the optogalvanic spectroscopy became unnecessary.

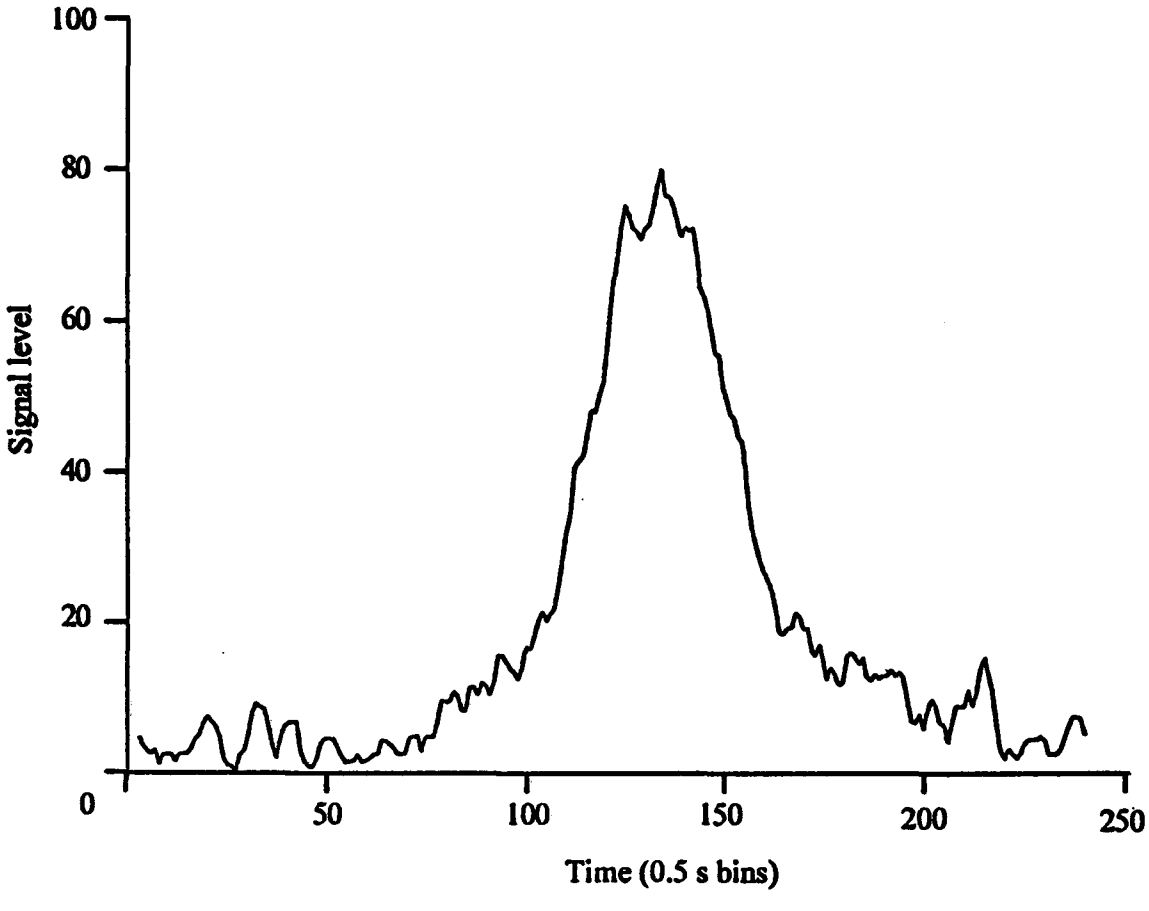

Figure 4.14: A typical line profile for the neon line at 703.404nm

4.8 Data acquisition using the PC

All the data from the experiment passes into a PC. The computer controls the photon counter, and stores the measured counts. The signals from the various photodiodes pass into an analogue-to-digital (A/D) converter, controlled by the computer, and the digital output is stored.

Analogue-to-digital converter

The outputs from the photodiodes monitoring the laser intensity, the iodine bromide signal, the iodine signal and the etalon signal pass into a PCLD-780 terminal board. Each input passes through a low pass filter on the board (R=470kΩ, C=1μF, time constant 0.47s) chosen to match the sampling rate of the photon counter (see section 5.1). The inputs pass to a PCL-818H data acquisition card, inside the PC. This carries out the A/D conversion, and is controlled by the data acquisition program.

Parameter	Default
Number of periods	1500
Gate time	0.5 s
Gate delay	5 ms
Discriminator level	-40 mV
Normalization range	0-1.25 V
Etalon range	0-10 V
Iodine range	0-2.5 V
Iodine bromide range	0-10 V

Table 4.2: Default values for photon counter and A/D converter

Data acquisition program

The data acquisition program used has evolved from the program ACQUIRE2.BAS used on the earlier mercury-argon experiment [45]. We have added a real time graphic display of data. The program is written in GW-BASIC which is sufficiently fast to handle incoming data, as a set of points are taken only every 0.5s. The computer communicates with the photon counter via the serial port and an RS232 interface. The A/D conversion is performed by an internal computer card.

The program first sets up the A/D converter, and the photon counter, using default values. These values are shown in table 4.2. Options are given to change the input voltage range of the PCL818H A/D converter, and the number of counting periods, the time for each period, the gate delay and the discriminator level of the SR400 photon counter.

When these values are set, a subroutine is called to select a filename, based on the day's date and the user's input. The user is also asked whether a plot of data is required, and, if so, what the range of the y-axis is to be.

If a plot is not required, headings for the columns of data are displayed. If a plot is required, then a subroutine is called which draws axes on the screen. Headings for data are also included, but this is restricted to the bottom few lines of the screen (figure 4.15).

The program then waits for the return key to be pressed before starting data collection of one point every 0.5 seconds. The computer repeatedly sends a signal to

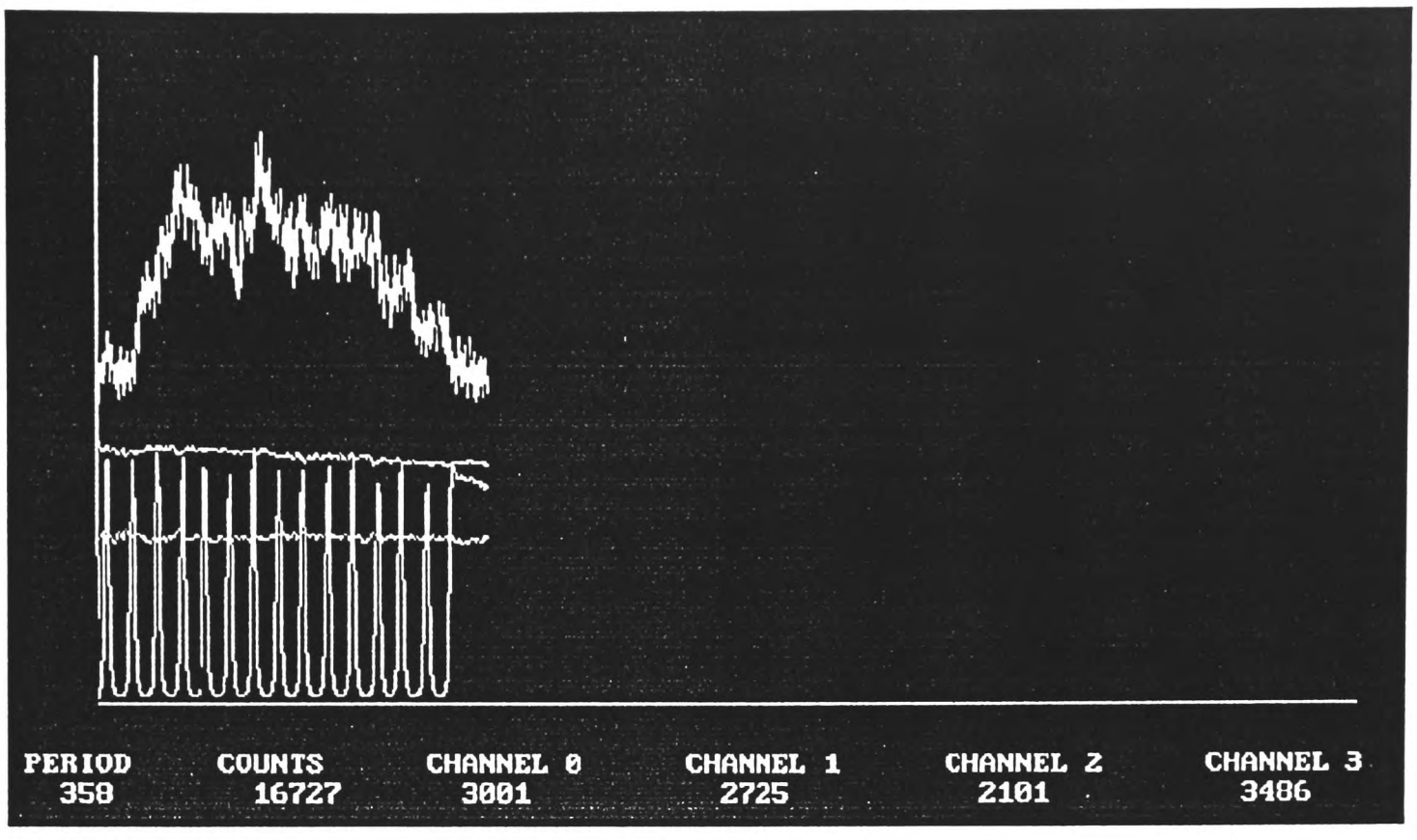

Figure 4.15: Real-time plot as displayed on the screen by the data collection program.

the photon counter. The photon counter sends back a value of -1 until the 0.5s count is complete, when it sends back the number of counts. The computer then triggers an analogue to digital conversion on each of the channels 0 to 3. For each channel in turn, the computer sends a trigger signal, and then checks a status signal from the A/D until the conversion is complete. The computer receives two bytes of data for each channel, and converts these to a decimal number. The computer then displays the photon count and A/D data, either as columns of data or in graphical format with data underneath. The data is also output to file.

4.9 Optimisation of conditions

In order to obtain the best spectra, it is necessary to find the optimum conditions. For both the singlet and the triplet spectra, we chose one band which we always observed when we wished to adjust the apparatus to give the best data. We will look at each of the factors to be optimised in turn, and consider the conditions which affect each. We find when optimising that there is not a single 'best' set of conditions, but that we often have a trade off between different factors.

4.9.1 Signal to noise

To get the best spectra, we need to achieve a high signal level, while minimising the background. For the singlet spectra, this poses little problem, as strong signals can be obtained with little optimisation. The triplet signals are much weaker, and the background much higher (see section 4.9.4) and so to optimise the signals required a great deal of preliminary work.

We found that increasing the oven temperature increased the signal level. This is to be expected, as increasing the temperature increases the vapour pressure of caesium, and hence the number of molecules. We found that we need to heat the oven to at least 270°C to give sufficient signals. The highest temperature used was $\sim$ 350°C, as there is a danger of the solder melting above this. We found that increasing the pressure of the argon buffer gas also increased the signal level, although the effect was less pronounced than for temperature. A gas handling system capable of withstanding pressures of up to 10 atm was constructed to allow the variation to be explored. However, the usable pressure range was limited by the onset of oscillations, which got worse as the pressure increased (section 4.9.4).

A greater signal level was also achieved by using a larger nozzle, since it allows a greater flow of caesium. We initially used 100 and 150μm nozzles, but later moved to a 250μm nozzle. This has the disadvantage that caesium is used up more quickly, but has the advantages of decreasing the level of oscillation and blocking less frequently.

To get the best signal to noise ratio, we also needed to reduce the background level as far as possible. Dark counts were reduced by cooling the photomultiplier, and scattered light was reduced by the design of the optics and baffles. However, we also observed high levels of background from the interaction region itself. This will be discussed in section 4.9.4.

The signal to noise can also be optimised by imaging a selected part of the interaction region. In the case of the singlets, where the signals are strong and there is less background from the interaction region, the best signals were obtained by imaging the central part of the interaction region directly below the nozzle. We initially thought that the same would apply in the case of the triplets. However, we found that a better signal to noise level was obtained if we imaged the edge of the interaction region.

4.9.2 Duration of experiment

Each day that the experiment is run, we load the oven with 1g of caesium. The experiment is then run until the caesium is exhausted. Given the work required to load the oven, and then clean it after use, it is desirable to get as much data as possible from each loading of caesium, and hence for each gram of caesium to last for as long as possible. But as we also need an adequate signal level, we have to compromise. For the triplet spectra, we used a temperature of 300°C as lower temperatures give insufficient signal. For the singlet spectra, the signal levels are higher, and it was possible to run at lower temperatures to maximise the duration. The duration of the run was similarly reduced by using the larger nozzle. The net result has been that as we have optimised to give stronger signal levels, the length of each run has come down from $\sim$ 8 hours to $\sim$ 4 hours.

4.9.3 Resolution

In order to extract the most information from our spectra, we wish to optimise the resolution. In the case of the singlets, we found that some individual rotational lines were resolved far from the band head. In the case of the triplets, the rotational spacing is much smaller and so we were unable to resolve rotational structure.

The main contribution to the linewidth is the Doppler width. For caesium dimers at room temperature (300K), the Doppler width is ~320 MHz. In the free jet expansion, the temperature (i.e. velocity *spread*) is reduced to $\sim$ 10K, but there is now a bulk flow of molecules. We can estimate the velocity of molecules in the beam from the predicted terminal velocity of the free jet expansion [41]

$$V_\infty = \sqrt{2\hat{C}_p(T_0 - T)} \tag{4.2}$$

where T_0 is the temperature in the oven, T is the final temperature, and $\hat{C}_p$ is the heat capacity at constant pressure. Where the jet contains more than one species, a weighted average heat capacity should be used. However, we will assume that the amount of caesium in the beam is negligible, and that we can use $\hat{C}_p = \frac{5}{2}\frac{R}{W}$ for argon, where W is the molecular weight. Taking $T_0 = 600$K, $T = 10$K and W=0.04kg mol^{-1} gives $V_\infty \sim 780$ ms^{-1}.

In the beam, the spread of velocities due to the temperature contributes little to the Doppler width. However, molecules in different parts of the beam are travelling at different angles, and so have different components of velocity parallel to the laser

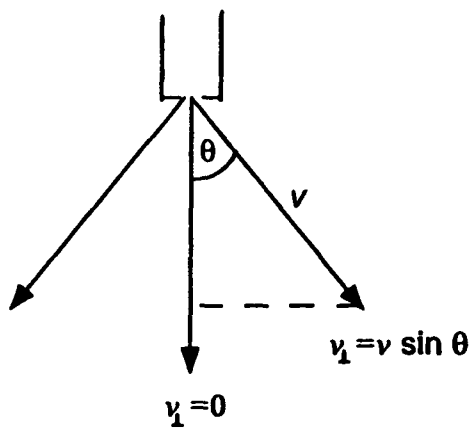

Figure 4.16: Molecules in different parts of the beam are travelling in different directions, and so have different perpendicular velocity components, and different Doppler shifts.

beam. It is this spread of velocity components which leads to the Doppler width (figure 4.16). The frequency spread corresponding to the full range of angles from $-\frac{\pi}{2}$ to $\frac{\pi}{2}$ is over 2GHz. By using a narrow slit to image only a narrow velocity class of molecules, we can reduce this Doppler width. Ideally, we would image directly below the nozzle, where the molecules have close to zero velocity parallel to the laser beam. But because of the need to obtain stronger signals, in recording our final data for the triplets we have imaged to one side. This leads to a shift in the position of the lines because the average component of velocity of the molecules imaged is non-zero. There may also be a greater spread of velocities, and so a greater width, because the height of the slit now also adds to the range of velocities sampled. We have made a rough estimate of the Doppler width for a slit directly below the nozzle, and for a slit off centre by 5mm (figure 4.17). We have assumed that the slit is 1mm wide, and that the nozzle is 5mm above the interaction region (the conditions used for the triplet spectra). We have also assumed that the effective height of the interaction region is 1.5mm. Although the slit itself has a greater height, the size of the interaction region is dependent on the height of the laser beam, which we estimate to be 1.5mm. From these figures, we have calculated the component of velocity parallel to the laser beam at the edges of the slit, and calculated the Doppler shift corresponding to each velocity. We have then estimated the Doppler *width* as the difference between the Doppler shifts at the edges of the slit, and the *average shift* as the mean of the shifts at each edge. We also performed the calculation for a slit width of 0.5mm and a nozzle height of 12mm (the conditions used for the singlet spectra). The results are shown in tables 4.3 and 4.4. These calculations show that although the Doppler width actually decreases slightly when the slit is off centre, a large shift is introduced,

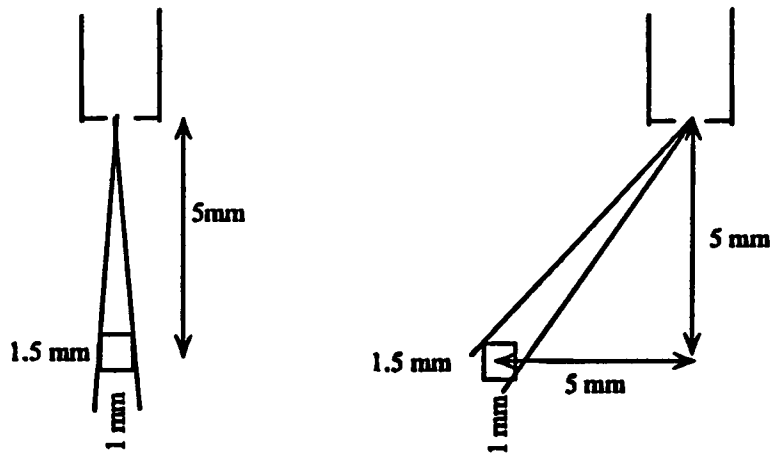

Figure 4.17: Dimensions used to calculate the Doppler width and shift for two positions of the slit.

	Width (MHz)	Shift (MHz)
Slit centred	255	0
Slit 5mm off-centre	190	770

Table 4.3: Estimated Doppler widths and shifts for a 1mm slit with a nozzle height of 5mm.

which will lead to a systematic error in the peak positions. We will compare these predictions with the experimental results in section 5.3.

In order to minimise the Doppler width, we therefore wish to use a narrow slit and to raise the nozzle as far as possible. However, since this will decrease the signal, we need to find an appropriate compromise. In the case of the singlets, the signal was sufficiently strong that we could use a 0.5mm slit and raise the nozzle to ~12mm above the laser beam. For the triplets, we used a 1mm slit, with the nozzle ~ 5mm from the laser beam.

When analysing the experimental line shapes, we found that there was an addi-

	Width (MHz)	Shift (MHz)
Slit centred	50	0
Slit 5mm off-centre	80	420

Table 4.4: Estimated Doppler widths and shifts for a 0.5mm slit with a nozzle height of 12mm.

tional Lorentzian contribution (see section 5.3).

4.9.4 Oscillations

When studying the singlet spectra, the background remained small compared with the signal level, but in the case of the triplet spectra, we observed that the molecular signal was on top of a high background level. This background was also present when we were tuned to a region where no molecular signal was present, and could be observed both with the photomultiplier and the CCD camera. An additional problem was presented by the fact that the background was not steady, but often had large fluctuations in intensity; sometimes these were erratic and unpredictable, and sometimes there was a regular oscillation, with frequency of the order of a few Hz. These oscillations were often large compared with the signals, and so it has been necessary to reduce the oscillations. This has proved a major problem in trying to obtain good triplet spectra, and much time has been devoted to it.

We investigated the conditions affecting the oscillations in an attempt to reduce them. In these early observations, we used a nozzle of 150μm diameter. We first checked that the oscillations were the same whether or not the laser was scanning. Hence we ruled out the possibility that the oscillations were actually genuine spectra. We observed that the high background levels and oscillations were there both when we were tuned to a region of triplet absorption, and when we were tuned well away from any bands. We then studied what happened when no caesium was present, and found that the background level was very low, and so no oscillations were discernible. We observed that the background level varied with the amount of caesium estimated to be in the beam; as the oven was heated, the background increased, and the background level fell as the caesium ran out. We found that as the oven heated up, the background had large random fluctuations, but that at an oven temperature of 300°C, the fluctuations settled into a steady oscillation.

We next investigated the effect of argon pressure on the oscillations. We found that as we increased the pressure, the oscillations became larger relative to the signal. At pressures above about 2 atm, the steady oscillation reverted to apparently random large fluctuations. We also observed that the level of oscillation for a given pressure was worse if the nozzle was partially blocked. This suggested that it could be better to use a larger nozzle. We switched to a 250μm nozzle, and found that the oscillations were reduced. We tried to reduce the pressure to a level where they were sufficiently

small to obtain good spectra, but found that at pressures below about 1 atm there were once again erratic fluctuations. However, we noticed that the flow rate of the argon varied in a similar way. We added a secondary regulator to the argon supply, and the flow rate was once again steady.

The oscillations are clearly associated with fluctuations with time of the species responsible for the background fluorescence, which certainly contains caesium, due to instabilities of the mass flow. The problem in the case of the triplets was that the background was so large that the oscillations in it dominated the spectra of interest.

At this point we discovered that at a pressure of 1.2 atm there was sufficiently little oscillation to take meaningful spectra, although the background level was still very high, leading to noise on the signals. We were able to study the strongest band with this arrangement, although we were unable to study the other vibrational bands.

A caesium-argon mixture is known to absorb in this wavelength region [59], corresponding to extreme line broadening by the argon of the forbidden S to D atomic caesium transitions at 685 and 690 nm. This is the same caesium electronic transition as for the caesium triplet spectra, but as the ground state interaction between caesium and argon is repulsive, the absorption is continuous rather than having discrete lines. The absorption becomes stronger for shorter wavelengths, as the forbidden atomic transitions at 684.9nm and 689.5nm are approached, and so we would expect the background level to increase as the wavenumber decreases. We tested this by measuring the background level at different frequencies. We took scans over different regions, and then found the background level for each region, ensuring that there was no signal due to caesium dimers. The results are shown in figure 4.18. There is no strong trend in the data, and so we were not able to confirm the role of caesium-argon absorption.

We then tried using neon buffer gas instead of argon buffer gas. Caesium-neon has also been found to absorb in the triplet region [59], but the absorption is weaker. Figure 4.19 shows singlet spectra taken with argon and neon, and a scan in the region of the triplet spectra taken with neon. The signal to background ratio when neon was used was worse than when argon was used. In addition, when neon was used there were large erratic fluctuations in the background, as seen in 4.19 b and c, instead of the steady oscillation seen when using argon. These erratic fluctuations mask any real signal far more than a steady oscillation. On the basis of these results, we decided that there was no advantage to be gained from using neon, and so we carried out the

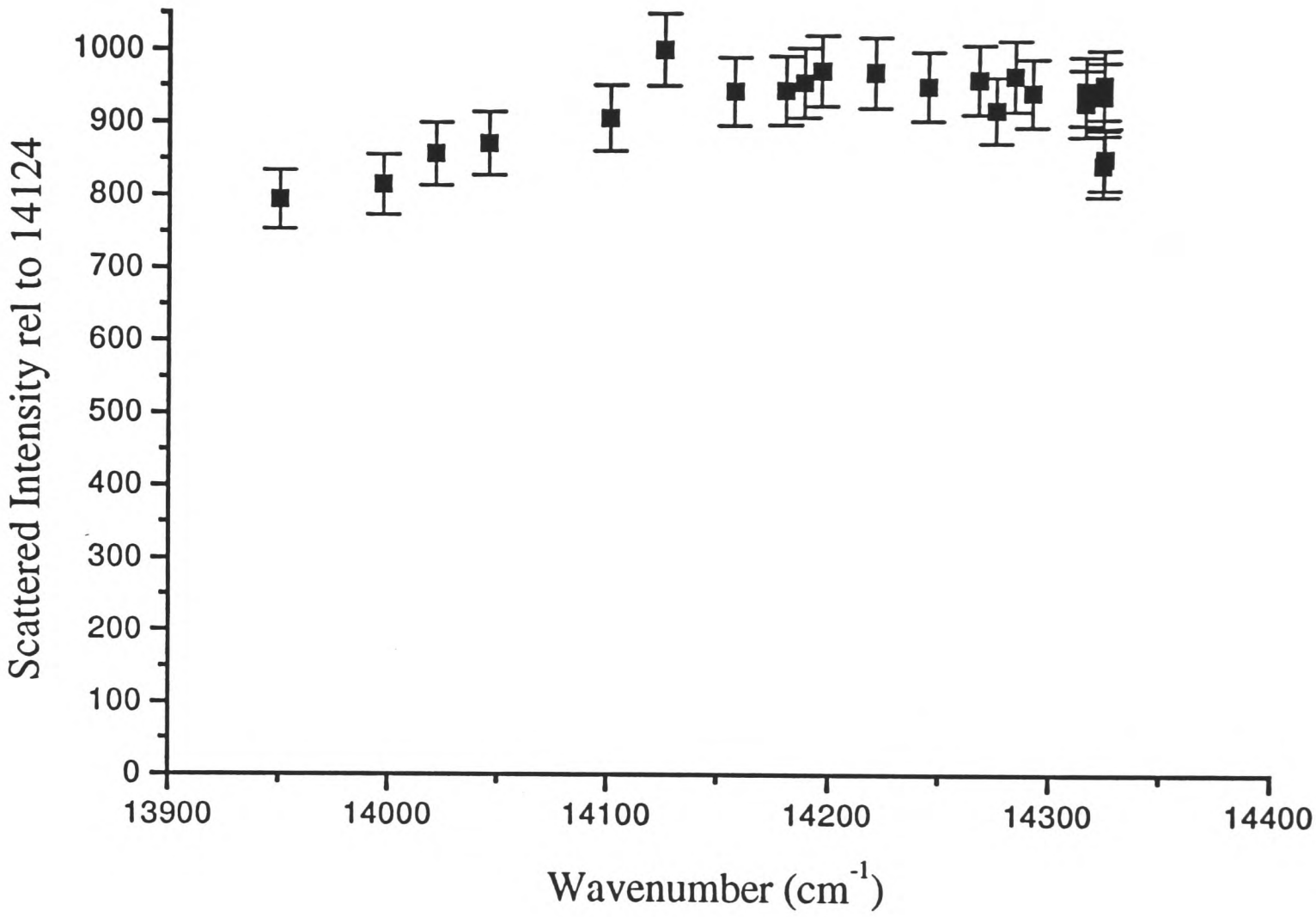

Figure 4.18: Plot of background level against wavenumber to test hypothesis that caesium-argon is responsible for the high background.

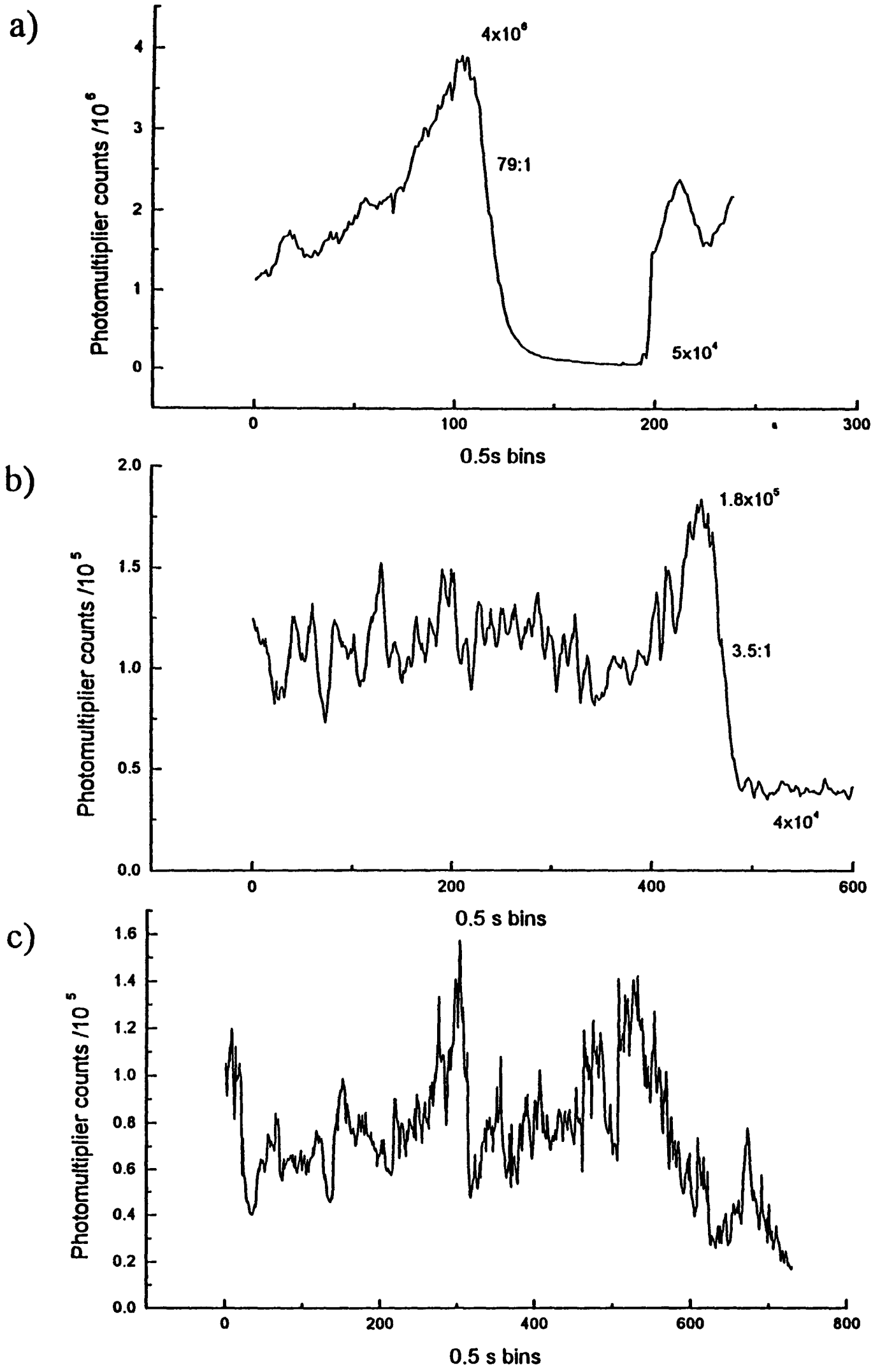

Figure 4.19: a) Singlet spectrum with argon buffer gas. b) Singlet spectrum with neon buffer gas. c) Triplet region with neon buffer gas.

rest of the experiments with argon buffer gas.

The major breakthrough occurred when we observed using the CCD camera that the strongest triplet fluorescence was outside the central intense part of the interaction region. By adjusting the slit so that we imaged this region of fluorescence, we were able to maintain an adequate signal level, while the background level was drastically reduced (figure 4.20). The level of oscillation was similarly reduced. By offsetting the slit in this way, we were able to study the weaker triplet bands. The residual oscillation can still be seen on the spectra, as for example, in figure 5.1.

Thus, as one would expect, the oscillations, which are indicative of instabilities in the flow, are still present at the offset position. However, the point is that quite a small oscillation on a large background masks any weak triplet signals, so that when the signal/background is significantly better, the oscillations are much less serious.

4.9.5 Effect of laser polarization

The light emitted from the dye laser is vertically plane polarized. The light becomes horizontally polarized by the periscope before entering the vacuum can. Our calculations in section 5.6 show that we would expect different relative intensities for the P,Q and R branches depending on the polarization of the incident light. We tested this by taking singlet spectra under the same conditions for both horizontally and vertically polarized incident light. To rotate the plane of polarization, we used a quarter wave plate and a crystal polarizer. We set the polarizer to transmit light of the desired polarization, and then rotated the quarter wave plate until the maximum intensity was transmitted through the polarizer. The results are shown in figure 4.21. This shows that when the two spectra are overlapped for the strongest Q branch lines, the difference between the intensities of the weaker R branch lines is clearly visible. This confirms that the intensity of the branches is sensitive to polarization, and that we must take this into account when fitting a theoretical model to the spectra.

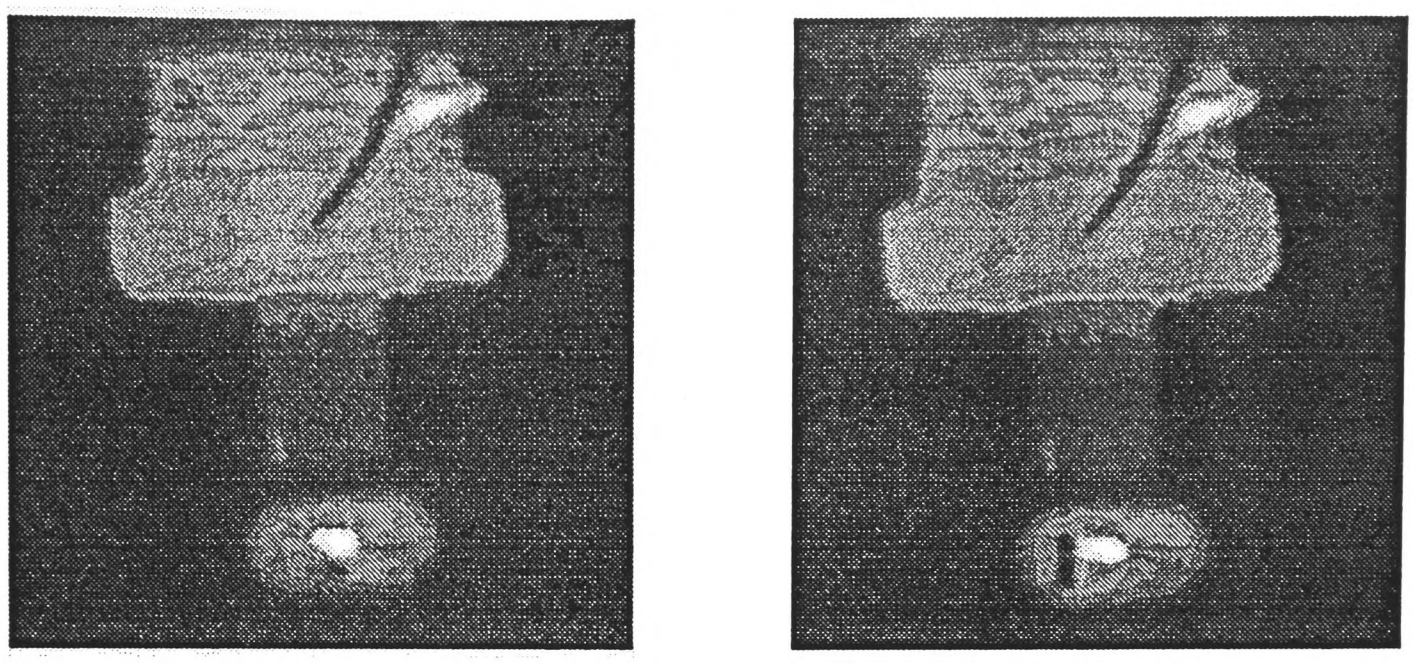

Figure 4.20: CCD camera image of showing the slit imaging the centre of the interaction region (left) and imaging the fluorescence to the left of the centre. (right).

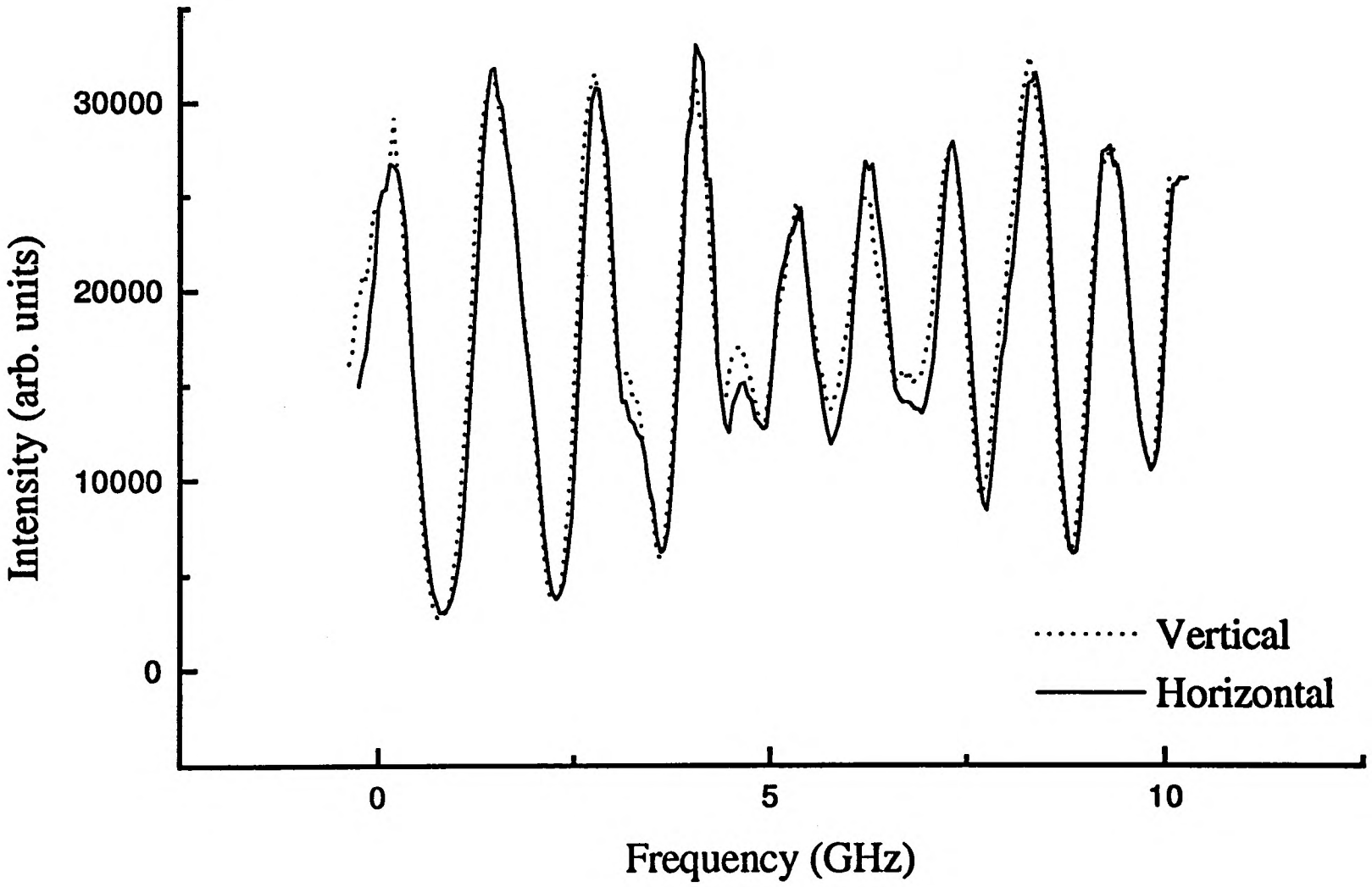

Figure 4.21: Singlet spectra for horizontally and vertically polarized incident light. The intensities of the spectra have been scaled slightly ($< 5\%$) to overlap the spectra

Chapter 5

Analysis and results

In this chapter we present the observed singlet and triplet bands. A theoretical model is formulated to explain the observed singlet spectra. In the case of the singlet spectra, the model can be optimised to the experimental data by least squares fitting. For the triplet bands we deduce accurate values for the frequencies of the peaks of the bands.

5.1 Normalising and linearising the raw data

The raw data from the experiment consists of a series of data files, each corresponding to an individual laser scan over 20 to 30GHz. A typical example is shown in figure 5.1. Each file has at least six columns: the data point number, the counts from the photon counter, and outputs from photodiodes measuring laser intensity, etalon transmission, iodine bromide transmission and iodine transmission. The data points are taken at equal intervals of time, so the spacing in frequency depends on the scan speed of the laser. This speed is not the same from run to run, and even varies slightly within a single scan. Before making any further analysis of the scans, it is necessary to normalise the signals using the laser intensity data, and add a linear frequency scale using the etalon fringes. This is done using a set of computer programs which act on the raw data files.

- **Normalization**

The program NORMAL.PAS reads in the data file, subtracts the background counts (i.e. the number of counts measured with the laser blocked) and then divides the photomultiplier counts and the photodiode signals by the signal representing laser intensity. We initially found that normalisation was poor, as the variations in intensity

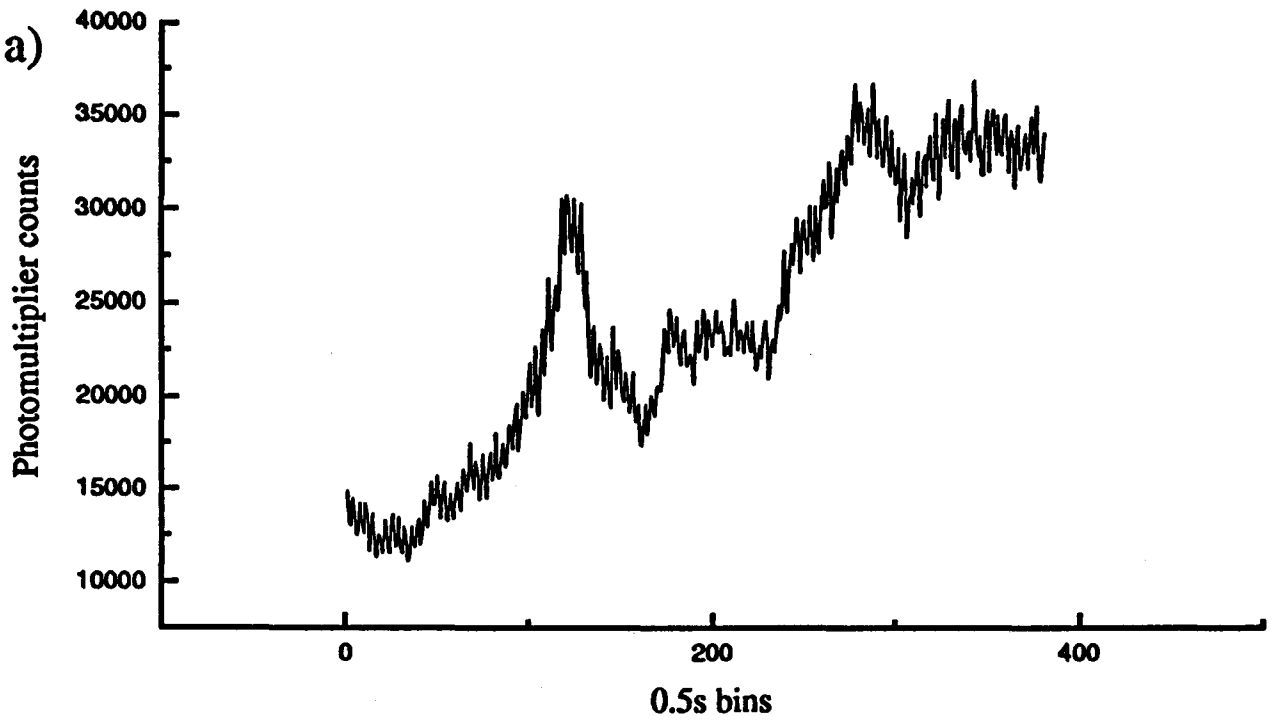

Bin No.	Photomultiplier	Normalization	Etalon	Iodine	Iodine bromide
1	14887	3048	114	2086	3705
2	13218	3059	123	2070	3705
3	13047	3071	137	2052	3700
4	14461	3088	163	2018	3687
5	13595	3084	207	2030	3677
6	12510	3076	315	2062	3695
7	12871	3082	751	2052	3710
8	14225	3088	1626	2049	3689
9	13048	3080	2151	2074	3681
10	12618	3080	2442	2082	3675
11	14191	3088	2994	2051	3662
12	13429	3106	2101	2024	3639

Figure 5.1: Typical plots from raw data, for a) photomultiplier counts and b) photodiodes (note the different scales). Also shown is part of a typical data file.

observed in the normalisation signal did not correspond to the variations observed in the photomultiplier signal. We suspected that this was because the photon counter gives the total number of counts over a 0.5s period, while the A/D converter gave signals from a shorter time period, as the time constant of its low pass filter was then 0.15s. We increased this time constant to 0.45s to be comparable to the summation time of the photon counter. We found that the normalisation was improved, although it was still not perfect. We then considered the possibility that movement of the laser beam on the normalisation photodiode was giving an incorrect intensity level. We focussed the beam onto the photodiode with a lens, and found that the normalisation was slightly improved. However, as the noise on the triplet spectra was now dominated by fluctuations in the caesium beam, rather than the laser intensity, we did not pursue the problem of normalisation further. We found it preferable to spend more time adjusting the laser to give a stable output power so that normalisation was less important.

- **Selecting etalon peaks**

The program FRINGE.PAS reads the normalised data file, and then finds the positions of the etalon peaks. The centre of each peak is determined by fitting a parabola to the top three points of each peak, and finding the peak of the parabola. The program displays the etalon signal on the screen, and asks the user to select which peaks are to be used by the spline fitting program. The positions of the peaks and the number of data points are written to a data file.

- **Spline fitting**

The program SPLINE.FOR fits a cubic spline to the peak positions to establish a linear frequency scale for each scan. Since the frequency scale is unreliable outside the range of the etalon peaks, the program includes in its output the range over which the frequency scale is reliable.

- **Adding the frequency scale to the normalised data.**

The program ADDSPLIN.PAS reads in the frequency scale from the spline fitting program and the normalised data, and combines the files to give a single normalised, linearized data set over the range for which the spline fit is reliable.

5.1.1 Absolute frequency calibration

The result is a series of scans with a relative GHz frequency scale, each beginning at 0GHz. For the triplet spectra, we have assigned an absolute frequency scale to the scans. For this, we use the iodine spectrum, together with the known positions of the iodine lines from [50]. There is typically only a single iodine line on each scan, and so we can only use them to find the absolute frequency scale on a single scan once a relative scale has been established.

First, a rough absolute frequency scale is established by using the wavemeter reading at the start of the scan. This allows lines in the observed iodine absorption spectrum to be matched to the corresponding lines in the atlas. Then the peak of each experimental iodine line is found. An offset is then added to the frequency values so that the frequency at the peak of the iodine line is the same as that given by the atlas. We have found the experimental iodine line positions by judging by eye from a plot. This is quick and simple, but gives an error of ~200MHz. This is greater than the error in the absolute values given by Gerstenkorn and Luc [50] (about 50MHz), and is the dominant source of error in the calibration. However, since we can only find the peak of the caesium band to ~ 300MHz due to the level of noise, this method of calibration is adequate for the current analysis. If a more detailed rotational analysis of the triplet bands were to be attempted, a better calibration could be obtained by fitting a suitable line profile to the iodine spectra to find the peaks.

In the case of the singlet bands, we have only used a rough calibration from the wavemeter readings, in which case the error is of the order of 5GHz ($0.17cm^{-1}$)(error in wavemeter reading of $0.1cm^{-1}$, error in correspondence between wavemeter reading and start of scan of $0.07cm^{-}1$).

5.1.2 Combining adjacent scans

Since each band is generally several scans wide, we wish to be able to patch together consecutive scans to produce a single plot of the region. This requires both the frequencies and intensities of adjacent scans to be matched.

Frequency matching

Where an absolute frequency scale has been established using the iodine calibration for adjacent scans, then the two scans will already be on the same frequency scale.

However, this is often not the case, as there are not suitable iodine features on every scan. We must then use other features to join up the scans. We first look for an iodine bromide feature in the overlap region of the two scans, using wavemeter readings and etalon fringes as a guide to check that it is the same feature appearing on both scans. If there is no suitable IBr feature, we next look for a matching feature in the caesium spectrum itself. In either case, we then add an offset to one of the scans without an absolute calibration, so that the frequencies of the feature chosen are the same for the two scans. The error in the frequency between adjacent scans joined in this way is $\sim$ 200MHz. If there is no suitable feature, then we use the wavemeter readings to try to deduce the correspondence between etalon fringes in the two scans; this is less satisfactory because the etalon may drift between scans. The wavemeter alone is not sufficiently accurate to be able to unambiguously match etalon fringes, and so there may be an error of 1 or 2 fringes ($\sim$ 2GHz or 0.07cm^{-1}). This may be overcome if any additional information from the spectra can be used. In practice, this only occurred occasionally at the extremes of the bands, and none of the numerical data relies on scans matched in this way.

Intensity matching

When we plot the scans on the same frequency scale, as deduced above, we often find that the intensity of the signals is different for the two scans. This may be due to changes in the amount of caesium molecules present in the beam, or other changes in observation conditions. In order to join the two traces, we add a fixed background and/or multiply the signal by a fixed factor across the scan. The values are chosen by eye from plots, and so are not very reliable, especially when the caesium spectrum has little structure for guidance.

We can then plot the adjacent scans on the same scale, delete the data in the overlap region, and then save the data in a single data file. This method is sufficiently accurate to produce good plots of the spectra, but should not be relied on when fitting a theoretical model to the data; in this case, each scan must be fitted separately, and the scans joined afterwards.

5.2 Singlet spectra

Although the singlet spectra have been well studied previously by Demtröder et al. [29], we found it of great value to study them using our experimental apparatus. We were initially unable to observe any triplet spectra, and so we were able to use the singlet spectra to optimise our experimental setup and techniques.

5.2.1 Vibrational band positions

We were able to record 22 bands of the $B^1\Pi_u \leftarrow X^1\Sigma_g^+$ system. Using the wavemeter, we were able to find the position of these bands to an accuracy of $\tilde{<}0.2\text{cm}^{-1}$. These values are recorded in table 5.1. For comparison with the previous data, we have calculated predicted positions from the band head using the X state Dunham coefficients of Weickenmeier [25] and the B state Dunham coefficients of [29]. These are also shown in the table in italics. We were not able to make a more accurate calibration of the wavenumbers as the iodine spectra are very weak in the singlet region, and there is more noise on the laser intensity because the laser is running further from the peak of the dye; hence we could not observe any iodine absorption above the noise.

Our results are in good agreement with the calculated line positions. This confirms that our wavemeter calibration is accurate to the level of 0.1cm^{-1} and that our program to calculate line positions from Dunham coefficients works correctly. We did not take further measurements of the vibrational band positions, as we clearly agree with the previous results of [29], and we cannot hope to improve on their resolution (125MHz for polarization spectroscopy [25]) with our experimental apparatus.

5.2.2 Rotational structure within a band

We then concentrated on a single band, the $v' = 3 \leftarrow v'' = 0$ band, in order to study the rotational structure more closely. This provides a good test of the resolution and signal to noise ratio provided by the experiment.

Scans were taken over four overlapping frequency regions to cover the band. The conditions were optimised as described in section 4.9 to give the best signal to noise ratio and resolution. Our optimised conditions were a pressure of 1.4 atm and a temperature of 325°C, with the sliding slit of 0.5mm width set to image the centre of the interaction region, and the nozzle about 12mm above the laser beam.

v'	$v''=0$	$v''=1$	$v''=2$	$v''=3$
1	13074.2			
	13074.19			
2	13108.3			
	13108.21			
3	13142.2			
	13142.06			
4	13175.9		13092.1	
	13175.75		*13092.21*	
5	13209.4	13167.4	13125.8	
	13209.27	*13167.42*	*13125.73*	
6	13242.5.	13200.8	13158.5	13117.6
	13242.62	*13200.77*	*13159.08*	*13117.56*
7	13275.5	13233.9	13192.3	13150.2
	13275.81	*13233.96*	*13192.27*	*13150.75*
8		13267.0	13225.3	13183.8
		13266.97	*13225.29*	*13183.76*
9			13258.0	13216.5
			13258.13	*13216.61*
10			13290.8	13249.2
			13290.81	*13249.29*

Table 5.1: Wavenumbers of the singlet bands, as measured in this work, and calculated from the coefficients of [29, 25] (*in italics*)

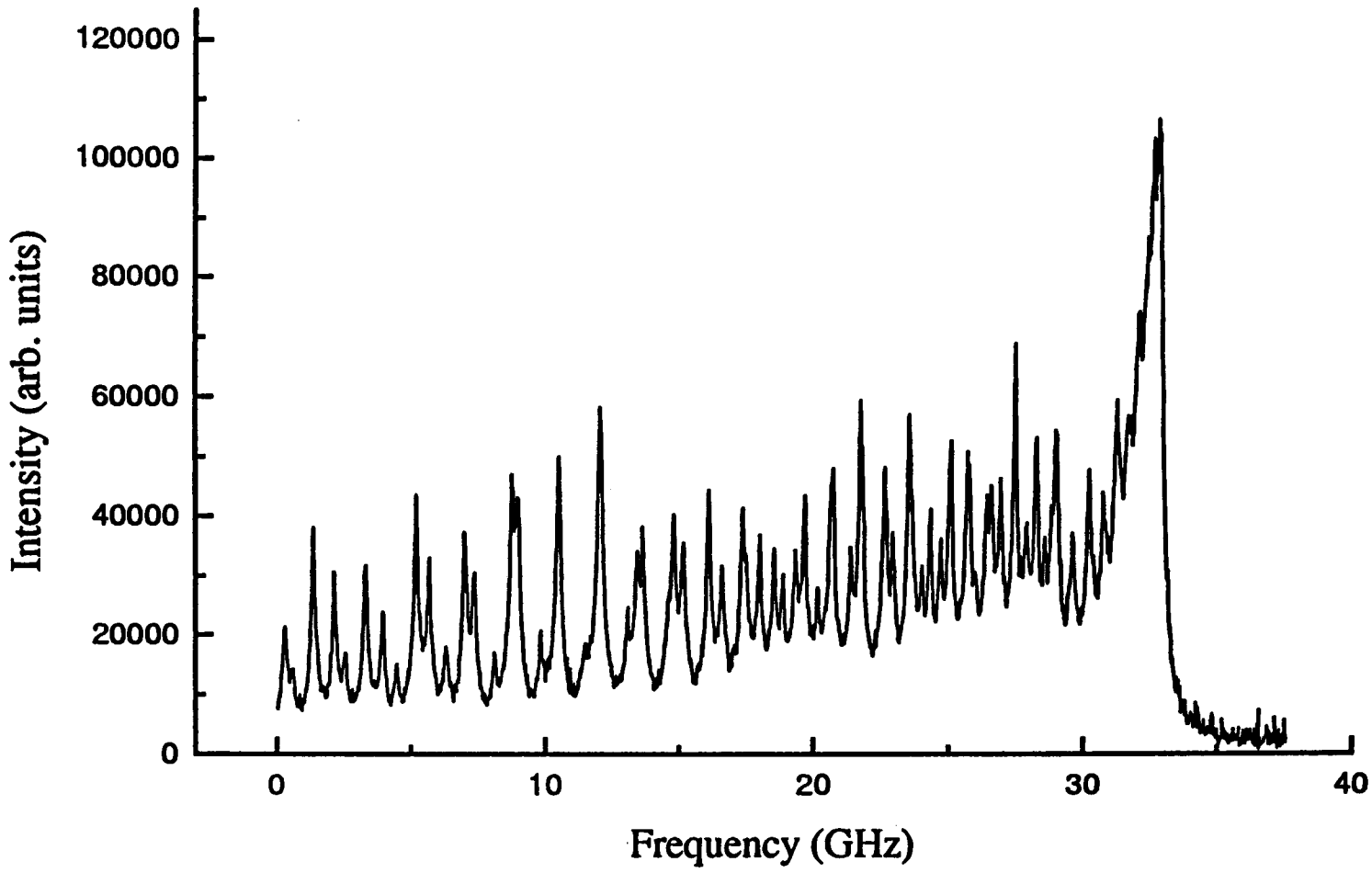

Figure 5.2: $v' = 3 \leftarrow v'' = 0$ singlet band.

The scans were normalised and linearized, as described above, and then patched together to give a plot of the whole band. This is shown in figure 5.2. As we were not able to obtain good iodine calibration spectra in this frequency region, we have not been able to assign an absolute frequency scale.

From this spectrum we can find the linewidth by measuring the full width at half maximum of one of the resolved peaks. In this way we find an approximate linewidth of 200MHz. However, the full interpretation of the profile is quite complex (see below).

5.2.3 Fitting theoretical profiles to experimental data

We wish to extract the rotational constants and linewidths from the experimental singlet spectra. Although we had reduced the linewidth to roughly 200MHz, the spectrum is still very complex, with the region around the bandhead largely unresolved. In order to calculate the rotational constants and linewidths, we must construct a theoretical model of the molecular spectrum in terms of these parameters, and then find the values of the parameters which give the best fit to experimental data. As we find that we need 13 parameters, we have used a computer program based on the NAG Fortran library least squares optimisation routine E04FDF.

In the program, the user supplies a routine LSFUN1 to calculate the model curve from a set of parameters, and to calculate the set of residuals from the difference between the model curve and the experimental data. The optimisation routine then finds the values of the parameters which minimize the sum of the squared residuals. The user must supply the initial values for the parameters. These must be chosen with care, as the optimisation routine will only find the best fit if the starting values are sufficiently close to the best values. The details of the theoretical model used are given below.

We fitted to individual scans rather than to the whole band, as inaccuracies in joining consecutive scans makes fitting across more than one scan difficult.

Line positions

The first step in modelling the line positions is to find the line positions. We are interested only in the rotational structure of the band; the vibrational band position is given as an offset added to all line positions. Using the Dunham coefficients given in [29] and [25] we calculated that we would only require the first two rotational constants; we predicted that higher order terms would give changes less than 1/10 of the linewidth for $J < 100$. Hence the line positions are given in our model by

$$\overline{\nu} = C + B'_v J'(J'+1) - B''_v J''(J''+1) - D'_v J'^2(J'+1)^2 + D''_v J''^2(J''+1)^2. \quad (5.1)$$

Line intensities

The next step is to calculate the relative intensities of each of the lines of the band. Our initial approach was that of section 2.5.4 i.e the population of the initial state is given by a Boltzmann distribution, and the relative transition rates are given by the Honl-London factors. However, we found that the agreement with the experimental data was not satisfactory. Figure 5.3 shows the experimental data and the fitted profile using this intensity model, for the middle of the band (figure 5.3a), and for the bandhead (figure 5.3b). This shows that the large peaks (the Q branch) are fitted well, but the smallest peaks (the R branch) are consistently underfitted. This was because the assumptions made in section 2.5.4 do not strictly hold. We must therefore relax these assumptions to develop a more sophisticated model of intensities.

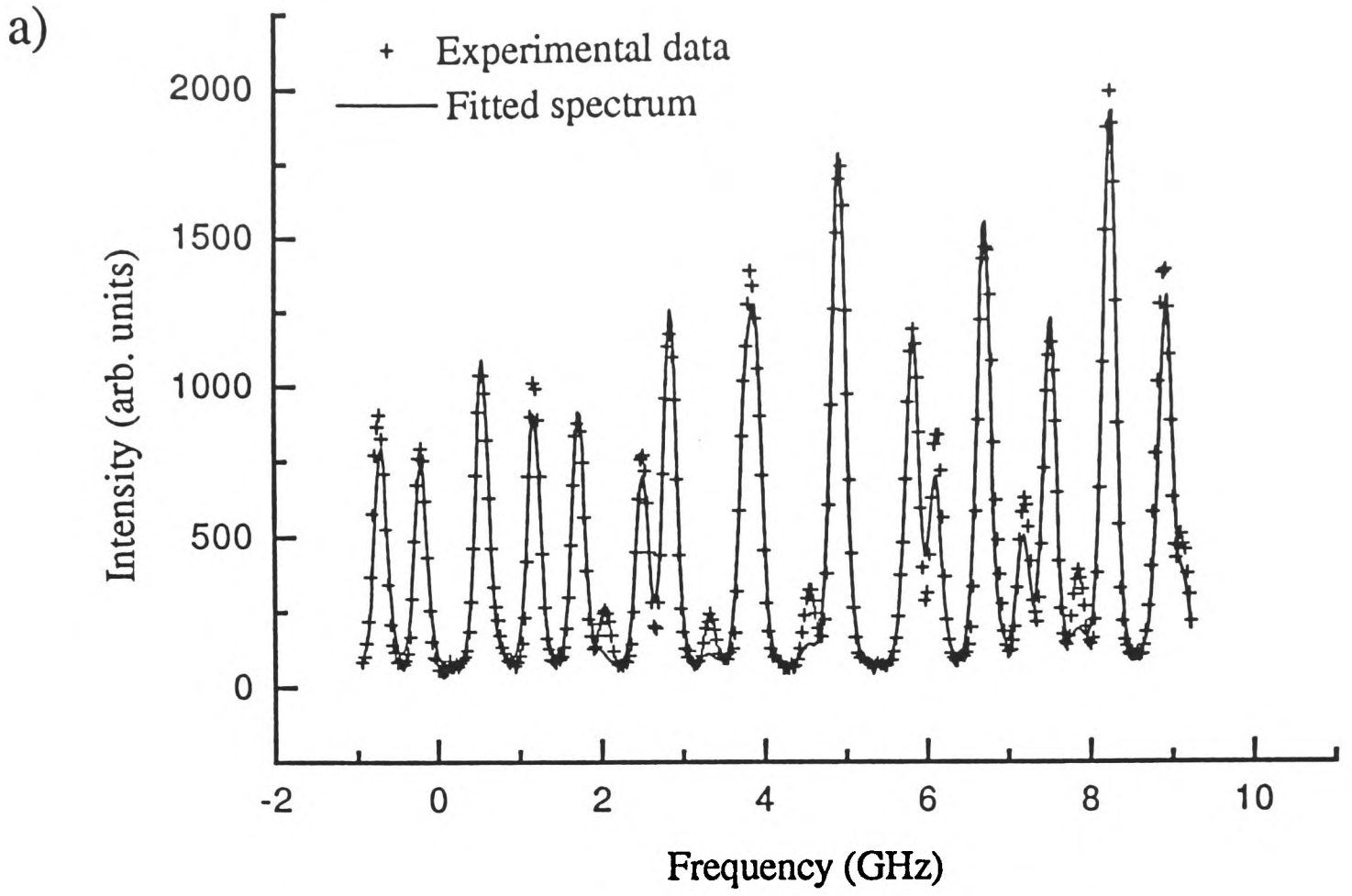

Figure 5.3: Fitted profile using simple Honl-London model for intensities for a) a section of the middle of the band and b) the bandhead. The smallest peaks are consistently underfitted.

5.3 Complex model of rotational transition probabilities

In order to find a better description of the intensities, we must examine the assumptions made in the simple case. Firstly, our detector does not cover all solid angle. Light is focussed onto the detector if it passes through a 9mm by 5mm slit at a distance 25mm from the interaction region. This covers roughly 0.5% of the total solid angle. Since light is detected in almost a single direction, photons from certain transitions, where emission is in a predominantly different direction, may be detected only weakly.

Secondly, we need to take into account the fact that each molecule will undergo more than one excitation cycle. We can make a rough estimate of the number of transitions by considering the transit time of a molecule.

The diameter of the laser beam is $\sim$ 1.5mm. We estimated the velocity of the molecules in the beam to be 780ms^{-1} in section 4.9.3. The time for the molecule to cross the beam is therefore $\sim 10^{-6}$s. Taking the time for a cycle to be given by the time for spontaneous emission for the singlets to be $\sim 10^{-8}s$ from section 2.5.2, then each molecule would go through $\sim$ 100 cycles while in the beam if it returned to its initial state each time. But in each cycle, a proportion of the molecules will return to other non-resonant states, and will no longer interact with the laser light. After 100 cycles, virtually none of the molecules will remain in the absorbing state. Hence the effects of optical pumping into non-resonant states will become significant.

To take these factors into account, we have developed a more complex model for transition probabilities. We now consider both the absorption and emission rates, the direction and polarization of the emitted photons, and the final states after emission.

Using the Wigner-Eckart theorem [60], the rotational term of the transition probability can be written as

$$|<\psi_f^r|\hat{\mathrm{r}}\hat{\epsilon}^{\pm 1}|\psi_i^r>|^2 = \frac{4\pi}{3} D_{\hat{k}}(\hat{\epsilon}) \begin{pmatrix} J_i & 1 & J_f \\ -m_i & \Delta m & m_f \end{pmatrix}^2 \times |<a_f J_f||D_1||a_i J_i>|^2 \quad (5.2)$$

where $\hat{\epsilon}^{\pm 1}$ represents the dependence on the polarisation of the incident light. For absorption transitions, with light linearly polarized parallel to $\hat{z}$ and direction of incidence along $\hat{x}$,

$$D_{\hat{k}}(\hat{\epsilon}) = \frac{1}{2}\delta_{\Delta m,0} \quad (5.3)$$

and so only transitions with $\Delta m = 0$ are possible. The line strength factor, S_{J_i,J_f} is given by [41]

$$S_{J_i,J_f} = \frac{4\pi}{3} | < a_f J_f || D_1 || a_i J_i > |^2 \tag{5.4}$$

S_{J_i,J_f} can be calculated for pure Hund's cases. For Hund's case (a), which is the approximation we are using in the caesium molecule,

$$S_{J_i,J_f} = \gamma \begin{pmatrix} J_i & 1 & J_f \\ -\Omega_i & \Delta\Omega & \Omega_f \end{pmatrix}^2 (2J_i + 1)(2J_f + 1) \tag{5.5}$$

where $\gamma = 1$ for $\Delta\Omega = 0$ and $\gamma = \frac{1}{4}$ for $\Delta\Omega = \pm 1$.

Considering a $^1\Sigma \rightarrow ^1\Pi$ transition, this gives

$$| < \psi_f^r | \hat{\mathbf{r}} \hat{\epsilon}^{\pm 1} | \psi_i^r > |^2 = \frac{1}{8} \begin{pmatrix} J_i & 1 & J_f \\ -m & 0 & m \end{pmatrix}^2 \begin{pmatrix} J_i & 1 & J_f \\ 0 & 1 & -1 \end{pmatrix}^2 (2J_i + 1)(2J_f + 1) \tag{5.6}$$

For absorption, $\Delta m = 0$. Evaluating equation 5.6 from a lower state (J'', m) to an upper state (J', m) gives the relative rates for transitions in table 5.2.

J''	m''	J'	m'	
J	m	J	m	$\frac{m^2}{2J(J+1)}$
J	m	$J-1$	m	$\frac{(J+m)(J-m)(J-1)}{2J(2J+1)(2J-1)}$
J	m	$J+1$	m	$\frac{(J+m+1)(J-m+1)(J+2)}{2(2J+3)(2J+1)(J+1)}$

Table 5.2: Table of relative transition rates for absorption

We must now consider spontaneous emission more carefully. For spontaneous emission, the factor $D_{\hat{k}}(\hat{\epsilon})$ has an angular dependence, and is given by (summed over emitted polarisations)

$$\begin{aligned} \sin^2 \hat{k} \quad & \text{for } \Delta m = 0 \\ 1 + \cos^2 \hat{k} \quad & \text{for } \Delta m = \pm 1 \end{aligned} \tag{5.7}$$

where $\hat{k}$ is the angle between the direction of emission, and the direction along which J is quantised ($\hat{z}$ in this case) [41].

We can take into account the two different laser polarisations by careful choice of axes, as shown in figure 5.4. Then the calculation of absorption rates will be the same

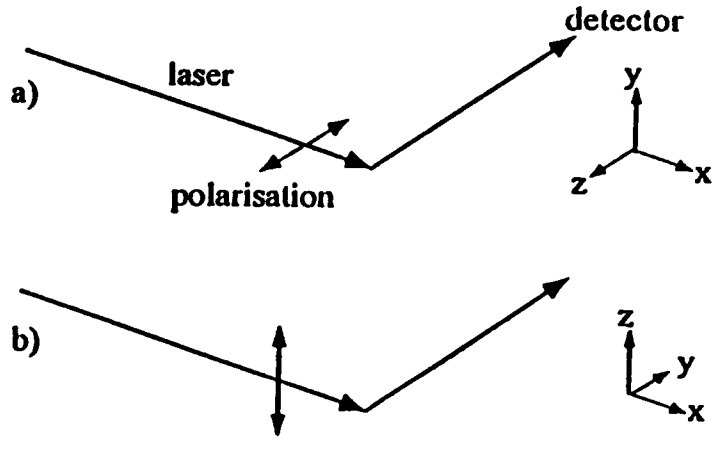

Figure 5.4: Choice of axes for a) horizontal polarization and b) vertical polarization

	$\Delta m = 0$	$\Delta m = \pm 1$
vertical	0.00569	0.00573
horizontal	0.00122	0.29900

Table 5.3: $D_{\hat{k}}(\hat{\epsilon})$ values for horizontal and vertical polarisations

for both polarisations, while the factors $D_{\hat{k}}(\hat{\epsilon})$ in (5.7) will be different for the two polarisations. These factors can be calculated once and for all by integrating (5.7) over the area of the slit (table 5.3).

We also need to evaluate equation 5.6 for each of the possible downwards transitions. Unlike the case for absorption, we now have transitions with $\Delta m = 0, \pm 1$, with $\Omega = 1 \rightarrow \Omega = 0$, giving the relative downwards transition rates in table 5.4. In order to find the relative intensities observed for each branch, we must sum the number of photons observed for each possible transition, and for each cycle, recalculating the populations for the ground states after each cycle. We have written programs in Pascal to perform the calculations, and give here an example to illustrate the method.

Consider the Q branch, and vertical polarization. In the ground state, there are $2J + 1$ values of m, from $m = -J$ to $m = J$. Let the initial population of each of these levels be N.

The probability of a Q branch ($\Delta J = 0$) transition from lower state (J,m) to upper state (J, m) is given by

$$\frac{Am^2}{2J(J+1)} \tag{5.8}$$

J'	m'	J''	m''	
J	m	J	m	$\frac{m^2}{2J(J+1)}$
J	m	$J-1$	m	$\frac{(J+m)(J-m)(J+1)}{2J(2J+1)(2J-1)}$
J	m	$J+1$	m	$\frac{J(J+m+1)(J-m+1)}{2(2J+1)(J+1)(2J+3)}$
J	m	J	$m-1$	$\frac{(J-m+1)(J+m)}{4J(J+1)}$
J	m	J	$m+1$	$\frac{(J-m)(J+m+1)}{4J(J+1)}$
J	m	$J-1$	$m-1$	$\frac{(J+m-1)(J+m)(J+1)}{4J(2J+1)(2J-1)}$
J	m	$J-1$	$m+1$	$\frac{(J-m-1)(J-m)(J+1)}{4J(2J+1)(2J-1)}$
J	m	$J+1$	$m-1$	$\frac{J(J-m+1)(J-m+2)}{4(2J+3)(2J+1)(J+1)}$
J	m	$J+1$	$m+1$	$\frac{J(J+m+1)(J+m+2)}{4(2J+3)(2J+1)(J+1)}$

Table 5.4: Table of relative transition rates for emission

where A is a constant containing the electronic and vibrational parts of the transition probability.

The population of the upper states will then be given by

$$\frac{ANm^2}{2J(J+1)} \tag{5.9}$$

Spontaneous emission can now occur to all lower states with $J = 0, \pm 1$, $m = 0 \pm 1$, however, not all the emitted photons will be detected. The number of photons detected in this cycle will be

$$\sum_{m=-J}^{J} \frac{ANm^2}{2J(J+1)} P(J,m) \tag{5.10}$$

where $P(J,m)$ is the total number of photons emitted in the direction of the detector per molecule in the state (J,m),

$$\begin{aligned} P(J,m) \;= D_{v,0} &\left[\tfrac{m^2}{2J(J+1)} + \tfrac{(J+m)(J-m)(J+1)}{2J(2J+1)(2J-1)} + \tfrac{J(J+m+1)(J-m+1)}{2(2J+1)(J+1)(2J+3)}\right] \\ &+ D_{v,1}\left[\tfrac{(J-m+1)(J+m)}{4J(J+1)} + \tfrac{(J-m)(J+m+1)}{4J(J+1)}\right. \\ &+ \tfrac{(J+m-1)(J+m)(J+1)}{4J(2J+1)(2J-1)} + \tfrac{(J-m-1)(J-m)(J+1)}{4J(2J+1)(2J-1)} \\ &\left. + \tfrac{J(J-m+1)(J-m+2)}{4(2J+3)(2J+1)(J+1)} + \tfrac{J(J+m+1)(J+m+2)}{4(2J+3)(2J+1)(J+1)}\right] \end{aligned} \tag{5.11}$$

which simplifies to

$$P(J,m) = D_{v,0}\left(\frac{J^2 + 2J^3 + J^4 - 3m^2 + Jm^2 + J^2m^2}{J(J+1)(2J-1)(2J+3}\right) \tag{5.12}$$

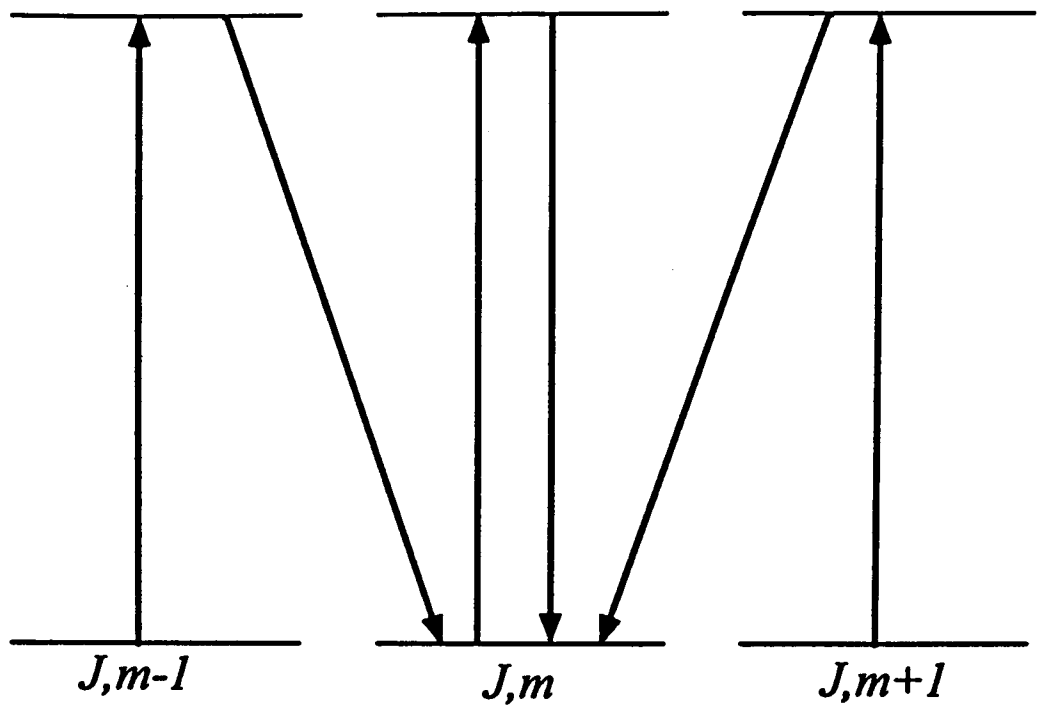

Figure 5.5: Transitions which take population from and return population to a state (J, m).

$$+D_{v,1}\left(\frac{3J^4+6J^3-3J+3m^2-Jm^2-J^2m^2}{J(J+1)(2J-1)(2J+3)}\right) \tag{5.13}$$

In order to consider the next cycle, we need to know the new populations of the ground (J, m) states. The transitions which return molecules to the ground state (J, m) are shown in figure 5.5. Hence the new population is given by

$$\begin{aligned} N_{m,new} = N_m - \frac{AN_m m^2}{2J(J+1)} + \frac{AN_m m^2}{2J(J+1)}\frac{m^2}{2J(J+1)} \\ + \frac{AN_{m+1}(m+1)^2}{2J(J+1)}\frac{(J-m)(J+m+1)}{4J(J+1)} \\ + \frac{AN_{m-1}(m-1)^2}{2J(J+1)}\frac{(J-m+1)(J+m)}{4J(J+1)} \end{aligned} \tag{5.14}$$

A new excitation cycle now begins, using these new populations. The number of photons emitted and the resultant populations are calculated for the new cycle. By using the computer program "QBRANCH.PAS", the total number of photons emitted over a large number of cycles can be calculated.

Applying the same arguments to the P and R branches, we can similarly find the total number of photons emitted for each branch as a function of J. Figure 5.6 shows the number of photons emitted towards the detector as a function of J for each branch, divided by the number expected from the Honl-London factors, for horizontal and vertical polarisations. The exact form of these graphs is dependent on A and

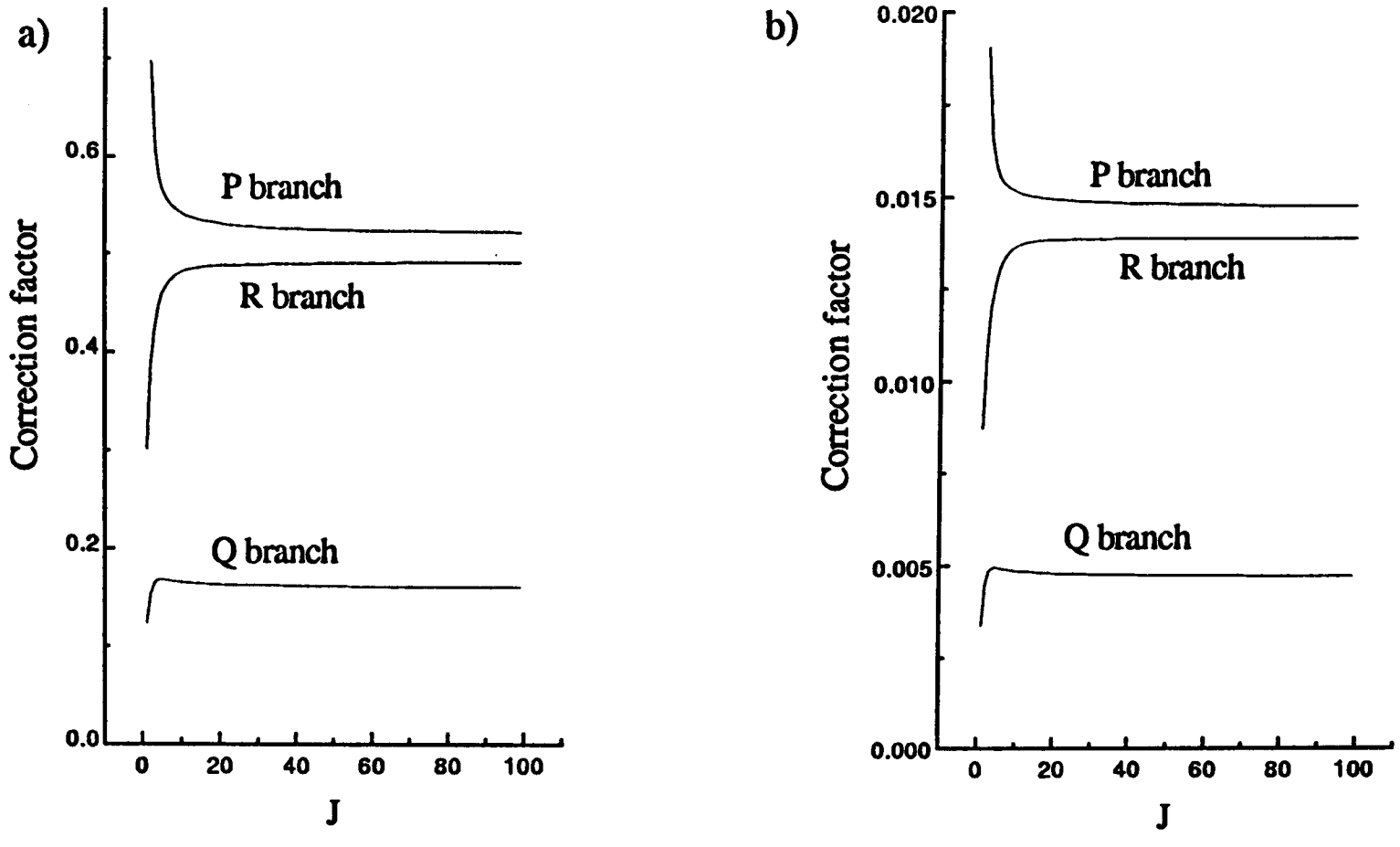

Figure 5.6: Corrections to Honl-London factors for a) horizontal polarization and b) vertical polarization.

the number of iterations, but the curves shown for $A = 0.1$ with 100 iterations are typical.

It turns out that the "correction factors" to the Honl-London factors are almost constant with J for $J > 10$, with different constant values for the three branches. However, the values of these constants depend on the the number of iterations, which varies with the velocity of the molecules and the transition rate; and the value of A, which depends on the laser intensity and the transition probability. Since it would be difficult to measure such quantities directly from our experimental setup, we have introduced the correction factors into our intensity model by assuming that the intensity of each branch should be multiplied by a constant factor, which is found empirically during the fitting. In this way, we obtain the fits shown in figure 5.7.

So in order to model line intensities correctly, we need four parameters: the rotational temperature T_{rot}, the relative scaling factors for the P and R branches ($PFac$ and $RFac$) and an overall scaling factor I.

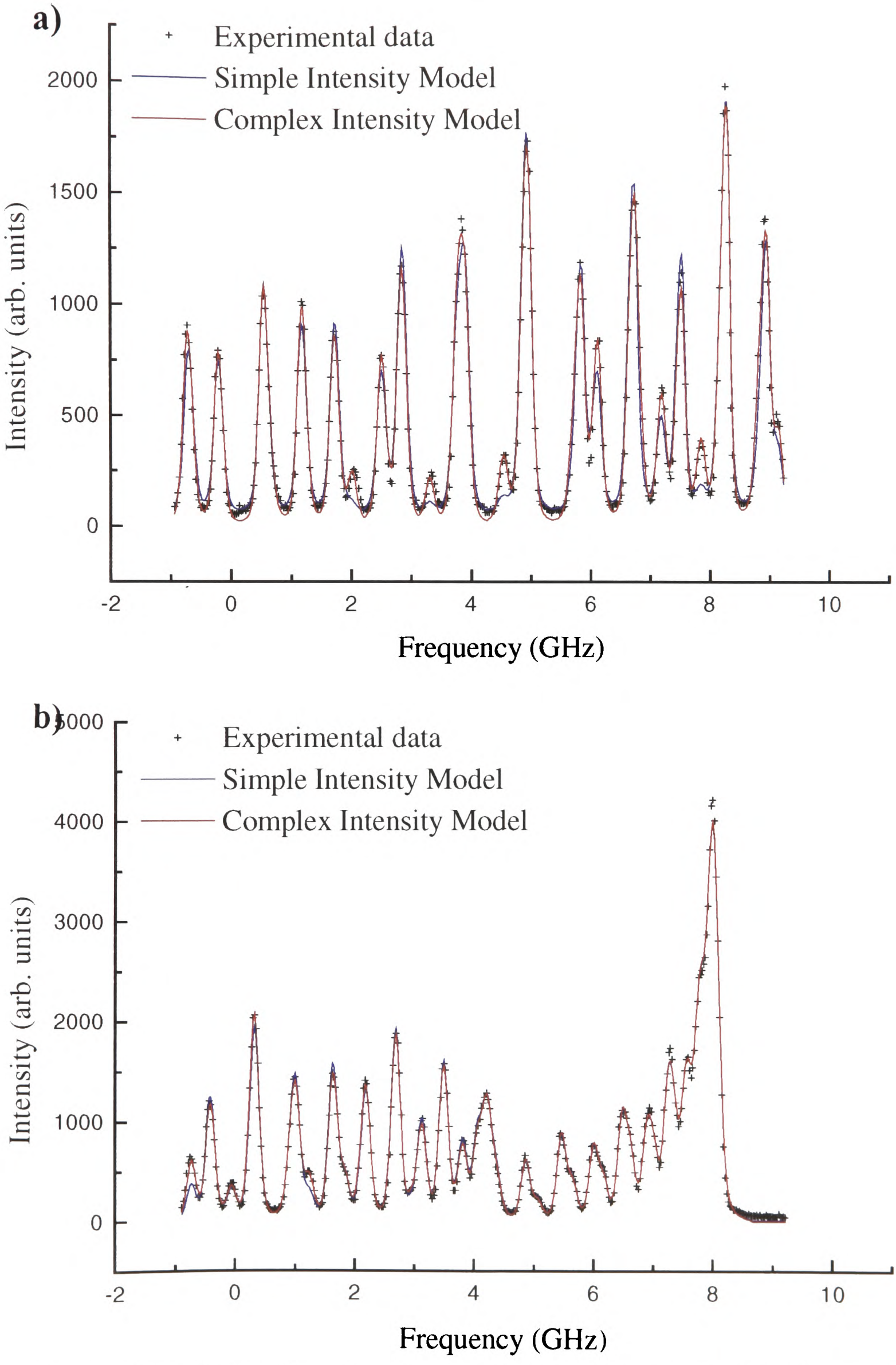

Figure 5.7: Fitted profiles using simple and complex models for intensities for a) section of the middle of the band and b) the bandhead region.

Line shapes

To obtain the theoretical profile from the line positions and intensities, we must add include a line profile at each position, and by adding the contribution from each line, find the intensity at each frequency. The two simplest line shapes to try are the Gaussian and the Lorentzian.

A Gaussian line shape normally arises from Doppler broadening of the spectral lines. This will not be the case in the present experiment because the velocity spread is so small; the frequency shifts come about primarily because of the different directions of the molecules emerging from the nozzle. However, the Gaussian is a good enough approximation to the profile expected for this mechanism, and has the virtue of simplicity. As we have taken steps to reduce the observed Doppler width by using perpendicular laser and molecular beams and a narrow slit, we would expect the Doppler width to be reduced as discussed in section 4.9.3.

A Lorentzian line shape can arise from the natural linewidth of the transition, or from collisions with other atoms [61]. By using a supersonic expansion we hope to have reduced the collisions both between molecules and atoms in the beam, and with background gas. The Lorentzian differs from the Gaussian in having large wings, which did in fact characterise our experimental profile.

However, neither the Gaussian or Lorentzian alone proved satisfactory. We then considered whether the line shape was due to both Doppler and collisional broadening occurring together. This can be taken into account by using a Voigt profile: a convolution of a Lorentzian and a Gaussian profile. However, the Voigt profile did not reproduce the experimental data either. In fact, the level of collisional broadening is so small that effects $\sim$100MHz would not be expected in any case.

We found that the best fits were obtained if the line shape was taken as a *sum* of a Gaussian and a Lorentzian of different widths. We believe that the additional Lorentzian contribution is due to the Doppler shift caused by atoms which have been deflected into the imaged region following a collision; the collision process leads to a wider spread of velocities and directions, and so this contribution has a greater line width (figure 5.8). It is clearly not rigorously Lorentzian, but the exact shape is not critical.

The resulting line profile is a sum of the two contributions, rather than a convolution, because different atoms contribute to each profile.

The line profile therefore requires a further four parameters, a background, a

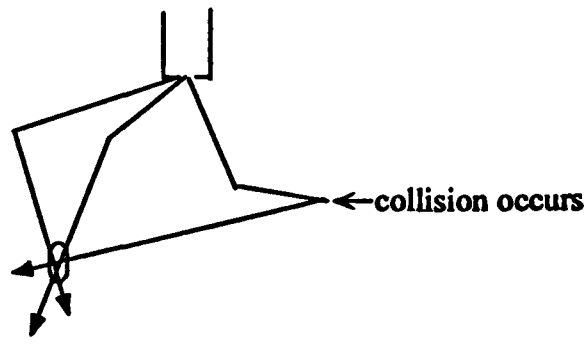

Figure 5.8: The origin of the Lorentzian component of the line profile : atoms are deflected into the imaged region by collisions, leading to a wide spread of velocities.

Gaussian linewidth, a Lorentzian linewidth and the relative height of the two line shapes.

This gives a total of 13 parameters to be found during the fitting. The least squares fitting routine can only fit such a large number of parameters well if good initial guesses are made for each of the parameters. Because of this we proceeded in several stages before fitting all 13 parameters at the same time.

- Our initial values for the rotational constants were those taken from [29] and [25].
- The initial value for the background was estimated from the intensity to the right of the band head, where there is no molecular signal.
- The Gaussian line width was estimated from the FWHM of one of the single lines towards the left of the band.
- The P and R branch scaling factors were initially estimated to be 1.
- We then calculated the theoretical profile, adjusting the other parameters manually (i.e. not using the computerised fitting routine), using a single scan over the bandhead, until a good agreement between theory and experiment was obtained 'by eye'.
- We then used the fitting routine to optimise the parameters, for the single scan over the bandhead.
- We used these resulting parameters, changing only the frequency offset, as the inputs for fitting the other three single scans covering the band.

		a)	b)
Background	(arb. units)	1.625e-7	-3.2519e-6
Intensity Scaling		439235	348823
Ratio of Lorentzian to Gaussian peak heights		0.947	0.730
Offset	GHz	29.1148	29.121
Temperature	K	11.1	9.13
P branch scaling		2.39	1.90
R branch scaling		1.52	1.62
Gaussian Linewidth	GHz	0.230	0.238
Lorentzian Linewidth	GHz	1.002	1.076
B_v Lower Level	cm^{-1}	1.1704×10^{-2}	1.1706×10^{-2}
D_v Lower Level	cm^{-1}	2.304×10^{-9}	2.409×10^{-9}
B_v Upper Level	cm^{-1}	1.0671×10^{-2}	1.0673×10^{-2}
D_v Upper Level	cm^{-1}	2.780×10^{-9}	2.852×10^{-9}

Table 5.5: Parameters calculated from fitting the two parts of the singlet band.

- Using the background, intensity and offset parameters from the fits, we joined together pairs of consecutive scans.

- We performed a series of fits on these combined spectra in which the B_v were adjusted manually, and the other parameters were fitted automatically. This was to check that we had found the true best values of B_v, and not some subsidiary minimum in the fitting; and to make an estimate of the errors in the values of the rotational constants.

We then performed one final fit on each of the two halves of the band, using the best values so far as the inputs. In this way we obtained the fitted spectra shown in figure 5.9, and the parameters given in table 5.5.

The rotational constants deduced in this work are

$$x^1\Sigma_g^+ : \quad B_v = 1.1705 \times 10^{-2}\text{cm}^{-1} \tag{5.15}$$

$$D_v = 2.357 \times 10^{-9}\text{cm}^{-1} \tag{5.16}$$

$$B^1\Pi_u : \quad B_v = 1.0672 \times 10^{-2}\text{cm}^{-1} \tag{5.17}$$

$$D_v = 2.816 \times 10^{-9}\text{cm}^{-1} \tag{5.18}$$

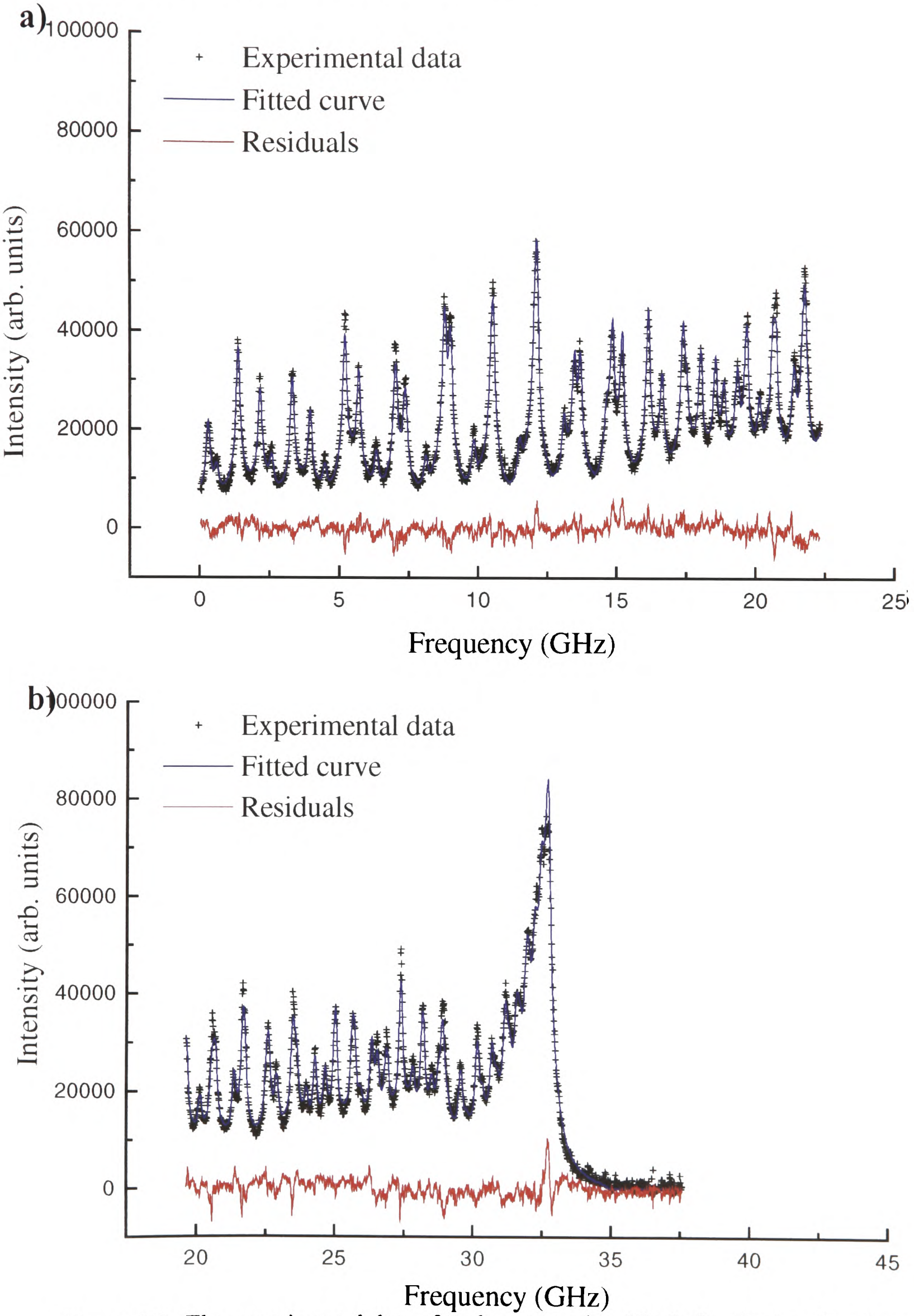

Figure 5.9: The experimental data, fitted curve and residuals for the two fitted sections of the singlet band a) and b), corresponding to the parameters of table 5.5.

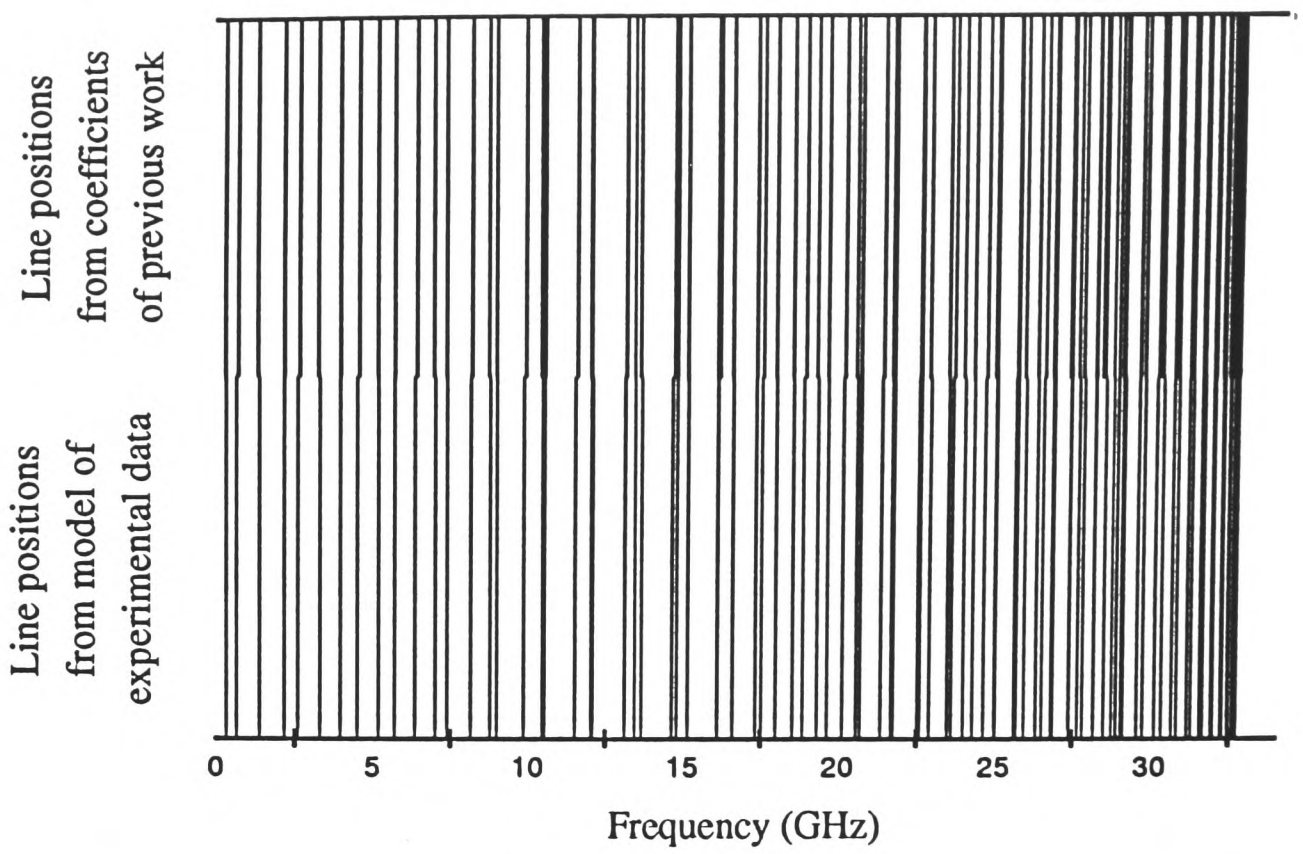

Figure 5.10: Calculated line positions from this work and from refs [25, 29]

while those deduced from [29, 25] are

$$x^1\Sigma_g^+: \quad B_v = 1.17312 \times 10^{-2}\text{cm}^{-1} \tag{5.19}$$

$$D_v = 3.709 \times 10^{-9}\text{cm}^{-1} \tag{5.20}$$

$$B^1\Pi_u: \quad B_v = 1.0700 \times 10^{-2}\text{cm}^{-1} \tag{5.21}$$

$$D_v = 4.179 \times 10^{-9}\text{cm}^{-1} \tag{5.22}$$

Our values for the B_v's are in fairly good agreement with those calculated from the previous work. However, the fit is relatively insensitive to the absolute values of B_v, only to the difference between them. Hence the discrepancy could well be due to the inadequacies of the fit. There is a greater discrepancy between our D_v values and those calculated from the previous work. The D_v values varied widely depending on the exact details of the fit, and so these values have little significance.

A better test of the similarity of our spectra with the previous work is to compare the line positions derived from our spectra with those calculated using the Dunham coefficients of [29, 25]. Figure 5.10 shows the two sets of line positions. Our line positions are very close to those derived from the previous work. When the offset is chosen to match the line positions at the band head, the maximum discrepancy between corresponding lines within the range of the experimental data is 55MHz. This clearly shows the good agreement between our measurements of the $v' = 3 \leftarrow v'' = 0$

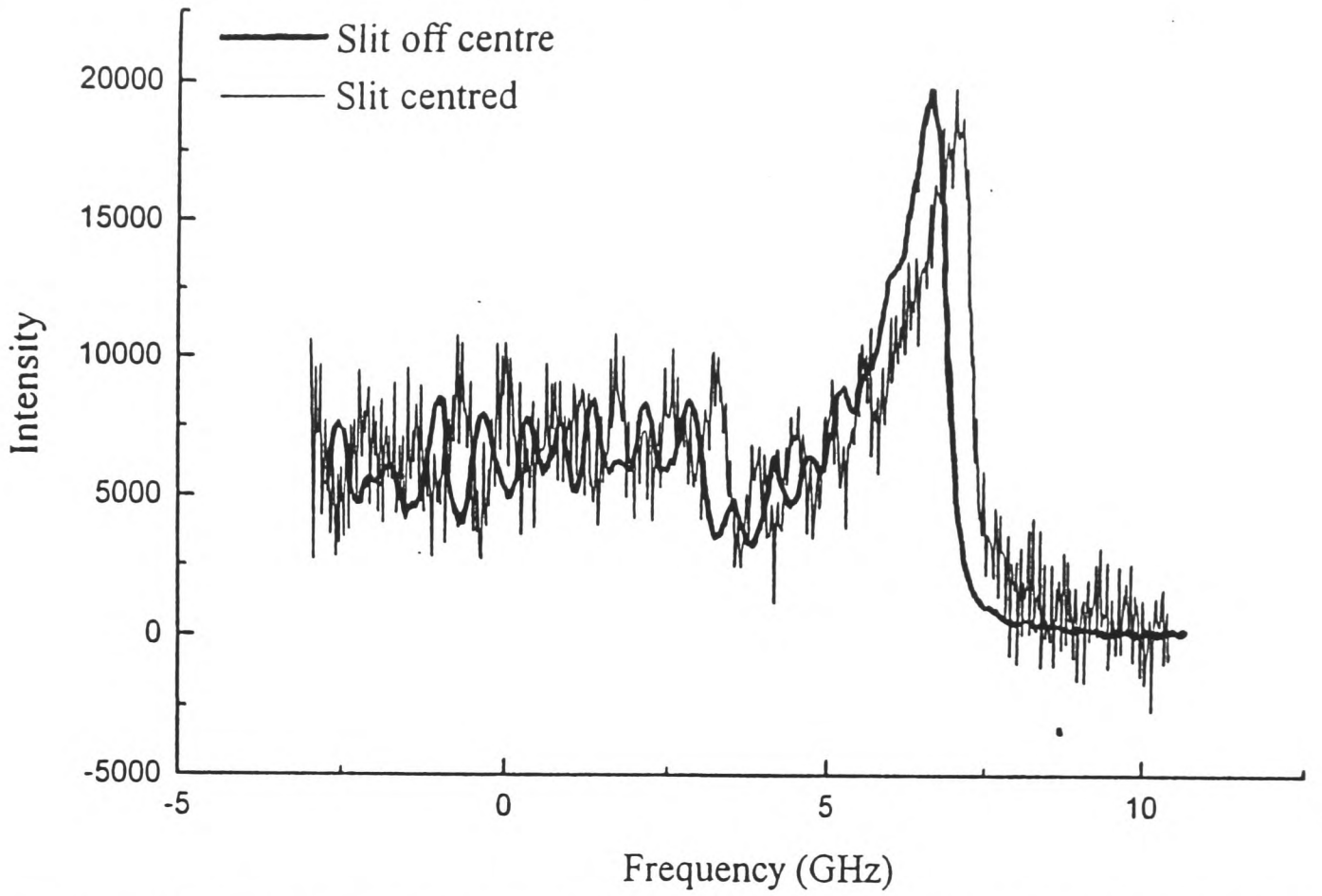

Figure 5.11: Singlet spectra taken with slit centred and slit off centre, showing Doppler shift.

band and the previous data on this band. Since our results for this sample band agree with the previous work, we did not study any of the other bands in this detail, but moved on to study the triplet spectra. It is interesting to note that although there is a close agreement in line positions, the derived parameters, in particular the D_v values, diverge widely. This could be due to errors introduced by using a finite number of terms in the Dunham expansion; even if the line positions are the same, the values of the fitted coefficients will vary depending on how many terms are used.

Line width and shift

The Gaussian Doppler width of 234MHz found in our fits is substantially larger than the Doppler width of 50MHz estimated for these conditions in section 4.9.3. In making our estimate of the Doppler width, we assumed that the nozzle was a point source. In fact, the nozzle has a diameter of 0.25mm, which will increase the spread of angles at which the molecules are travelling, and so will increase the Doppler width. Collisions in the vicinity of the nozzle further increase the effective size. The width may also be increased by lens aberrations, and by any error in focussing the interaction region onto the slit.

To find the shift in line positions, we compared spectra taken with a 1mm wide

slit imaging the region directly below the nozzle, and with the slit imaging to one side, at a nozzle height of 5mm. Figure 5.11 shows the two spectra, which have been accurately superposed on the same absolute frequency scale by fitting a Gaussian curve to the same iodine bromide feature on each spectrum, and ensuring that the peak is at the same frequency.

We found the difference in frequencies between the bandheads on the two spectra, and calculated the Doppler shift to be 430MHz. This is of the same order of magnitude as the shift estimated in section 4.9.3 of 770MHz. The discrepancy is likely to be due to the discrepancy in finding the distances used in the calculation, as we have no way of measuring them directly; our values are crude estimates based on the CCD camera pictures.

5.4 Triplet spectra

Although the singlet spectra provide a good test of our apparatus and techniques, the aim of this work is to study the triplet spectra. After studying the singlet spectra we were able to make our first observations of the triplet spectra.

5.4.1 Observations made with broadband laser

Before we could make a detailed study of the triplet spectra, it was necessary to locate the vibrational bands. Because of the discrepancy between the two previously measured sets of band positions[28, 26], it was not clear over which wavelength region we should scan; scanning over wide wavelength ranges takes a long time which is unacceptable given the limited quantity of caesium used. For these reasons we were initially unable to find any triplet spectra using the dye laser running single-mode.

We then removed the etalon assembly and Brewster plate from the laser cavity, and ran it broadband with only the BRF for tuning. When running in this way, the laser can be tuned manually using the BRF micrometer drive over a wide wavelength range in a short time. As the laser is tuned by hand, the wavelength can not be made to vary even approximately linearly with time, and so no spectra can be taken using the computer. However, the fluorescence from the molecules when the laser is in resonance with a transition can be observed using the CCD camera. A ' flash' is seen as the laser is tuned over a transition, as shown in figure 5.12. The laser can then be tuned to sit on the transition, and the wavenumber of the transition read

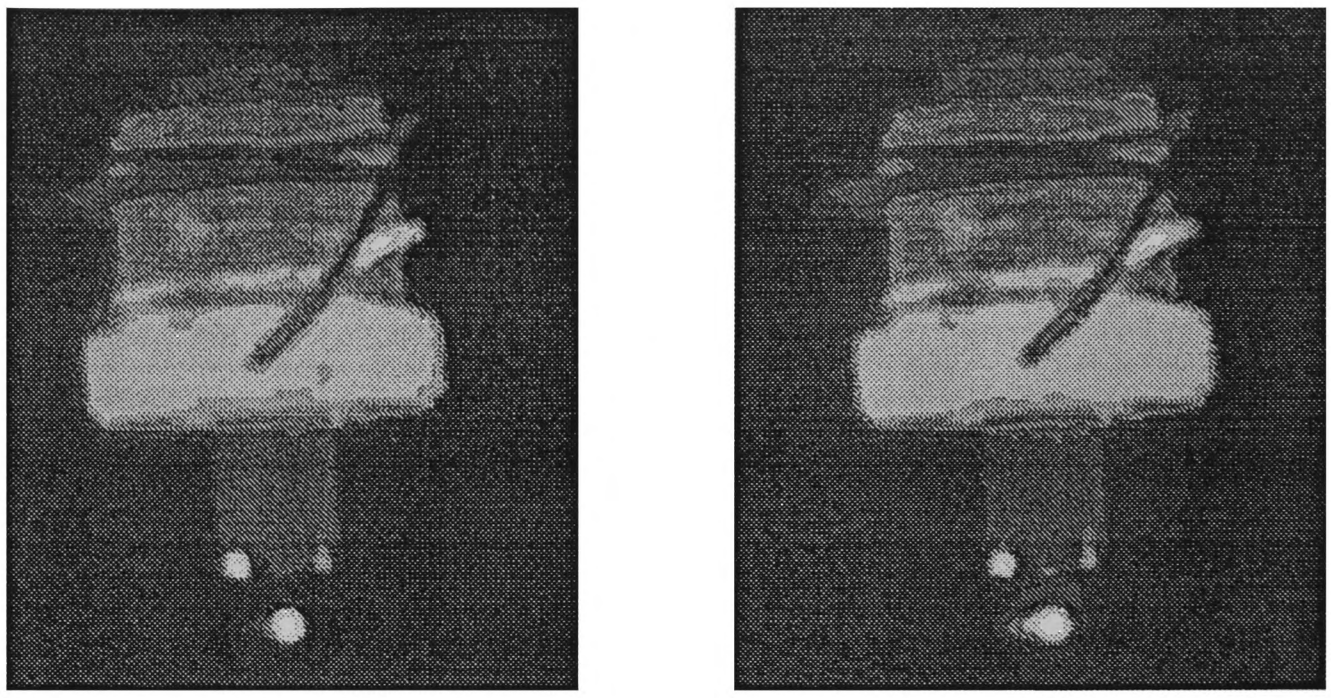

Figure 5.12: CCD camera image when the broadband laser is off resonance (left) and on resonance (right). The fluorescence appears to the left of the bright blob.

from the wavemeter. This technique is obviously less accurate than scanning using a single mode laser, but it does enable us to locate the transitions to enable a more detailed study.

Using this technique, we were able to observe 7 vibrational bands, at the wavenumbers given in table 5.6. We compared these values with those found by Diemer et al. [28], and those given by Kim and Yoshihara [26], as shown in table 5.6.

For 6 of the bands, our line positions are close to those given by Kim and Yoshihara [26]. There is no line position close to that we observed at 14130.5cm^{-1}; however, from the hot band of the $\Omega = 1$ state, it can be deduced that there would be a hot band $\Omega = 2, v'' = 1, v' = 1$ at 14130.39cm^{-1}. We do not agree with the band positions found by Diemer et al. [28]. We also note that the closest bands from [28] to those in this work are hot bands; we would be very surprised if we could see bands from $v'' = 1$ but not $v'' = 0$. Kim and Yoshihara [26] suggest that the peak positions given by Diemer et al. [28] have been misassigned. However, the intensities of the bands as shown in the spectra presented in [28] would seem to be consistent with the assignment given, and so it seems more likely that there is a systematic error of 15-20cm^{-1} in the values given by Diemer et al. [28]. We were then able to use the laser in its single mode configuration to scan over the vibrational bands, using the

This work	Nearest band in [26]	Assignment of [26]	Nearest band in [28]	Assignment of [28]
14124.5	14124.21	$\Omega = 2, v'' = 0, v' = 0$	14134	$\Omega = 2, v'' = 1, v' = 0$
14016.6	14016.36	$\Omega = 1, v'' = 0, v' = 0$	14026	$\Omega = 1, v'' = 1, v' = 0$
13916.6	13916.39	$\Omega = 0^+, v'' = 0, v' = 0$	13916	$\Omega = 0^-, v'' = 1, v' = 0$
13912.9	13912.88	$\Omega = 0^-, v'' = 0, v' = 0$	13916	$\Omega = 0^-, v'' = 1, v' = 0$
19934.5	13934.38	$\Omega = 0^+, v'' = 0, v' = 1$	13936	$\Omega = 0^-, v'' = 1, v' = 0$
14033.9	14033.72	$\Omega = 1, v'' = 0, v' = 1$	14033	$\Omega = 1, v'' = 2, v' = 1$
14130.5	-	-	14134	$\Omega = 2, v'' = 1, v' = 0$

Table 5.6: Frequencies of triplet vibrational bands, using broadband laser (all $\pm 0.3 \text{cm}^{-1}$)

broadband values and those of Kim and Yoshihara as a guide.

5.4.2 High resolution spectra of triplet bands

When optimising the triplet spectra at the beginning of each run, we used the $2^3\Pi_g(\Omega = 2) \leftarrow x^3\Sigma_u\ v' = 0 \leftarrow v'' = 0$ band at 14124cm^{-1} as this was the strongest band we observed. The methods for optimisation were as discussed in section 4.9. Our optimised conditions were a slit width of 1mm positioned off centre, a nozzle height of 5mm, a temperature of 320°C and a pressure of 1.2 atm. We then took our final scans for each band. Each band required several laser scans. We took at least two scans at each wavelength to check that the features were reproducible. We made sure that there was sufficient overlap between adjacent bands to patch them together as described above to give a spectrum of the band. We were able to observe ten bands in total. We also searched for the $\Omega = 2, v'' = 0, v' = 1$ and $\Omega = 2, v'' = 2, v' = 2$ bands without success.

We used the techniques described at the beginning of this chapter to combine adjacent scans, and the resulting spectra of the bands are shown in figures 5.13, 5.14, 5.15, 5.16 and 5.17.

The spectra of vibrational bands with the same v'' and Ω show very similar features. There are certain features which are similar for many of the bands: there is a rounded peak of $\sim 0.2 \text{cm}^{-1}$ at the left of many of the scans, with a sharper peak immediately to the right. We believe that these are the P and Q branch respectively,

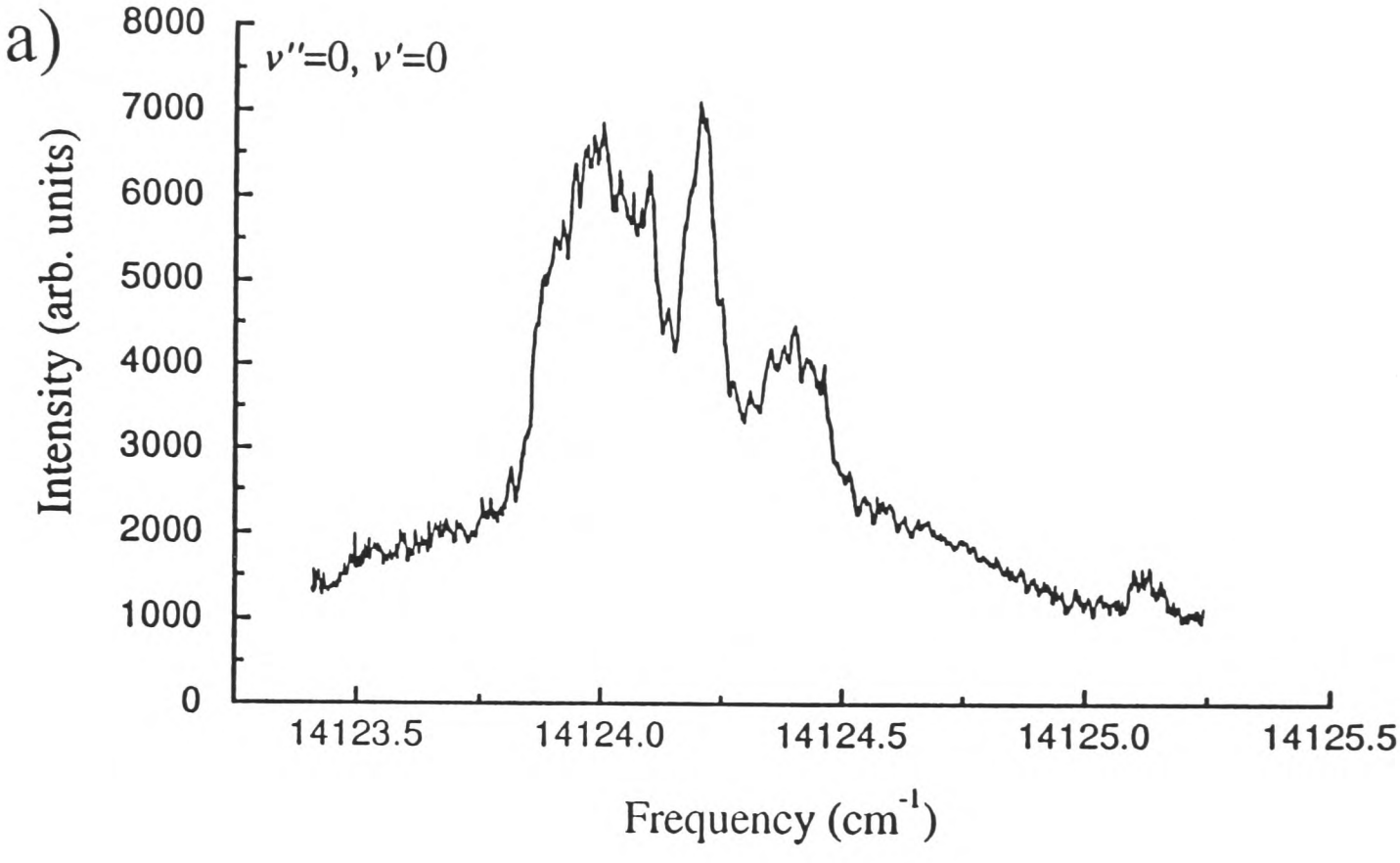

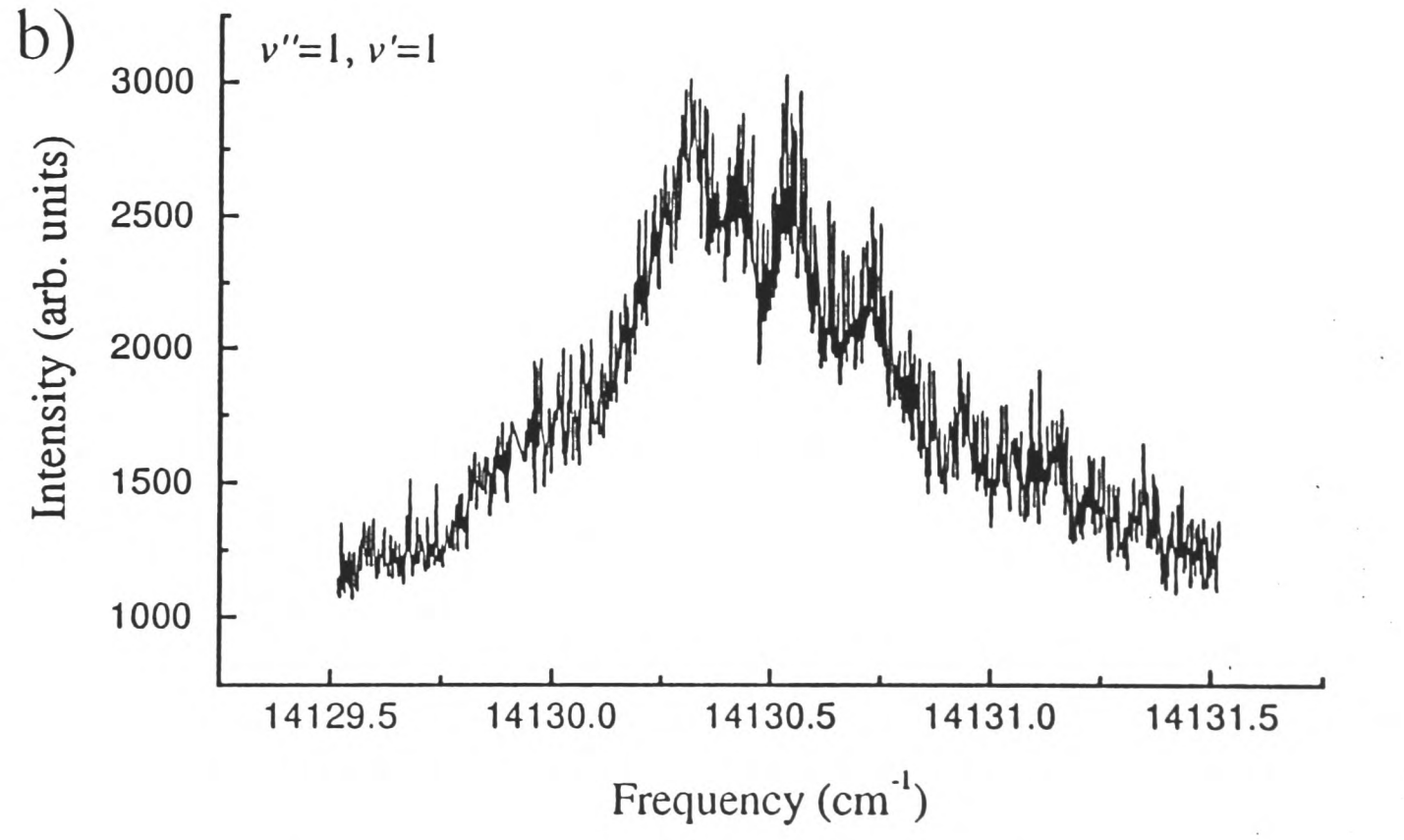

Figure 5.13: The observed $\Omega = 2$ triplet bands.

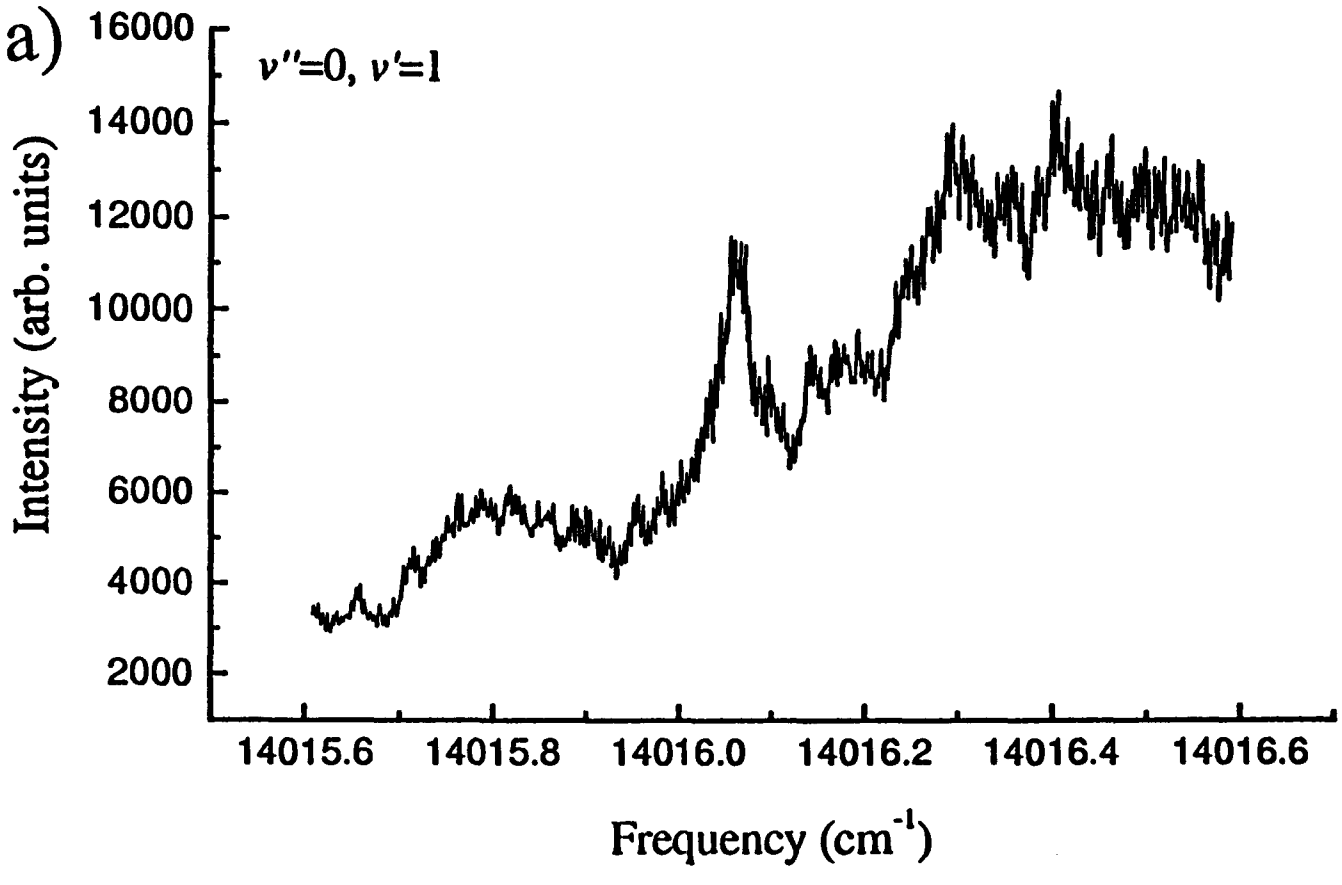

Figure 5.14: The observed $\Omega = 1$, $v'' = 0$ triplet bands.

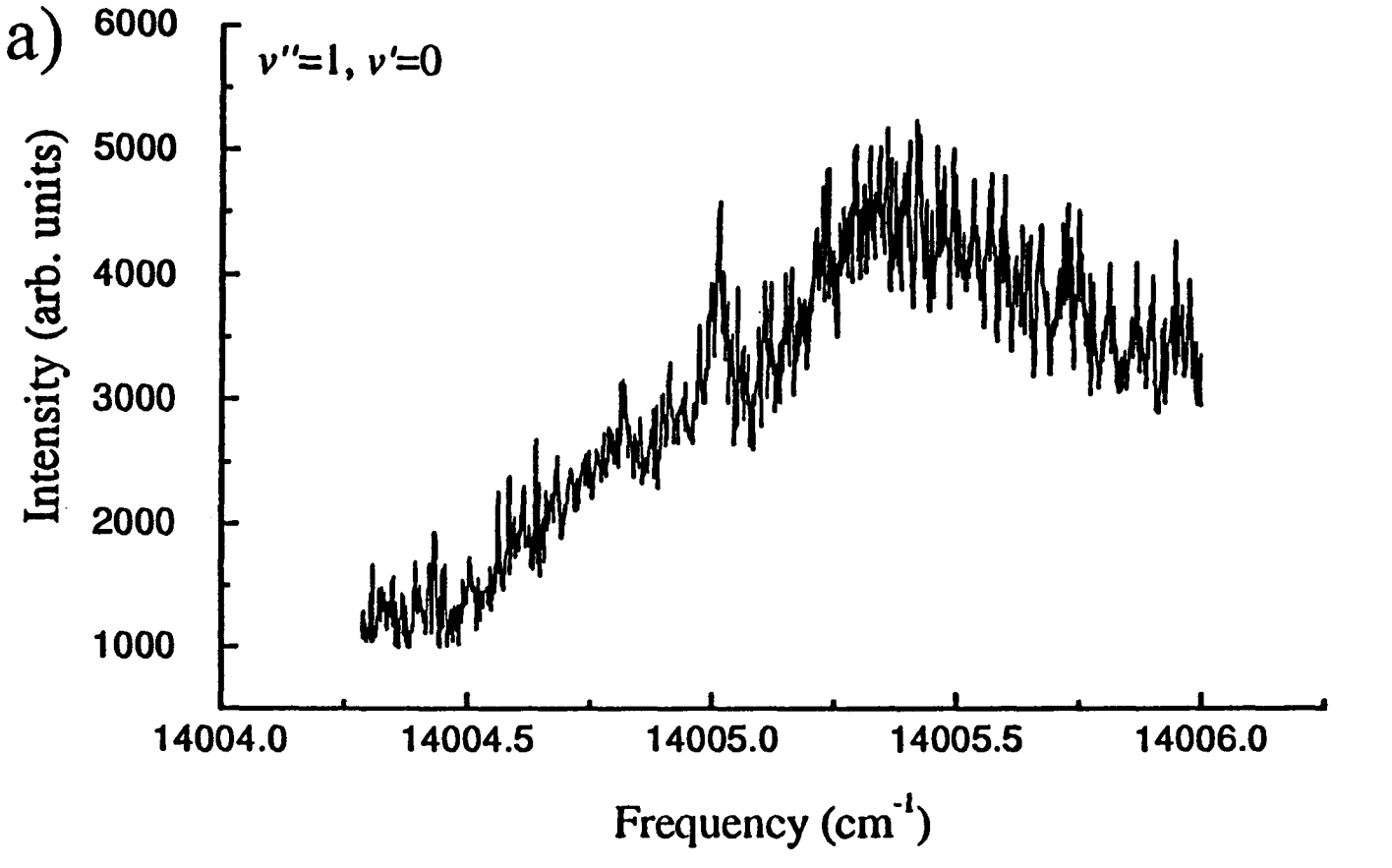

Figure 5.15: The observed $\Omega = 1$, $v'' = 1$ triplet bands.

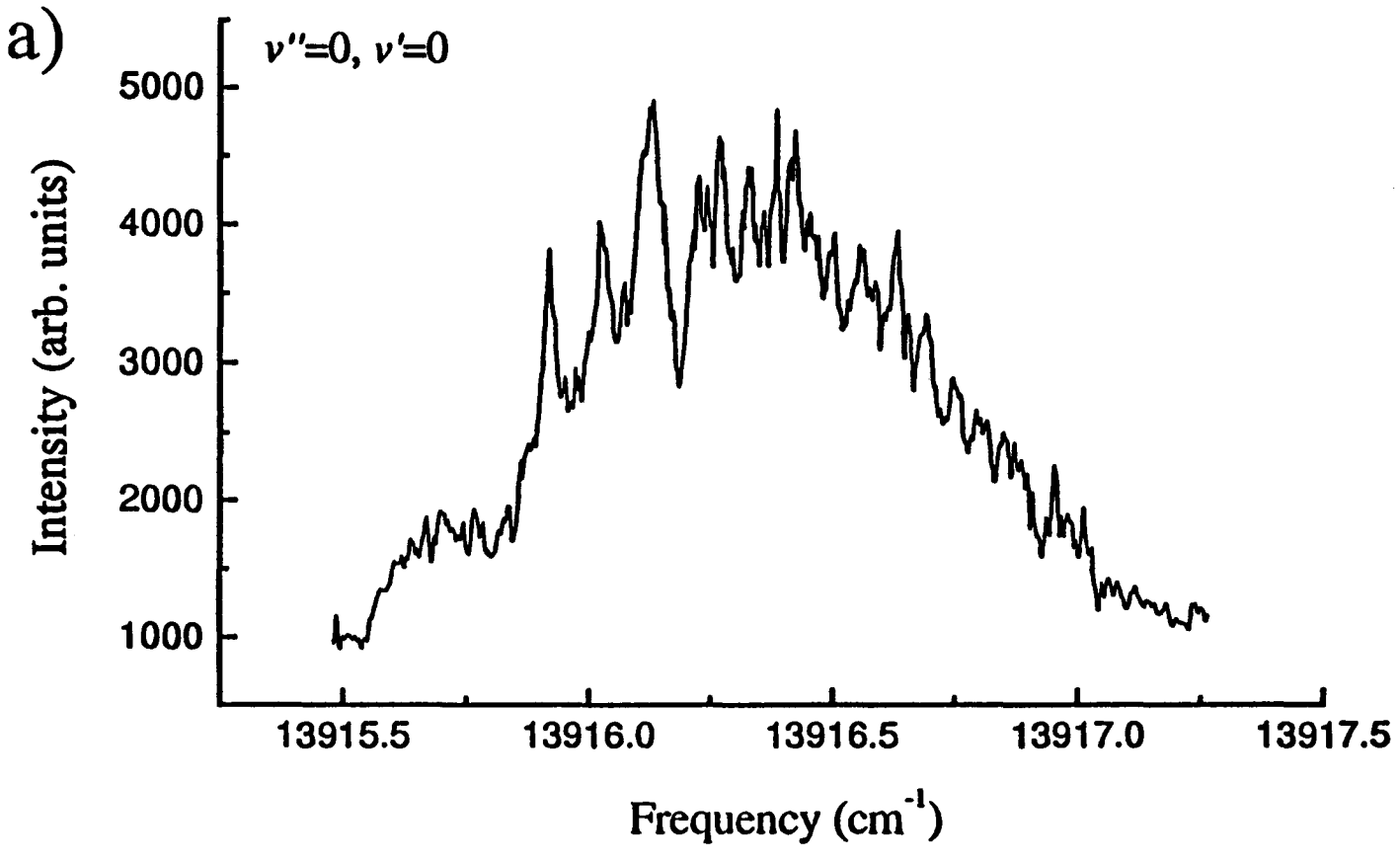

Figure 5.16: The observed $\Omega = 0^+$ triplet bands.

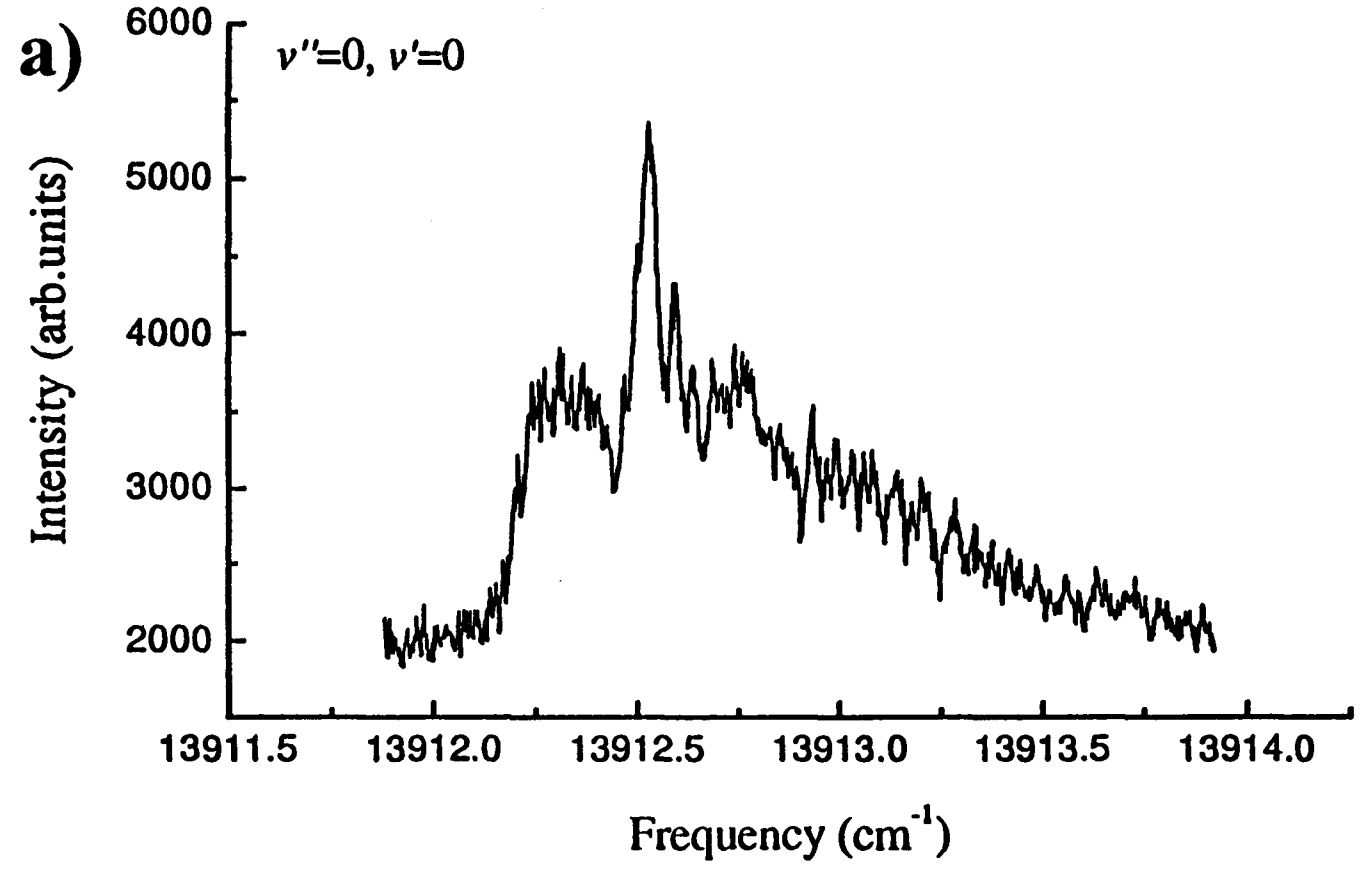

Figure 5.17: The observed $\Omega = 0^-$ triplet bands.

Ω	v''	v'	Peak of band (cm^{-1})	Q branch (cm^{-1})	Ref [26] (cm^{-1})
2	0	0	14124.20	14124.20	14124.21
2	1	1	14130.32	14130.55	14130.39[1]
1	0	0	14016.40	14016.06	14016.36
1	0	1	14033.81	14033.47	14033.72
1	1	0	14005.36	14005.01	14005.23[1]
1	1	1	14022.15	14022.45	14022.59
0^+	0	0	13916.12	13916.12	13916.39
0^+	0	1	13934.09	13934.09	13934.38
0^-	0	0	13912.52	13912.52	13912.88
0^-	0	1	13930.63	13930.63	13930.81

Table 5.7: Triplet band positions found in this work, and from the previous work by Kim and Yoshihara [26].

while the region to the right of the sharp peak corresponds to the R branch. We notice that the greatest intensity within a band does not necessarily correspond to the Q-branch; for $\Omega = 2$, the greatest intensities occur in the P branch, while for $\Omega = 1$ the greatest intensities are in what we believe is the R branch. This may be partially due to the slightly different conditions under which spectra were taken.

For each band, we found the frequency corresponding to the peak of the feature that we judged to be the Q branch, and the frequency at which the greatest intensity occurs. These frequencies are given in table 5.7, together with the corresponding frequencies given by Kim and Yoshihara [26]. The error in each frequency, taking into account the error in calibration using the I_2 spectra (200MHz), the difficulty of judging the peak of each band (300MHz) and the Doppler shift introduced by using an off-centre slit (500MHz) , is estimated to be 1GHz or $0.03cm^{-1}$.

From our Q branch positions, we have calculated the wavenumber differences between $v'' = 0$ and $v' = 0$ for both the ground and excited states (table 5.8), and we have constructed an energy level diagram of the states studied (figure 5.18).

[1] While these bands were not observed directly in [25], their positions have been deduced from other observed bands.

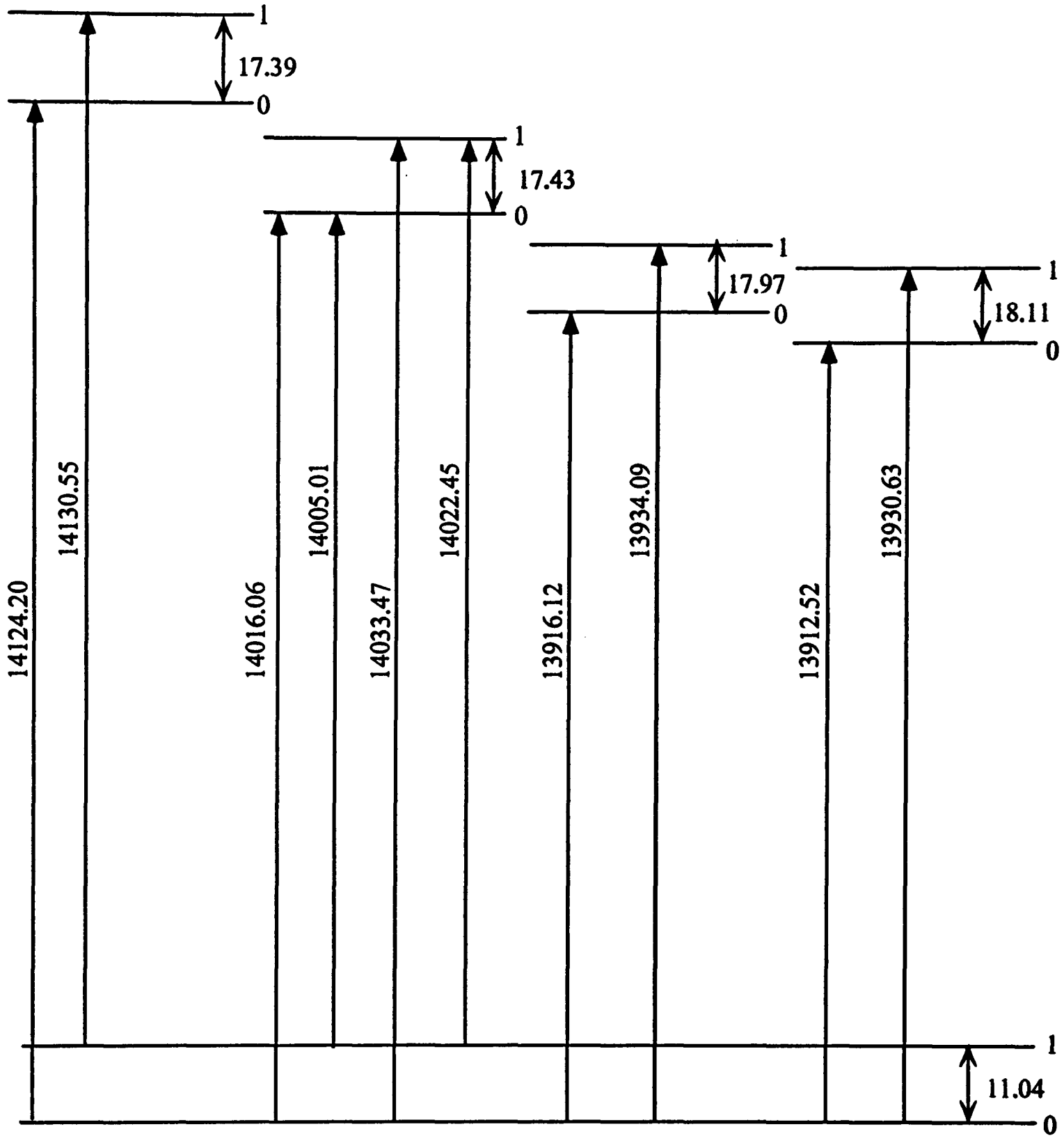

Figure 5.18: Energy level diagram of the triplet states studied in this work (not to scale).

Electronic state	This work	Ref [26](exp.)	Ref [27](theory)
$x^3\Sigma_u$	11.04	11.05	11.2
$(2)^3\Pi_g : 2_g$	17.39	17.31	17.9
1_g	17.43	17.36	18.1
0_g^+	17.97	17.99	18.9
0_g^-	18.11	17.94	18.8

Table 5.8: Wavenumber differences between $v'' = 0$ and $v' = 0$ bands for triplet ground and excited states.

5.4.3 Comparison of line positions from this work with previous work

As can be seen from table 5.7, our peak positions for the $\Omega = 2$ and $\Omega = 1$, $v'' = 0$ bands agree with the positions given by Kim and Yoshihara [26] to within 0.1cm^{-1}, a discrepancy which can be accounted for by our experimental error which is estimated to be 0.03cm^{-1}, and the quoted error of 0.06cm^{-1} given in [26]. We note that in the $\Omega = 1, v'' = 0, v' = 1$ band around 14033cm^{-1}, even better agreement is obtained if we consider the *second highest* peak in our data, at 14033.70cm^{-1}. For the $\Omega = 1$, $v'' = 1$ band, there are discrepancies of 0.13 and 0.14cm^{-1}, in opposite directions. The spectra of these bands have considerable noise, and so we would expect a greater experimental error in determining the peak positions. In the $\Omega = 0$ bands, our peak positions are consistently at lower wavenumber than those from [26], by between 0.18cm^{-1} and 0.36cm^{-1}. This could be because the different experimental conditions used by Kim and Yoshihara [26] (T_{rot}=1K, while we estimate T_{rot}=10K) give an intensity distribution which is sufficiently different to explain the discrepancy in the peak positions.

Our *differences* between vibrational states, which are approximately equal to the vibrational constants, are in better agreement with those of Kim and Yoshihara, since we do not need to correctly identify the peak of the band, but only to be consistent in the feature (here, the Q branch) which we have measured for each band. Our value of 11.04cm^{-1} for the separation of the $v'' = 0$ and $v'' = 1$ states is in reasonable agreement with the theoretical results of Spiess [27] (11.2cm^{-1}) and Foucrault et al. [23] (11.18cm^{-1}).

Background	(arb. units)	1000
Intensity Scaling		4225
Ratio of Lorentzian to Gaussian peak heights		0.935
Offset	cm^{-1}	14124.18
Temperature	K	3.9
P branch scaling		7.42
R branch scaling		3.73
Gaussian Linewidth	GHz	0.353
Lorentzian Linewidth	GHz	1.120
B_v Lower Level	cm^{-1}	6.075×10^{-3}
B_v Upper Level	cm^{-1}	6.141×10^{-3}

Table 5.9: Parameters found in fitting to the triplet $\Omega = 2, v'' = 0, v' = 0$ band.

5.4.4 Theoretical modelling of triplet bands

As in the case of the singlets, we wish to find the vibrational and rotational constants for the triplet bands. As for the singlets, the best way to achieve this is to develop a theoretical model and to fit it to the observed spectra. In the case of the triplets, we were uncertain as to which features in the spectrum corresponded to the three branches. A satisfactory model of the spectra will enable us to deduce the origin of each feature in the spectrum.

We used the final model for the singlet case to fit to the $\Omega = 2, v'' = 0, v' = 0$ triplet band. We initially used the line profile and temperature found in the singlet fits, while for the rotational constants, we used the theoretical values of Spiess [27]: $B''_e = 5.97 \times 10^{-3}\text{cm}^{-1}$, $B'_e = 6.05 \times 10^{-3}\text{cm}^{-1}$. We adjusted the other parameters "by eye" to give the best agreement between the model and the experimental spectra. We found that better agreement was obtained if we reduced the temperature from 10K, as found in the singlet case, to 4K. We would expect that the rotational temperature of the triplets would be lower, as the rotational constant of the triplet ground state is less than that for the singlet ground state [28]. We then used the fitting program to find the best values of the parameters. The resulting theoretical spectrum is shown in figure 5.19, and the values of the parameters in table 5.9.

The overall shape of the theoretical spectrum is in agreement with our experimen-

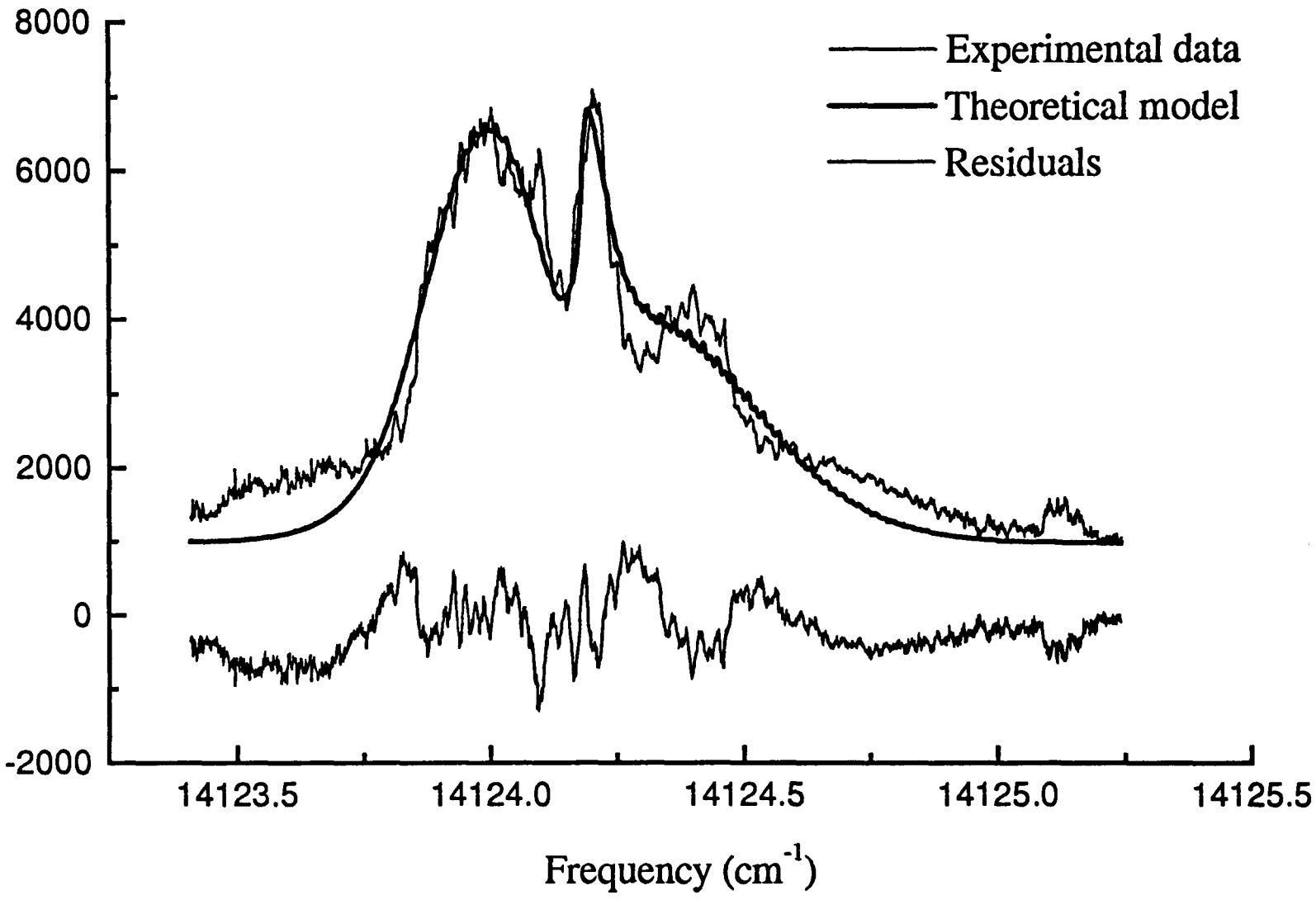

Figure 5.19: Theoretical spectrum of $\Omega = 2, v'' = 0, v' = 0$ band

tal data, and confirms that we have correctly identified the Q branch as the central sharp peak. However, the finer details of the spectrum are not adequately modelled. We found that the scaling factors for the P and R branches relative to the Q branch are larger than in the singlet case.

The model shows that the rotational constants of Spiess [27] are broadly consistent with our experimental data. Since the rotational constants could be varied by up to ~50% (with the difference between them constant) without producing a large change in the quality of fit, our values are no more than an order of magnitude estimate. Our ground state rotational constant is also in reasonable agreement with the value of $6.28\times10^{-3}\text{cm}^{-1}$ derived from the R_e of Foucrault et al. [23].

There are a number of reasons why we have not been able model the triplet spectra with the same degree of success as the singlet spectra:

- The rotational constants are smaller in the triplet case, and so we have not been able to resolve the rotational structure with our experimental arrangement. Hence we cannot unambiguously determine the rotational constants.

- Without resolved peaks, it has not been possible to determine the line profile.

- The complex model derived for singlet intensities may give a very different result in the triplet case. The triplet transition corresponds to a forbidden S to D atomic transition, and so we would expect a lower transition probability. Also, in the case of the singlets, all excited molecules must return to states within the ground state potential. In the triplet case, it is highly likely that an excited molecule will decay via an intermediate electronic state correlating to the 6P excited atomic state. These molecules may then return to the ground state. Hence there are many more transition probabilities to be calculated to derive a full model for intensities.

- We have not taken into account hyperfine structure. In the singlet $^1\Sigma$, there is no overall electronic angular momentum to lead to first-order magnetic hyperfine structure, whereas in the triplet $^3\Sigma$ state, the spin can interact with the nuclear magnetic moment. The ground state hyperfine splitting in the caesium atom is 9.2GHz, and so we might expect hyperfine structure of a similar order of magnitude in the molecule. In both cases, quadrupole hyperfine structure is small because the quadrupole moment of the caesium nucleus is only $-0.003\times10^{-24}\text{cm}^2$ [62].

It seems likely that the additional peaks observed in the triplet bands are due to hyperfine structure. The details of molecular hyperfine structure depend on the coupling case, but as the rotational structure and hyperfine structure are of similar orders of magnitude, a simple coupling case may not apply. A full molecular coupled channel calculation may then be required, in which Schrödinger's equation is solved explicitly with all the relevant couplings taken into account. Such calculations have been completed for Li_2 and are underway for Na_2 [63]. Caesium poses an even greater problem due to the the large spin ($\frac{7}{2}$) of the nucleus; even in $^{23}Na_2$ and $^{7}Li_2$, where the nuclear spin is $\frac{3}{2}$, there are 96 ways the electronic orbital, spin, nuclear and rotational angular momenta can couple to give a state of good total angular momentum and parity [63]. A similar calculation for caesium would be a major undertaking, and is beyond the scope of this work; such a calculation may well prove necessary, however, for a fuller understanding of the caesium dimer.

Chapter 6

Conclusions and suggestions for future work

6.1 Scattering theory

6.1.1 Summary

We have discussed methods for calculating potential curves from spectroscopic data, and developed computer techniques for calculating cross sections from interatomic potentials. We have investigated the accuracy of different approximations to the low temperature cross section. We demonstrated that when there is a bound state very close to the dissociation limit (as would seem to be the case for caesium [12]), and the scattering length becomes very large, the scattering length approximation is no longer a good one. A better approximation is the effective range expansion, which is a good model over a wider range of energies.

6.1.2 Future work

Theoretical investigations of Bose-Einstein condensates to date have generally modelled the interactions between atoms purely in terms of the scattering length. Given that the interactions between caesium atoms are probably better modelled using the effective range approximation, a better understanding of condensates may be possible if this improved expression for interactions is used.

6.2 The singlet $B^1\Pi_u \leftarrow X^1\Sigma_g^+$ bands

6.2.1 Summary

We have obtained spectra for the bandhead region of 22 vibrational bands in the singlet B-X system of Cs_2. We found the approximate frequencies of the bandheads, which agreed well with the bandhead positions deduced from the Dunham coefficients of Diemer et al. [29] and Weickenmeier et al. [25]. The $v' = 3 \leftarrow v'' = 0$ band was studied in detail, and rotationally resolved spectra of 35GHz of this band were obtained. We have developed a theoretical model of the rotational structure of this singlet band. This required detailed analysis of the relative transition probabilities to take into account optical pumping and the small solid angle subtended by the detector.

By fitting the theoretical model to the experimental spectrum, we extracted rotational constants for the $v' = 3$ $B^1\Pi_u$ state and the $v'' = 0$ $X^1\Sigma_g^+$ state. We found a fairly good agreement between the B_v values found in this work and those calculated from the previous work of [25] and [29], but noted that the fit was not very sensitive to these constants. We found better agreement when we compared the line positions deduced in this work to those of the previous work, with a maximum discrepancy of 55MHz between corresponding line positions.

We conclude that our singlet results are in good agreement with the previous work, and so further detailed study is not required. However, this study of the singlet spectra enabled us to establish the best experimental procedure and to check the accuracy of our calibration techniques.

6.3 The triplet $(2)^3\Pi_g \leftarrow x^3\Sigma_u^+$ bands

6.3.1 Summary

We have obtained spectra of 10 vibrational bands of the triplet system of Cs_2. We found the frequencies of the peaks of the bands and the peaks of the Q branches to an accuracy of $0.03cm^{-1}$. We found that our band positions agreed with those found by Kim and Yoshihara [26], but did not agree with the band positions of Diemer et al. [28]; hence we have been able to resolve the discrepancy between the two experiments. There were discrepancies of around $0.3cm^{-1}$ between the peak positions

found in this work and those of Kim and Yoshihara [26]; these could be explained as due to different experimental conditions in the two cases leading to different rotational temperatures, and hence the greatest intensity occurring in different parts of the band.

We were able to observe reproducible structure within the band, which we believe is rotational in origin. We were not able to resolve rotational lines, as they are spaced by $\sim$ 100MHz [28], and the linewidth achieved in our experiments was 350MHz.

We found that the theoretical model developed to fit the singlet bands was not adequate to fit the triplet bands. It is likely that this is due to additional structure in the triplet bands due to the hyperfine interaction. The fit was sufficient to demonstrate that the broad rotational contour of the $\Omega = 2, v' = 0, v'' = 0$ band is roughly consistent with the theoretical rotational constants of Spiess [27] and Foucrault et al. [23].

6.3.2 Suggestions for future work

Our attempts to determine rotational constants from our experimental data have been limited by the inadequacies of the theoretical model. The next step in this analysis would be to add in hyperfine structure in an attempt to model the additional peaks in the spectra which are not reproduced by the current model.

It would also be desirable to obtain better resolution of the spectra. The Doppler width could be reduced by narrowing the slit and/or by raising the nozzle. However, both of these alterations will also decrease the level of signal. In order to increase the signal level, we could redesign the oven to withstand higher temperatures (by using different heater wires and solder). If this were done, then it would also be helpful to increase the quantity of caesium loaded into the oven each time, to maintain the duration of each run.

Although we have only studied the lowest two vibrational states of the ground state triplet potential, this data provides important additional constraints on the potential. We have been able to resolve the discrepancy between the two previous sets of data, and we have found that the separation of the first two vibrational states is 11.04cm^{-1}. Although a detailed analysis of the rotational structure has not been possible, we have shown that the ground state rotational constant is of the order 6×10^{3}cm^{-1}. In order to continue towards a determination of the scattering length, information about the interatomic potential up to the dissociation limit is required. One way to proceed would be to use this experimental data to constrain theoretical

potentials. The molecular constants derived from the potential of Fourault et al. [23] are in reasonable agreement with the experimental data; using this potential with the long range coefficients of Marinescu and Dalgarno [44], Pillet et al. [21] derived a scattering length of -250a_0. The agreement between our experimental data and the potential used in their calculation suggest that this value for the scattering length is reasonable. It may be possible to modify this theoretical potential slightly to reproduce the experimental vibrational levels (using, for example, an inverse perturbation approach [64]), and then to use the modified potential to derive the scattering length in the same way.

Alternatively, we could look to experimental techniques to study the higher lying levels of the potential. However, even with the above modifications to the experiment, we would only expect to observe at most two or three more vibrational levels of the ground state. This would still leave a gap in our knowledge of the potential between these low lying states and the region where long range parameters are applicable. We need to investigate alternative techniques for studying the higher vibrational levels. One such technique is *photoassociation spectroscopy.*

6.3.3 Photoassociation spectroscopy

The method of photoassociation spectroscopy was first proposed in 1987 by Thorsein, Weiner and Julienne [14]. Alkali atoms are confined in a magneto-optical trap or far-off-resonance optical dipole force trap (FORT). A pair of colliding ultracold atoms in the trap can resonantly absorb a laser photon to produce a bound, excited molecule. Photons are provided either by an additional laser, or by the FORT laser itself. As the laser is tuned, absorption peaks occur when the frequency corresponds to a transition between the dissociation limit of the ground state and a bound vibrational level of the excited state (see figure 6.1). The excited state molecules formed may then decay either to a bound ground-state molecule, or to an unbound atom pair [65]. Either the fluorescence from the transition itself can be monitored, which will increase on resonance, or the number of atoms in the trap can be monitored, which will decrease on resonance, as the molecules which drop back to the ground state are lost from the trap. Normally we would expect to see only broad diffuse bands arising from free-bound transitions; but in the case of ultracold laser cooled atoms, the energy spread of the initial colliding atoms is very small (21MHz at T=1mK). Hence the linewidth of these free-bound transitions will be comparable to that of bound-bound transitions;

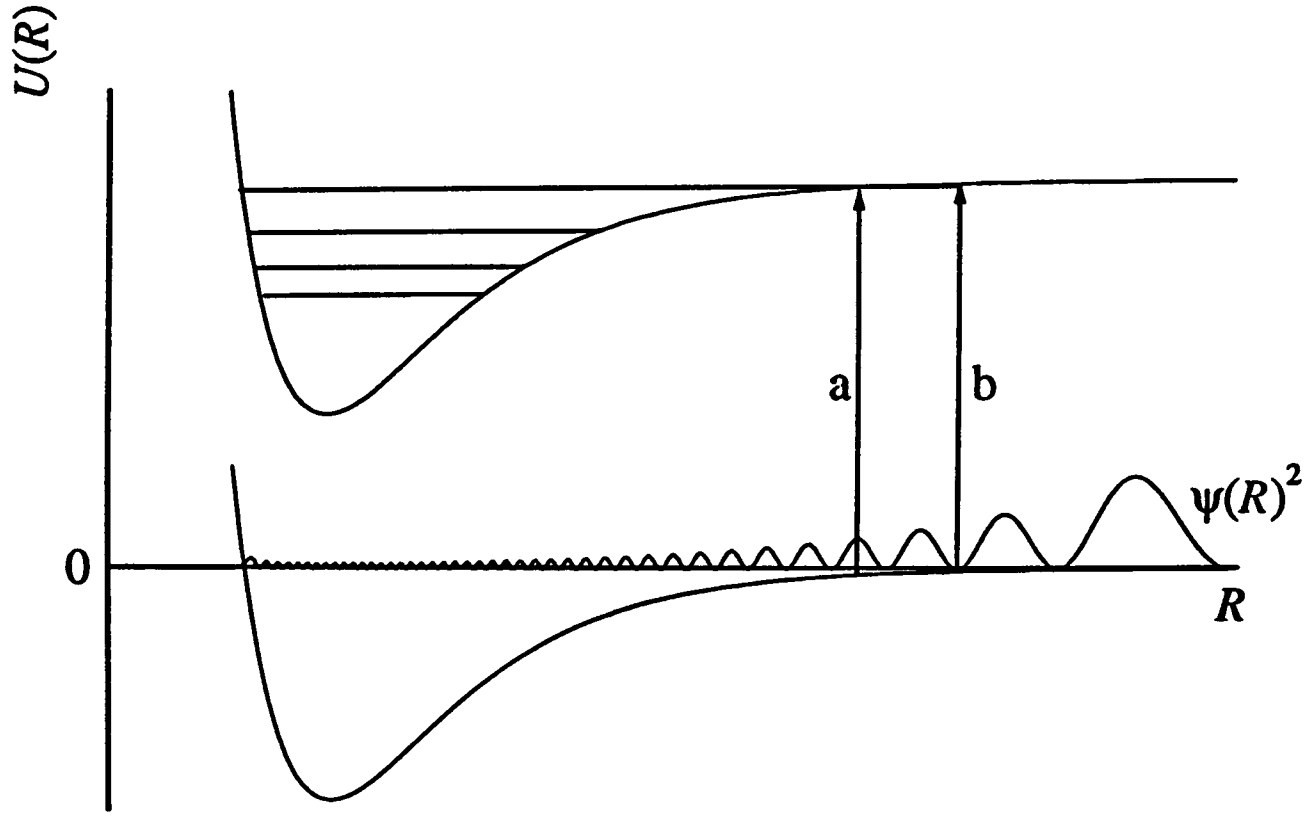

Figure 6.1: Transitions occurring in photoassociation spectroscopy

the technique is analogous to the laser induced fluorescence (LIF) technique used in our experiments. The resulting spectrum gives the energy levels of the excited state.

In addition, information on the ground state potential and scattering wavefunction can be obtained from line shapes and intensity patterns[66], by considering the Franck-Condon factors for the free-bound transitions. Franck-Condon factors for bound-bound transitions were discussed in section 2.5.3. For the bound excited state, the square of the wavefunction, and hence probability, is greatest at the classical turning points. Figure 6.1 shows the square of the wavefunction for the initial state. If there is an antinode of the lower wavefunction vertically below the outer turning point of the excited vibrational state (transition a) then the Franck-Condon factor and hence intensity of the line will be large. If there is a node below the outer turning point (transition b), then the Franck-Condon factor will be small, and the line weak. By measuring the intensities of the transitions, information about the ground state dissociation limit wavefunction can be found, which could lead to a determination of the scattering length.

The technique can be extended to give information about the vibrational levels of the ground state potential, not only the dissociation limit [6]. The photoassociation laser frequency ω_l is fixed on a resonance, increasing the loss from the trap, and so decreasing the trap fluorescence. A second laser of frequency ω_{bb} is then used to tune over transitions between the excited state, and bound states of the ground-state

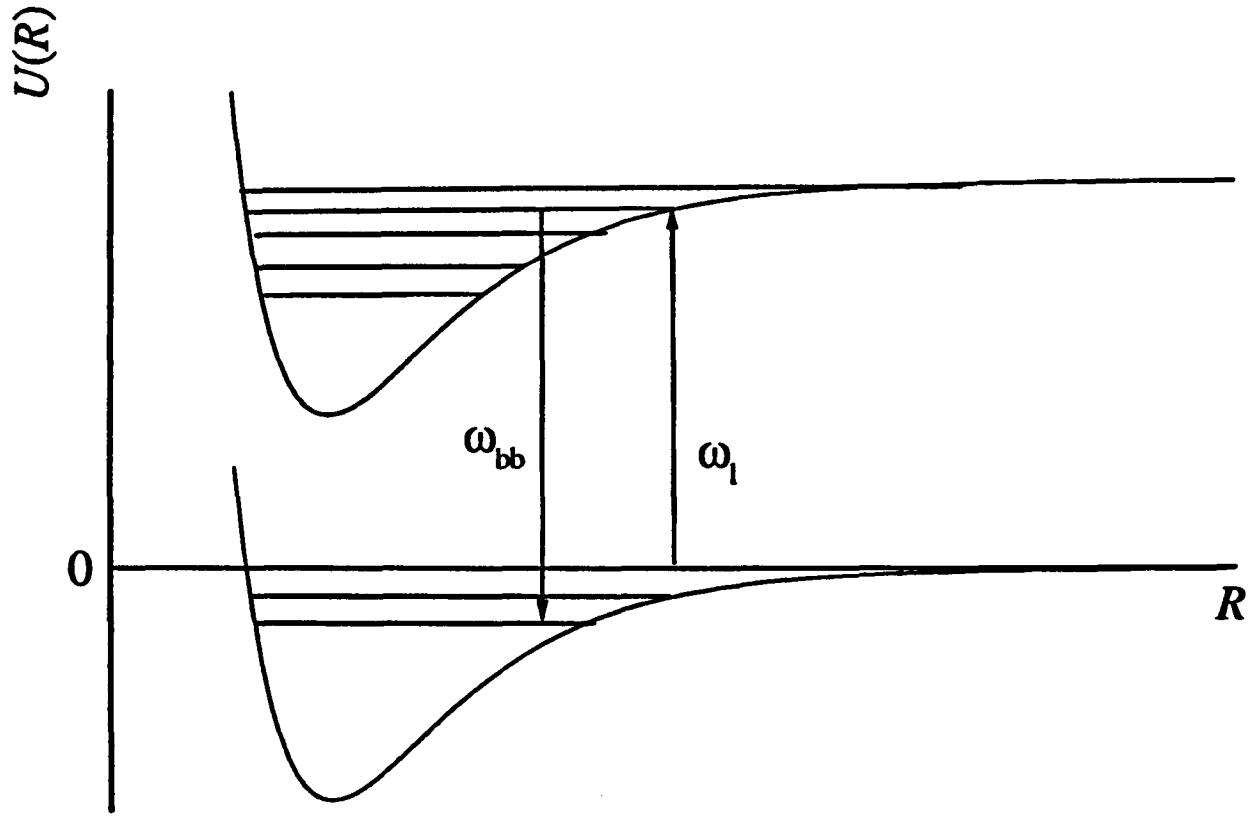

Figure 6.2: Transitions involved in two photon photoassociation spectroscopy.

potential. When this second laser is tuned to a resonance, the rate of loss from the trap is reduced, and the trap fluorescence increases (see figure 6.2).

Photoassociation spectroscopy has two major advantages over the LIF technique used in this work. Firstly, as the initial state is formed in a collision, both singlet and triplet states can be studied. Secondly, due to the Franck-Condon factors it is the higher lying states which are excited; it is the higher lying states which we need to study to calculate scattering lengths, and which cannot be studied easily using LIF.

However, photoassociation spectroscopy is difficult. Although it has been used successfully to study Li_2, Na_2 and Rb_2 and K_2, an attempt to observe photoassociation in caesium at NIST was unsuccessful; in Paris, Pillet has now made preliminary observations. Caesium presents a particular problem as the photoassociation rate is predicted to decrease with increasing atomic mass from Li to Cs; observations of photoassociation in caesium by studying trap loss in a MOT are also made more difficult because the rate of trap loss due to photoassociation also decreases with increasing mass [21].

Appendix A

Numerov method of calculating wavefunctions

We have found it necessary to calculate numerically wavefunctions for interatomic potentials, both to find the bound states, and to find the wavefunctions and hence phase shifts for states above the dissociation limit. We will outline here the techniques used, based on the Numerov method.

A.1 Bound states

The original program we worked from used the Numerov algorithm to perform numerical integration of the radial Schrödinger equation. The general procedure is as follows. The program reads in the potential curve and parameters from file. An estimate of the first eigenvalue is either input by the user, or estimated by the program assuming a harmonic potential. The classical turning points of the potential at this energy are then found.

Starting just outside the outer turning point, the outermost point of the wavefunction is chosen to be a positive value (the value chosen is not important, as it only determines the normalisation of the wavefunction). The next point in is estimated by [67]

$$\psi_n = \psi_{n+1} \exp\left(r^{n+1}\sqrt{2m/\hbar^2(V_{n+1}-E)} - r^n\sqrt{2m/\hbar^2(V_n-E)}\right) \qquad \text{(A.1)}$$

Further values of the wavefunction for smaller radii are then found using the

Numerov algorithm:

$$\psi_n = \frac{2\psi_{n+1} + 10C\psi_{n+1}V_{n+1} + C\psi_{n+2}V_{n+2} - \psi_{n+2}}{1 - CV_N} \tag{A.2}$$

where V_n is shorthand for $V_n - E$. For SI units

$$C = \frac{H^2\mu}{6\hbar^2} \tag{A.3}$$

where H is the spacing between points and μ is the reduced mass.

The wavefunction is integrated inwards in this way until the point halfway between the turning points is reached, or the outermost antinode of the wavefunction is passed.

Using starting values of 0 and a constant, the same procedure is then used to find the wavefunction from the inner turning point (replacing n+1 with n-1 and n+2 with n-2 in the Numerov formula) until there is an overlap of 5 points between the two parts of the wavefunction. The norm of the two parts N=$\sum_n \psi_n^2$ is calculated. Cooley's eigenvalue predictor is then used to predict the error in E:

$$\Delta E = \frac{(-Y_{-1} + 2Y_0 - Y_1)/H^2 + (V_{mid} - E)}{N^2/H} \tag{A.4}$$

where

$$Y_{-1} = (1 - C(V_{mid-1} - E)) \times \frac{\psi_{mid-1}}{\psi_{mid}} \tag{A.5}$$

$$Y_0 = (1 - C(V_{mid} - E)) \tag{A.6}$$

$$Y_1 = (1 - C(V - mid + 1 - E)) \times \frac{\psi_{mid+1}}{\psi_{mid}} \tag{A.7}$$

and *mid* is the middle value of the overlap region.

If ΔE is sufficiently small, then the two parts of the wavefunction are normalised so that they are on the same scale and join smoothly, else another iteration takes place with the new value of E. The wavefunction and energy value are written to file, and the program moves on to find the next eigenvalue.

In this way, we can find the energies of the vibrational states of an interatomic potential.

A.2 Extension of bound state calculation to find scattering wavefunctions

We wished to adapt the method to find the wavefunctions for unbound states, just above the dissociation limit, so that we could find the phase shift. The first method

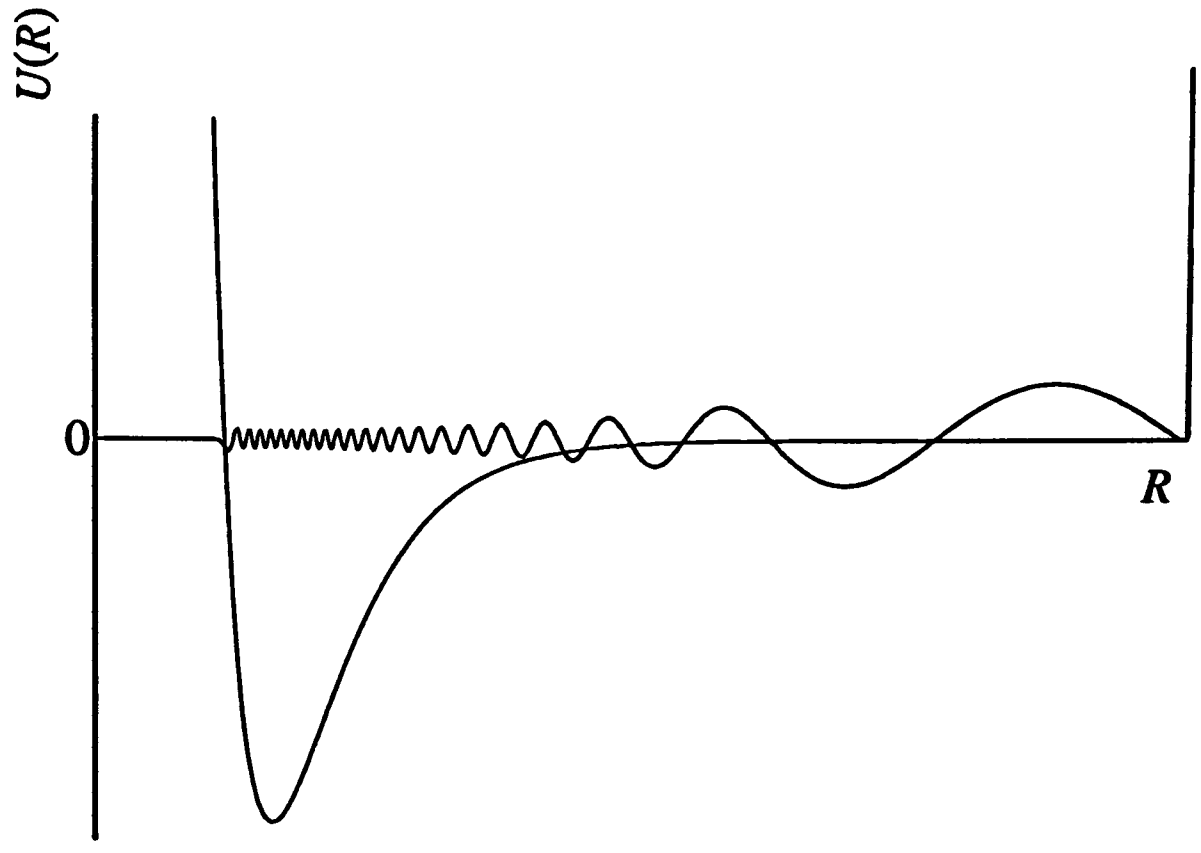

Figure A.1: Scattering wavefunction calculated using a 'wall' in the potential

we used was to use the same program, but to adapt the potentials. By adding a "wall" to the potential at a large radius (figure A.1), we can once again constrain the wavefunction between two turning points, with the wavefunction falling to zero at the outer wall. The energy of the state and the wavevector k are determined by the position of the outer wall. The further out the wall, the smaller the value of k and of the energy above dissociation. However, we found that in order to reach the low energies required to calculate scattering lengths, we needed to use a wall at a very large radius, and so the deep part of the potential well covered only a small fraction of the total range. Since the number of points used to determine the potential is limited to 10000, this meant that very few points were used over the main part of the potential well, while many points were used to describe the potential where it was almost flat, near the dissociation limit, and so the potential was not well represented.

A.3 Revised program to find scattering wavefunctions

We altered the original bound state program to calculate the scattering wavefunctions. We removed the inwards integration step, and replaced it with a sine wave. The wavevector of the sine wave is determined by the user, while the phase is found by the program. The outwards integration is performed in the same way as before, using the fixed value of energy determined by the wavevector, and the outwards wavefunction is joined to the sine wave at a suitably large radius, where the potential is very close to its dissociation limit, and so the wavefunction is close to that of a free particle.

Cooley's method, in which the wavefunction is found by succesive approximations to the energy, is no longer appropriate, as the energy is now a fixed parameter; instead it is now a phase which is to be found. We divided each set of overlap values by the central value (hence putting the two sets of values on the same scale), found differences between corresponding values from the two sets, and found the sum of the squared differences. We found the phase which gave the minimum value of this sum by bisection [68].

We also adapted the program to generate Morse potentials without reading from file. In this way we could quickly find the effect of varying a parameter in the potential. Alternatively, we could vary the energy, while keeping the potential the same.

Bibliography

[1] M.H. Anderson, J.R. Ensher, M.R. Matthews, C.E. Wieman, E.A. Cornell, Science **269**, 198 (1995)

[2] C.C. Bradley, C.A. Sackett, J.J. Tollett, G.G. Hulet, Phys. Rev. Lett. **75**, 1687 (1995)

[3] K. B. Davis, M.-O Mewes, M. R. Andrews, N. J. van Druten, D. S. Durfee, D. M. Kurn, W. Ketterle, Phys. Rev. Lett **75**, 3969 (1995)

[4] C. S. Adams, E. Riis, Prog. Quant. Electr. **21**, 1 (1997)

[5] K. Huang, *Statistical Mechanics* (Wiley, New York, 1963)

[6] E. R. I. Abraham, W. I. McAlexander, C. A. Sackett, R. G. Hulet, Phys. Rev. Lett. **78**, 1315 (1995)

[7] C.C. Bradley, C. A. Sackett, R. G. Hulet, Phys. Rev. Lett **78**, 985 (1997)

[8] W. Ketterle, N. J. Van Druten, Advances in atomic, molecular and optical physics **37**, 181 (1996)

[9] P. O. Fedichev, M. W. Reynolds, G. V. Shlyapnikov, Phys. Rev. Lett **77**, 2921 (1996)

[10] K. Gibble, S. Chu, Phys. Rev. Lett **70**, 1771 (1993)

[11] E. Audouard, P. Duplàa, J. Vigué, Europhys. Lett. **32**, 397 (1995)

[12] M. Arndt, M. Ben Dahan, D. Guéry-Odelin, M. W. Reynolds, J. Dalibard, Phys. Rev. Lett **79**, 625 (1997)

[13] B. Verhaar, K. Gibble, S. Chu, Phys. Rev. A **48**, R3429 (1993)

[14] H. R. Thorsheim, J. Weiner, P. S. Julienne, Phys. Rev. Lett, **58**, 2420 (1987)

[15] E. Tiesinga, A.J. Moerdijk, B.V. Verhaar, H.T.C. Stoof, Phys. Rev. A **46**, R1167 (1992)

[16] P. O. Fedichev, Y. Kagan, G. V. Shlyapnikov, J. T. M. Walraven, Phys Rev Lett. **77**, 2913 (1996)

[17] E. R. I. Abraham, W. I. McAlexander, J. M. Gerton, R. G. Hulet, R. Côté, A. Dalgarno, Phys. Rev. A **55**, R3299 (1997)

[18] R. Côté, A. Dalgarno, Phys. Rev. A. **50**, 4827 (1994)

[19] H. M. J. M. Boesten, C. C. Tsai, J. R. Gardner, D. J. Heinzen, B. J. Verhaar, Phys. Rev. A. **55**, 636 (1997)

[20] J. R. Gardner, R. A. Cline, J. D. Miller, D. J. Heinzen, H. M. J. M. Boesten, B. J. Verhaar. Phys. Rev. Lett. **74**, 3764 (1995)

[21] P. Pillet, A. Crubellier, A. Bleton, O. Dulieu, P. Nosbaum, I. Mourachko, F. Masnou-Seeuws, J. Phys. B **30** 2801 (1997)

[22] M. Krauss, W. J. Stevens, J. Chem. Phys **93**, 4236 (1990)

[23] M. Foucrault, Ph. Millie, J. P. Daudey, J. Chem. Phys. **96**, 1257 (1992)

[24] M. Marinescu, H. R. Sadeghpour, A. Dalgarno, Phys. Rev. A. **49**, 982 (1994)

[25] W. Weickenmeier, U. Diemer, M.Wahl, M. Raab, W. Demtröder, J. Chem. Phys. **82**, 5354 (1985)

[26] B.Kim, K.Yoshihara, Chem. Phys. Lett. **204**, 407 (1993)

[27] N. Spiess, Ph.D Thesis, Fachbereich Chemie, Universität Kaiserslautern (1989)

[28] U. Diemer, J. Gress, W. Demtröder, Chem. Phys. Lett. **178**, 30 (1991)

[29] U. Diemer, R. Duchowicz, M. Ertel, E. Mehdizadeh, W. Demtröder, Chem. Phys. Lett. **164**, 419 (1989)

[30] C. Amiot, W. Demtröder, C. R. Vidal, J. Chem. Phys **88**, 5265 (1988)

[31] M. Raab, G. Höning, W. Demtröder, C. R. Vidal, J. Chem. Phys **76**, 4370 (1982)

[32] C. Amiot, J. Verges, Chem. Phys. Lett **116**, 273 (1985)

[33] J. C. McLennan, D. S. Ainslie, Roy. Soc. Proc. A, **103** 304 (1923)

[34] F. W. Loomis, P. Kusch, Phys. Rev. **46**, 292 (1934)

[35] P. Kusch, M. M. Hessel, J. Mol. Spec. **32**, 181 (1969)

[36] J. M. Walter, S. Barratt, Roy. Soc. Proc. A, **119** 257 (1928)

[37] B. H. Bransden, C. J. Joachain, *Physics of atoms and molecules,* (Longman 1983)

[38] G. Herzberg, *Spectra of diatomic molecules*, (Van Nostrand 1950)

[39] A.I.M. Rae *Quantum Mechanics* (IOP 1992)

[40] J. L. Dunham, Phys. Rev. **41**, 721 (1932)

[41] G. Scoles, *Atomic and molecular beam methods*, (OUP 1988)

[42] G. K. Woodgate, *Elementary atomic structure*, (OUP 1980)

[43] G.C. Maitland, M. Rigby, E. B. Smith, W. A. Wakeham *Intermolecular forces* (OUP, 1987)

[44] M. Marinescu, A. Dalgarno, Phys. Rev. A **52**, 311 (1995)

[45] S. J. Lawrence, *D. Phil Thesis*, (Oxford 1995)

[46] K. Burnett, Contemp. Phys., to be published

[47] G. F. Gribakin, V. V. Flambaum, Phys. Rev. A **48**, 546 (1993)

[48] L.D. Landau, E.M. Lifshitz, *Quantum mechanics*(Pergamon 1991)

[49] N. F. Mott, H. S. W. Massey, *The theory of atomic collisions*, (OUP 1965)

[50] S. Gerstenkorn, P. Luc, *Atlas du spectre d'absorption de la molecule d'iode* (Orsay 1978)

[51] Coherent CR699 ring dye laser instruction manual

[52] H. D. Babcock, L. Herzberg, Astrophys. J. **108**, 167 (1948)

[53] D.R. Miller, *Atomic and molecular beam methods*, ed.G. Scoles, (OUP 1988)

[54] C.J.K Quale, *D. Phil Thesis*, (Oxford 1993)

[55] D. Lucas, *First year report* (Oxford 1994)

[56] L.E. Selin, Arkiv för Fysik **21**, 479 (1961)

[57] D. R. T. Appadoo, P. F. Bernath, R. J. Le Roy, Can. J. Phys. **72**, 1265 (1994)

[58] K. C. Smyth, P. K. Schenck, Chem. Phys. Lett. **55**, 466 (1978)

[59] G. Moe, A. C. Tam, W. Happer, Phys. Rev. A **14**, 349 (1976)

[60] A. R. Edmonds, *Angular momentum in quantum mechanics*, (Princeton UP 1957)

[61] A.P. Thorne, *Spectrophysics*, (Chapman and Hall 1988)

[62] H. Weickenmeier, U. Diemer, W. Demtröder, Chem. Phys. Lett, **124**, 470 (1986)

[63] C. J. Williams, E. Tiesinga, P. S. Julienne, Phys. Rev. A **53**, R1939 (1996)

[64] W.M. Kosman, J.Hinze, J. Mol. Spectrosc. **56**, 93 (1975)

[65] E. R. I. Abraham, W. I. McAlexander, J. M. Gerton, R. G. Hulet, R. Côté, A. Dalgarno, Phys. Rev. A **53**, R3713 (1996)

[66] R. Napolitano, J. Weiner, C. J. Williams, P. S. Julienne, Phys. Rev. Lett, **73**, 1352 (1994)

[67] D. R. Hartree, *The calculation of atomic structures* (Chapman and Hall, 1957)

[68] W. H. Press, B. P. Flannery, S. A. Teukolsky, W. T. Vetterling, *Numerical recipies in C*, (CUP, 1988)